

# Doctoral Dissertation

## Top-pair differential cross sections in $pp$ collisions at $\sqrt{s}=13$ TeV with the ATLAS detector

(ATLAS実験 $\sqrt{s}=13$  TeV 陽子衝突におけるトップ  
クォーク対生成の微分断面積)

January 2018

Graduate School of Science

Kobe University

Ye Chen

(陳 叶)



## Abstract

This thesis presents the measurement of the  $t\bar{t}$  differential cross section with the boosted top quarks. The measurement uses proton–proton collisions at a center-of-mass energy of  $\sqrt{s} = 13$  TeV. The data set corresponds to an integrated luminosity of  $36.1 \text{ fb}^{-1}$ , recorded in 2015 and 2016 with the ATLAS detector at the CERN Large Hadron Collider. Events with two large-radius jets in the final state, one with transverse momentum  $p_{\text{T}} > 500$  GeV and a second with  $p_{\text{T}} > 350$  GeV, are used for the measurement. The top quark candidates are separated from the multijet background by data-driven method using jet mass, jet substructure information and association with a  $b$ -tagged jet. The measured spectra are corrected for detector effects to a particle-level fiducial phase space and are compared to several predictions based on perturbative QCD calculation.

As a result, the inclusive cross section for  $t\bar{t}$  production in the fiducial phase-space region is  $292 \pm 7$  (stat.)  $\pm 76$  (syst.) fb, to be compared to the theoretical prediction of  $384 \pm 36$  fb, which is based on next-to-next-leading-order (NNLO) calculation of perturbative QCD. The predictions are generally in agreement with the measured differential cross section as a function of top-quark and  $t\bar{t}$  system kinematic observables.

# Contents

<b>1</b>	<b>Introduction</b>	<b>3</b>
<b>2</b>	<b>The Standard Model and Top quark</b>	<b>5</b>
2.1	Standard Model (SM)	5
2.2	Top quark	6
2.3	Top-Pair Production in $pp$ collisions	7
2.3.1	Top decays	11
2.4	Cross Section Measurement	13
<b>3</b>	<b>The ATLAS experiment</b>	<b>15</b>
3.1	The Large Hadron Collider	15
3.2	The ATLAS detector	16
3.2.1	The coordinate system	18
3.2.2	Inner Detector	18
3.2.3	Calorimeters	21
3.2.4	Muon Spectrometer	22
3.2.5	Magnet System	26
3.3	ATLAS Trigger and Data Acquisition System	28
3.4	Luminosity measurement	30
<b>4</b>	<b>Datasets and Simulated Samples</b>	<b>33</b>
4.1	Data sample	33
4.2	Simulated samples	33
4.2.1	Matrix Element calculation	35
4.2.2	Parton shower and hadronization models	35
4.2.3	Signal and background samples	36
<b>5</b>	<b>The reconstruction of physics objects in ATLAS</b>	<b>38</b>
5.1	Jet reconstruction	38
5.1.1	$b$ -tagging	39
5.1.2	Top tagging	40
5.2	Lepton reconstruction	46

<b>6</b>	<b>Event selection and Background estimation</b>	<b>47</b>
6.1	Event selection . . . . .	47
6.2	Background sources . . . . .	50
6.2.1	Data-driven QCD background estimation . . . . .	51
<b>7</b>	<b>Particle level fiducial phase-space cross sections</b>	<b>58</b>
7.1	Fiducial phase space . . . . .	58
7.2	Unfolding procedure . . . . .	60
<b>8</b>	<b>Systematic uncertainties</b>	<b>69</b>
8.1	Propagation of systematic uncertainties and treatment of correlations	69
8.1.1	Pseudo-experiment . . . . .	69
8.1.2	Covariance Matrix . . . . .	71
8.2	Dominant systematic uncertainties . . . . .	75
8.3	Detailed study on signal modelling uncertainties . . . . .	79
8.3.1	Comparison of POWHEG+PYTHIA8 with POWHEG+HERWIG7 . . . . .	79
<b>9</b>	<b>Result and discussion</b>	<b>88</b>
9.1	Fiducial phase-space inclusive cross section . . . . .	88
9.2	Fiducial phase-space differential cross sections . . . . .	89
9.3	Quantitative comparisons with SM predictions through $\chi^2$ estimator .	97
<b>10</b>	<b>Conclusion</b>	<b>103</b>
	<b>Bibliography</b>	<b>111</b>
<b>11</b>	<b>Appendix</b>	<b>112</b>
11.1	Tables of systematic uncertainties in detail for $t\bar{t}$ fiducial inclusive cross section . . . . .	112
11.2	Particle level covariances and correlations . . . . .	116
11.2.1	Covariance and correlations for absolute differential cross section	116
11.2.2	Covariance and correlations for normalized differential cross section . . . . .	121
11.3	POWHEG+HERWIG7 vs POWHEG+PYTHIA8 @ detector level distribution . . . . .	126
11.3.1	POWHEG+HERWIG7 distribution . . . . .	126
11.3.2	POWHEG+PYTHIA8 distribution . . . . .	130

# Chapter 1

## Introduction

Matter was thought to be made of many kinds of chemical elements long time ago. The periodic table has shown over 100 chemical elements so far. For instance, water ( $\text{H}_2\text{O}$ ) is a compound of the elements hydrogen and oxygen. A hydrogen atom ( $\sim 10^{-10}$  m) contains a proton ( $\sim 10^{-15}$  m) and an electron. Looking into inside further, a proton consists of three quarks ( $< 10^{-18}$  m). Through a series of experiments in fields of cosmic ray and high energy physics, it is currently believed that the matter is made of quarks and leptons. The particle physics is to describe the fundamental building blocks, the *elementary particles*, of the matter and their interactions. At present, the SM (Standard Model) has been enormously successful in describing a wide variety of phenomenons in the particle physics. The most recent and notable example is the discovery of the Higgs boson reported in July 2012. It is used to explain where the mass of an elementary particle comes from.

SM consists of six quarks, six leptons, four kinds of gauge bosons and a Higgs boson. Gauge bosons mediate the interaction between the elementary particles. Top quark as one of quarks was discovered by the CDF and DØ experiments at the Tevatron proton-antiproton ( $p\bar{p}$ ) collider in 1995. Since its discovery, the study of the top quark represented one of the most interesting fields in particle physics. For instance, the top quark has short lifetime so that it can not form a hadron before it decays to a lighter quark. This implies the unique possibility to observe the properties of a “bare” quark.

In order to obtain top quarks to study their properties, the colliders, like the Tevatron, are used to produce the elementary particles. Now the LHC (Large Hadron Collider) is the most powerful accelerator in the world. It is located at CERN (the European Organization for Nuclear Research) and currently collides proton-proton pairs ( $pp$ ) at a center-of-mass energy  $\sqrt{s} = 13$  TeV, the highest collision energy in the world. It can produce as many as 10 top pairs per second and act as a top factory. These many top quarks may show some hint to answer some open questions of SM and provide evidence to support new physics theories.

The topic of this dissertation is to measure the top quark pair ( $t\bar{t}$ ) differential cross sections in  $pp$  collisions at  $\sqrt{s} = 13$  TeV. The top quark decays almost 100% into a  $W$  boson and a  $b$ -quark. With the increase of top quark transverse momentum,

the decay products from top quark are generated within a narrow angular area. Such a top quark is called “boost top quark”. This measurement utilizes the boosted top quarks using a full dataset of the 13 TeV collisions taken during 2015 and 2016. The large amount of produced top quark pairs ( $t\bar{t}$ ) allows measurements of differential cross sections as a function of various kinematic variables, such as the momentum of the top quark and the invariant mass of top quark pairs. This verifies the SM predictions and is sensitive to new physics.

The structure of this thesis is the following. In Chapter 2, theoretical aspects of SM and top quark physics are described together with top quark pair production mechanism. The ATLAS experiment is one of the LHC projects. The description on the ATLAS detector is given in Chapter 3. A detailed description of the collected data sample and simulation samples are in Chapter 4. The simulation samples are generated using event generator models for the production of  $t\bar{t}$  events and background estimation. In Chapter 5 the reconstruction of physics objects used in this analysis is described. The event selection and background estimation are shown in Chapter 6. Chapter 7 describes the procedure to calculate the  $t\bar{t}$  differential cross sections. Systematic uncertainties are described in Chapter 8. The results of top pair cross sections and comparisons with different  $t\bar{t}$  predictions are presented in Chapter 9. The conclusion of this measurement is given in the last Chapter.

# Chapter 2

## The Standard Model and Top quark

In this chapter, the SM and physics related to the top quark are described in section 2.1 and 2.2. Then the top pair production mechanism and top decay channels are introduced in section 2.3. Section 2.4 presents general concept of cross section and physics motivation of measuring differential cross section of  $t\bar{t}$  production.

### 2.1 Standard Model (SM)

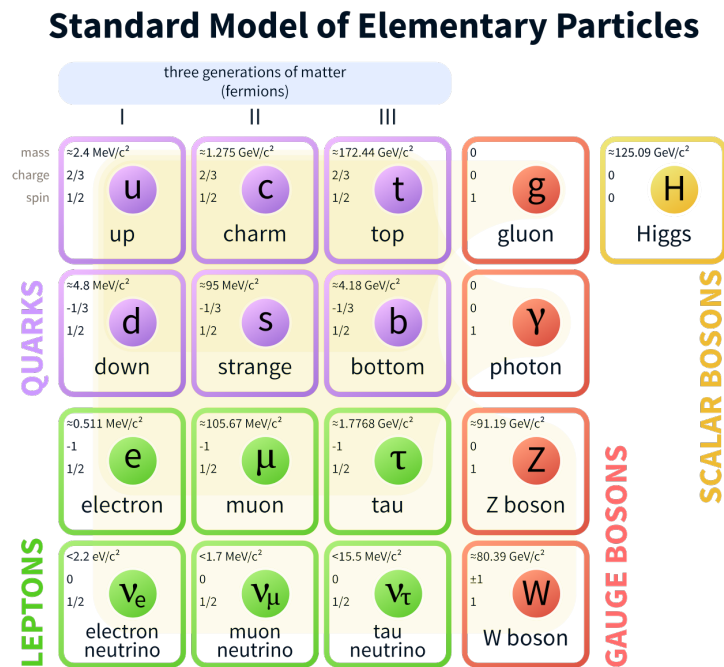


Figure 2.1: Standard Model: Magenta indicates quarks; Green indicates leptons; Red indicates gauge bosons; Yellow indicates Higgs. [1]

The Standard Model of particle physics is the theory describing the interactions mediated by gauge bosons between elementary particles (fermions). The strong interaction, whose typical range is  $10^{-15}$  m, is carried by a particle called the gluon, and is responsible for the binding of quarks together to form hadrons, such as protons. The weak interaction, whose typical range is  $10^{-18}$  m, is carried by particles called  $W^\pm$  and  $Z$  bosons. The force is, for example, responsible for the radioactive  $\beta$ -decay, such as  $n \rightarrow p + e^- + \bar{\nu}$ . The electromagnetic force carried by the photon creates electric and magnetic fields, which are responsible for electromagnetic waves such as light, and thus propagates over an infinite distance.

Within the Standard Model, the elementary particles consist of 12 flavours of fermions (spin  $\frac{1}{2}$ ), six flavours of quarks and six flavours of leptons, four gauge bosons (spin 1), which mediate forces between fermions, and one scalar particle (Higgs boson) being responsible for giving mass to these particles. The Higgs boson was discovered by the two experiments (ATLAS and CMS) of the LHC in summer 2012 [2]. The six leptons consist of neutrinos and charged leptons. Neutrinos interact with other fermions only through the weak interaction via exchange of massive gauge bosons ( $Z$  and  $W^\pm$ ). Charged leptons take part both in weak and electromagnetic interactions. The six flavours of quarks are classified into doublets for each generation, *up*-type and *down*-type. Quarks interact with other quarks via strong interaction mediated by gluons as well as weak and electromagnetic interactions. The top quark is the third generation *up*-type quark. The details about the properties of these particles are pictorially shown in the Fig. 2.1.

## 2.2 Top quark

The top quark was discovered by the CDF and DØ experiments in 1995 [3][4] at the Tevatron, which is a proton-antiproton collider, with a center-of-mass energy  $\sqrt{s} = 1.8$  TeV at Fermilab. Its discovery completes the three generation structure of quarks in the Standard Model. The properties of the top quark are later studied by experiments of the LHC in detail. The result of top quark mass combining Tevatron and LHC experiments is  $m_{top} = 173.34 \pm 0.27$  (stat.)  $\pm 0.71$  (syst.) GeV [5]. Currently in the LHC, the most precise individual measurement of  $m_{top}$  is performed by two collaborations respectively, the value from CMS Collaboration is  $m_{top} = 172.99 \pm 0.13$  (stat.)  $\pm 0.47$  (syst.) GeV [6], and from ATLAS Collaboration, the value is  $m_{top} = 173.35 \pm 0.27$  (stat.)  $\pm 0.42$  (syst.) GeV [7].

There are several reasons why top quark physics is important. Firstly, the top quark has a mass of around 173 GeV, which is the heaviest elementary particle observed so far and approximately at the electroweak symmetry breaking (EWSB) scale. Secondly, the top quark couples strongly with the Higgs sector because of its large mass. This indicates that all new physics in connection with the EWSB should preferentially couple to the top quark. In addition, the top quark has unique short lifetime,  $\tau_{top} = \frac{1}{\Gamma_{top}} \approx 5 \times 10^{-25}$  s, which is almost an order of magnitude smaller than the characteristic time of QCD hadronization ( $O(10^{-24}$  s)), which is described

briefly in Section 2.3.1. This means the top quark decays before it couples to other quarks to form hadrons and corresponds physicists an opportunity to study a bare quark.

## 2.3 Top-Pair Production in $pp$ collisions

The  $t\bar{t}$  production in  $pp$  collisions at the LHC is described as the interaction between gluons and quarks. Top quarks are produced through two kinds of processes. Top quark pairs ( $t\bar{t}$ ) are produced through the strong interaction, while single top quark production occurs via the electroweak interaction. Figure 2.2 shows the schematic QCD description of  $t\bar{t}$  production via strong production and top quark decays. This gives the cross section of  $t\bar{t}$  production:

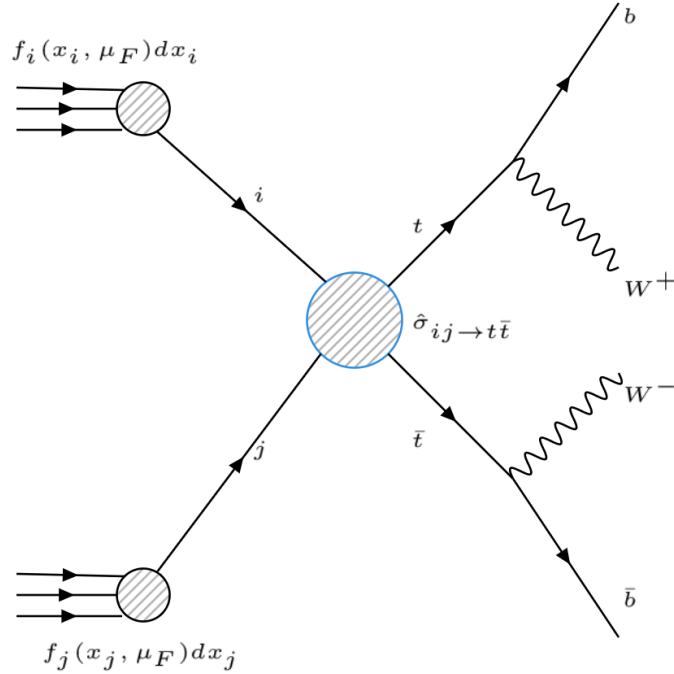


Figure 2.2: Diagram of the  $t\bar{t}$  production and decay at the  $pp$  collisions

$$\sigma_{t\bar{t}}(\sqrt{s}) = \int_0^1 dx_i \int_0^1 dx_j \underbrace{\sum_{i,j} f_i(x_i, \mu_F^2) f_j(x_j, \mu_F^2)}_{\text{long distance}} \times \underbrace{\hat{\sigma}_{ij \rightarrow t\bar{t}}(\hat{s}, m_t, \mu_R, \alpha_S)}_{\text{short distance}}, \quad (2.1)$$

where  $x_i$  and  $x_j$  are their parton momentum fraction in the proton, the indices  $i, j$  sum over the incoming gluons and  $q\bar{q}$  pairs governed by PDFs  $f(x, \mu_f^2)$ ,  $\sqrt{s}$  is the collision energy,  $m_t$  is the top mass and  $\alpha_S$  is the strong coupling constant. The functions  $f_i$  and  $f_j$  are PDFs (Parton Distribution Functions), which describes the probability to find a parton of a given type with a given momentum fraction  $x_i$

when the interaction is assumed at a momentum transfer of  $\mu_F$ , the factorization scale, at which the PDFs  $f_i$  and  $f_j$  are evaluated. The strong coupling constant  $\alpha_S$  is evaluated at  $\mu_R$ , which is the renormalization scale. An example of PDF parametrization is shown in Fig. 2.3. The contribution of gluon collisions to the total cross section becomes large due to the large PDF value with  $x \simeq 2m_t/\sqrt{s} = 0.03$  at the LHC 13TeV energy. The short distance part  $\hat{\sigma}_{ij \rightarrow t\bar{t}}(\hat{s})$  is calculable by using the perturbative QCD (pQCD) theory and can be expanded as

$$\hat{\sigma}_{ij \rightarrow t\bar{t}}(\hat{s}) = a_1(\hat{s})\alpha_S + a_2(\hat{s})\alpha_S^2 + a_3(\hat{s})\alpha_S^3 + \dots, \quad (2.2)$$

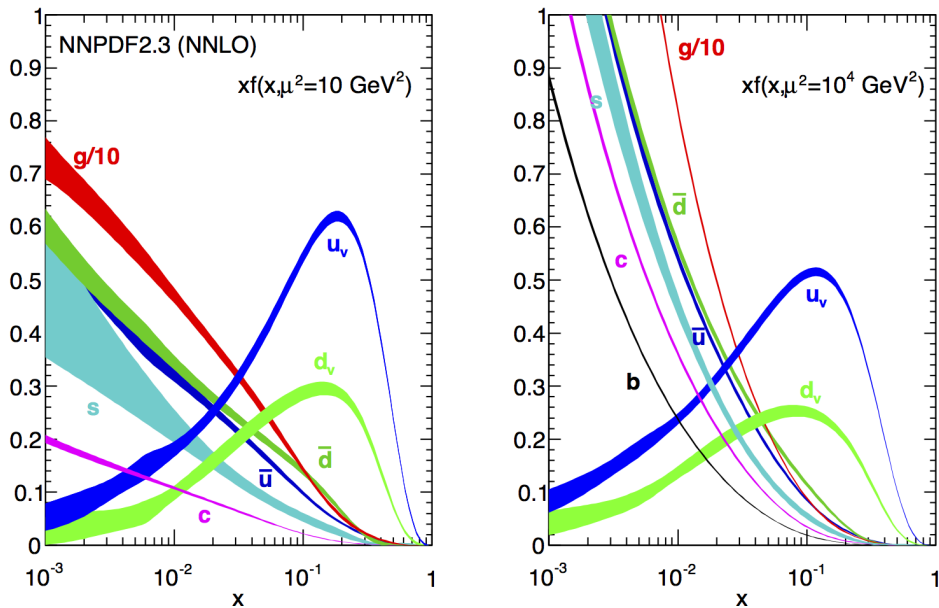


Figure 2.3: NNPDF(NNLO) PDF set [8]. Parton distribution function  $f(x, \mu_F^2)$  for  $\mu_F^2 = 10 \text{ GeV}^2$  and  $\mu_F^2 = 10^4 \text{ GeV}^2$

Each order of the coefficients in principle can be calculated. Figure 2.4 pictorially shows conception related to the order of  $\alpha_S$  in the diagrams. Leading order (LO) corresponds to  $\alpha_S$ , next-to-leading-order (NLO) corresponds to  $\alpha_S^2$  and next-to-next-leading-order (NNLO) corresponds to  $\alpha_S^3$ .

The  $t\bar{t}$  pairs are produced in the LHC through gluon fusion ( $\sim 85\%$ ) and quark-antiquark annihilation ( $\sim 15\%$ ). Since the LHC is a proton-proton collider, the antiquarks are sea quarks. As a result, gluon fusion is the dominant process in contrast to the Tevatron, which was a proton-antiproton collider. Fig. 2.5 show the diagrams for  $t\bar{t}$  production in the leading order (LO:  $\alpha_S$ ) via  $q\bar{q}$  and gluon fusion. Fig. 2.6 show two examples of the diagrams with radiations, initial state radiation (ISR) and final state radiation (FSR), which corresponds to the next-to-leading order (NLO:  $\alpha_S^2$ ).

The latest result of the total cross section of  $t\bar{t}$  production is shown in Fig. 2.7 as a function of collision energies for hadron collider experiments including CDF, DØ, CMS and ATLAS. The measured cross sections are compared to the theoret-

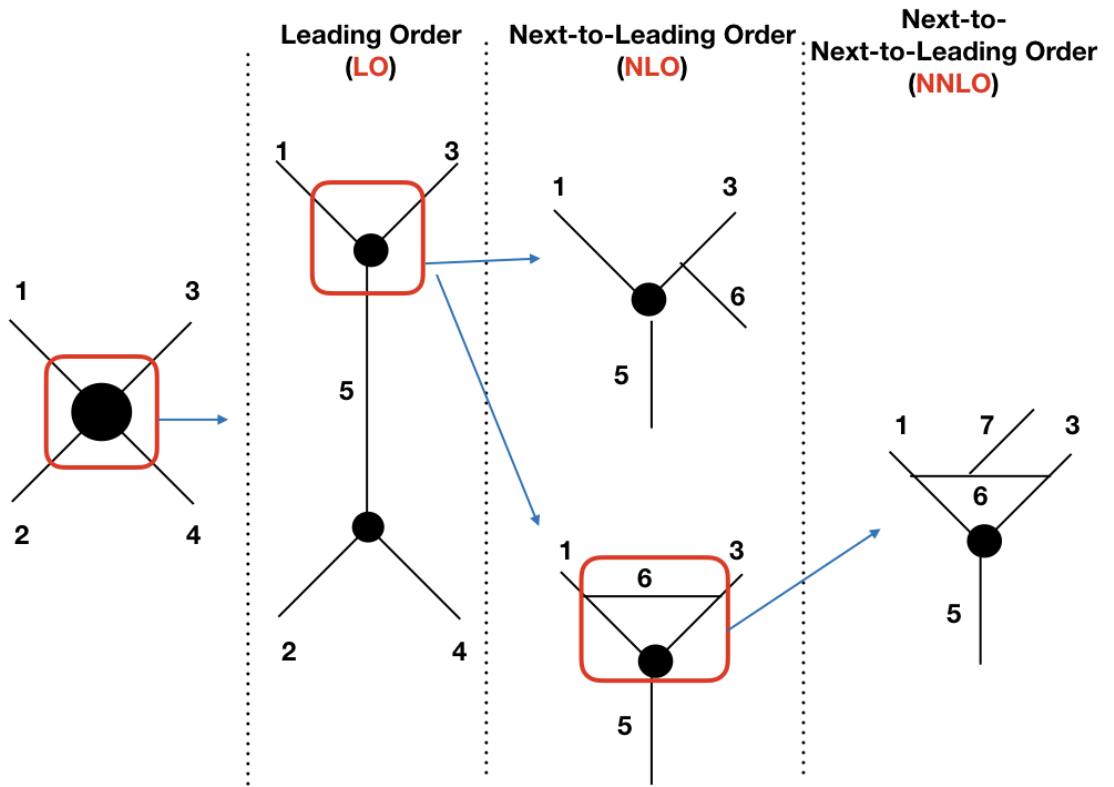


Figure 2.4: A sketch of  $\alpha_S$  order of Feynman diagrams in perturbative theory

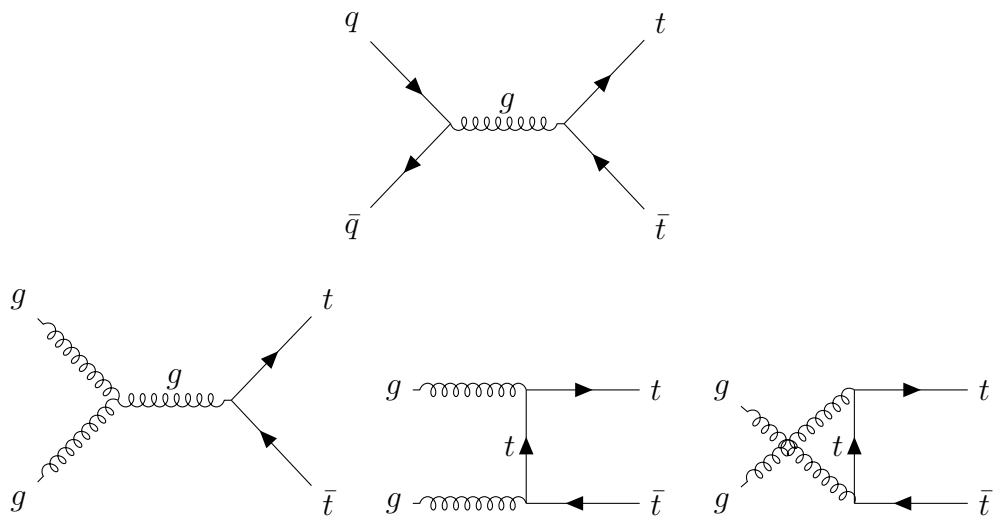


Figure 2.5: The top quark production via  $q\bar{q}$  collision (top diagram), and gluon fusion processes (the bottom three diagrams).

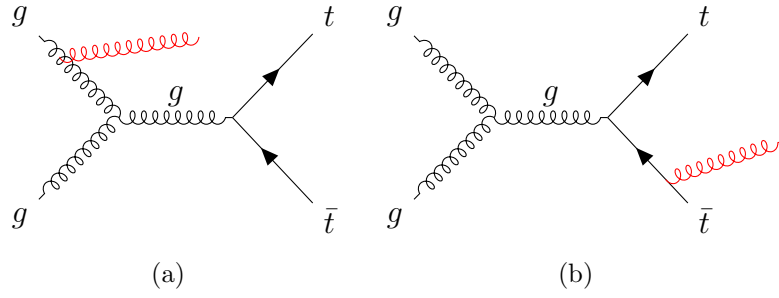


Figure 2.6: (a) initial state radiation (ISR) and (b) final state radiation (FSR) associated with  $t\bar{t}$  production processes.

ical calculations in NNLO (next-to-next-leading-order). At the LHC collision energy of  $\sqrt{s} = 13$  TeV, with the assumption that the top quark mass is 172.5 GeV, the theoretical prediction of  $t\bar{t}$  cross section by the pQCD NNLO calculation is  $\sigma_{t\bar{t}} = 832^{+46}_{-51}$  pb where the uncertainty is mainly from the theoretical uncertainties. These measured total cross sections in the Fig. 2.7, are good in agreement with the prediction.

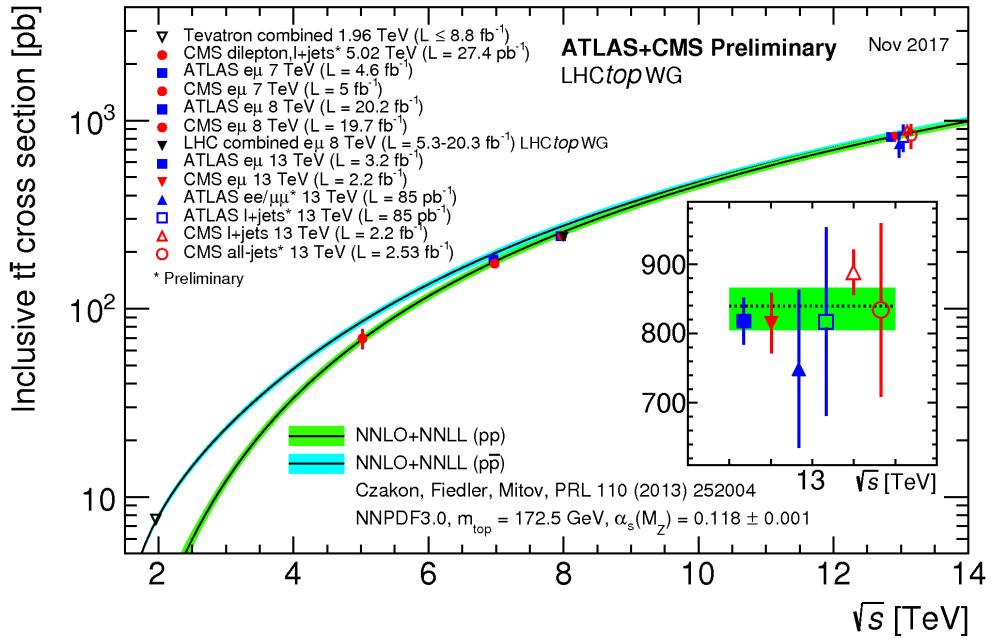


Figure 2.7: Summary of LHC and Tevatron measurements of the top-pair production cross-section as a function of the centre-of-mass energy compared to the NNLO QCD calculation [9].

### 2.3.1 Top decays

The branching fraction of  $t \rightarrow bW$  is predicted to be almost 100% by the SM. The final state of the top quark pair production process is categorised according to the combination of decay modes of the two  $W$ -bosons in the final state. The  $W$  boson decays into a charged lepton and a neutrino with a branching fraction of about 11% for each flavour of leptons. They are observed as an isolated lepton with high transverse momentum and a missing transverse energy in the detector, where the isolation is used to reduce the events with a charged lepton produced from decay of hadrons, especially those containing a  $b$ - and  $c$ -quarks. The  $W$  boson also decays into a pair of quarks with a branching fraction of  $\sim 67\%$ . These quarks are observed as jets in a detector. The jets are explained briefly later in this chapter. The possible combinations of decays of two  $W$  bosons in the final state of the top quark pair production are shown in Fig. 2.8(a). The decay branching ratio of each combination is shown in Fig. 2.8(b).

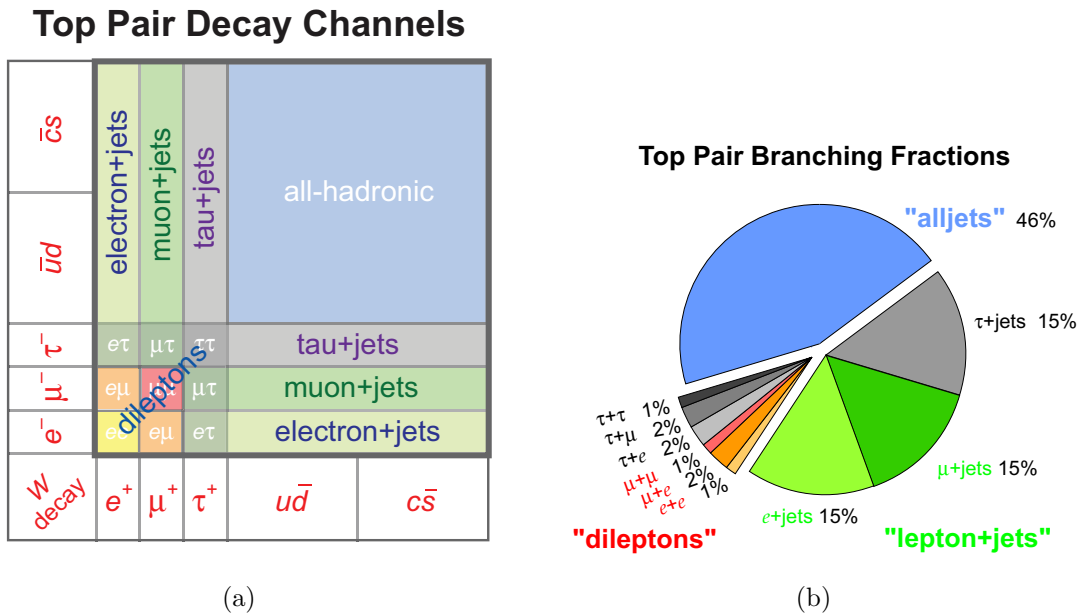


Figure 2.8:  $t\bar{t}$  decay channels and branch ratio [10]

### Leptonic decays

- Lepton+jets channel

Figure 2.9 shows a lepton plus jets decay channel of  $t\bar{t}$ . In this channel, one of the  $W$  bosons decays into a quark pair, while the other decays into a charged lepton and a neutrino. This channel has also a large branching fraction of  $\sim 15\%$  for each lepton flavour,  $e$ ,  $\mu$ , and  $\tau$ . The final state contains a high transverse momentum charged lepton, a missing transverse energy of the neu-

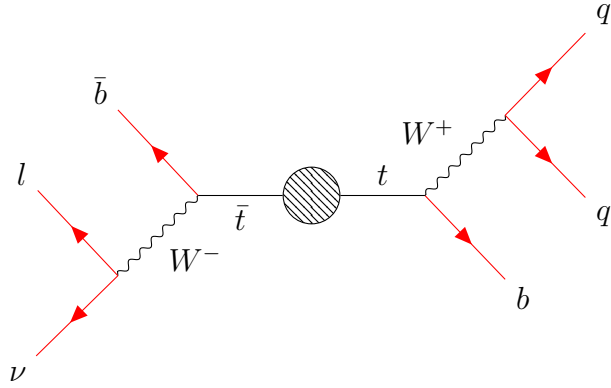


Figure 2.9: Diagram of lepton+jets channel

trino, two light quark jets and two  $b$ -jets, where the  $b$ -jet represents a jet containing a hadron consisting of a  $b$ -quark.

- Di-lepton channel

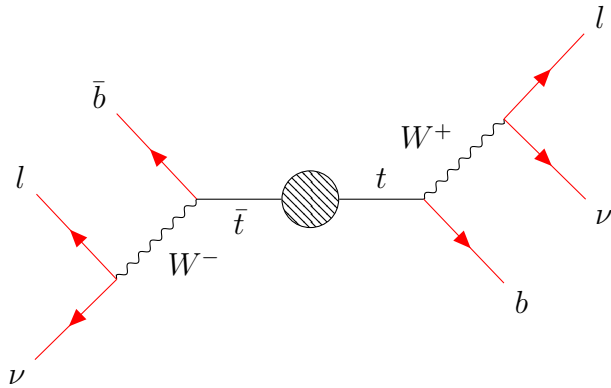


Figure 2.10: Diagram of di-lepton channel

Figure 2.10 shows two leptons decay channel of  $t\bar{t}$ . Both  $W$  bosons decay into a lepton and a neutrino. Two high transverse momentum charged leptons, a large missing transverse energy from two neutrinos and two  $b$ -quark jets are in the final state of this channel. The signal to background ratio is much better than the lepton+jets channel because of the two charged leptons. However, the branching ratio of this channel is much smaller ( $\sim 7\%$ ) for the case where both of the decay leptons are either an electron and a muon. Since it is not possible to uniquely determine the momenta of the two neutrinos in hadron colliders, reconstruction of the  $t\bar{t}$  system in this channel can be done within limited resolution.

## Hadronic decays

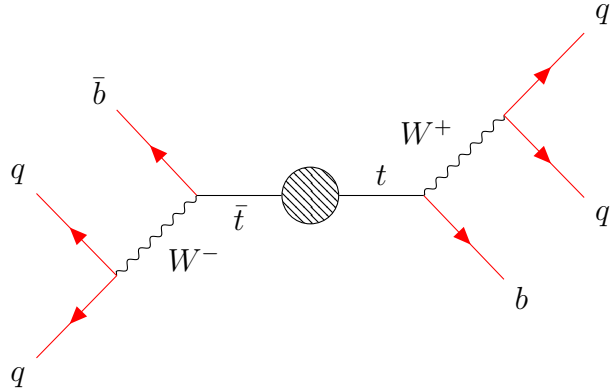


Figure 2.11: Diagram of all-hadronic channel

- All-hadronic channel

Figure 2.11 shows all-hadronic decay channel of  $t\bar{t}$ . In this channel, both  $W$  bosons decay into a quark pair. This leads to six hadronic jets, i.e. two  $b$ -jets plus four light quark jets in its final state. This channel has a large branching ratio of  $\sim 46\%$  as shown in Fig. 2.8(b), but suffers from the large amount of QCD background. With respect to other channels because of the absence of leptons, the reconstruction of  $t\bar{t}$  system for this channel does not involve any missing component in the final state. The estimation of background will be described later in Chapter 6.

Top quarks are detected by reconstructing their decay products. The top quarks from protons collisions are produced by parton interactions. Properties of events calculated using the momentum of partons in the final state is referred to as “parton level” properties. Then top quarks decay into quarks via weak interaction and the quarks are hadronized into stable particles. This step is called “particle level”. In the last step, called “detector level”, the stable particles are observed and reconstructed by interacting with the detector material. An example of a jet from  $b$ -quark, which is produced from  $pp$  collisions, by measuring the energy depositions in calorimeters as shown in Fig. 2.12. Several generator models for predicting the event processes are introduced in Chapter 4. The analysis physics object like the jet in detail will be described in Chapter 5.

## 2.4 Cross Section Measurement

In this thesis, the measurement is performed in the all-hadronic final state of the  $t\bar{t}$  decay. Events in the final state are selected using a series of selection criteria. In an ideal case where all the produced  $t\bar{t}$  pairs are observed by the detector, the  $t\bar{t}$  total cross section is written as:

$$\sigma_{t\bar{t}} = \frac{N_{obs} - N_{bkg}}{\int L dt} \quad (2.3)$$

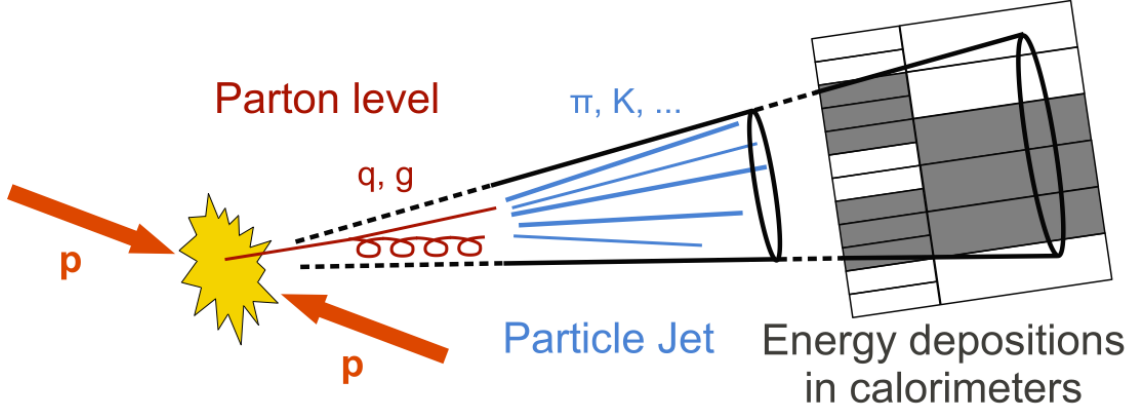


Figure 2.12: A sketch of parton and particle jet [11]

where  $N_{obs}$  is the number of  $t\bar{t}$  events in the all-hadronic final state,  $N_{bkg}$  is the number of background events and  $\int L dt$  is the integrated luminosity. Differential cross sections as a function of physical observable  $X$ ,  $d\sigma^{t\bar{t}}/dX$ , can also be measured by dividing the cross section within a small interval of  $X_i$  divided by the interval with  $\Delta X_i$ .

General goal of this study is to make precision test of QCD by comparing the experimental measurement with the SM theoretical prediction. Although the SM is greatly successful, we still need to verify every corner of it by measurement. Through measurement of differential cross sections, more details of model description can be verified, especially in kinematic regions which have not been explored so far. This gives feedback to theoretical models. Furthermore, effects beyond SM can appear as modification of  $t\bar{t}$  differential distribution with respect to the SM predictions, which may not be detected with an inclusive cross section measurement.

This analysis with all-hadronic channel uses boost object to test SM in high invariant mass ( $> 1\text{TeV}$ ). This measurement, therefore, explores the top quark interaction in the energy range much beyond the mass of the top quark. It can also be used to check consistency with measurement in other channels. Further, a well-established  $t\bar{t}$  sample can effectively be used to understand the physics objects reconstructed in the ATLAS detector.

# Chapter 3

## The ATLAS experiment

### 3.1 The Large Hadron Collider

The Large Hadron Collider (LHC) is currently the highest energy hadron collider in the world, located at the France-Swiss border as illustrated in Fig. 3.1. There are four large experiments utilizing the LHC collisions. Compact Muon Detector (CMS) and ATLAS are the general purpose detectors. ALICE is designed to study heavy ion collision physics, while LHCb focuses on the  $b$ -quark physics studies.

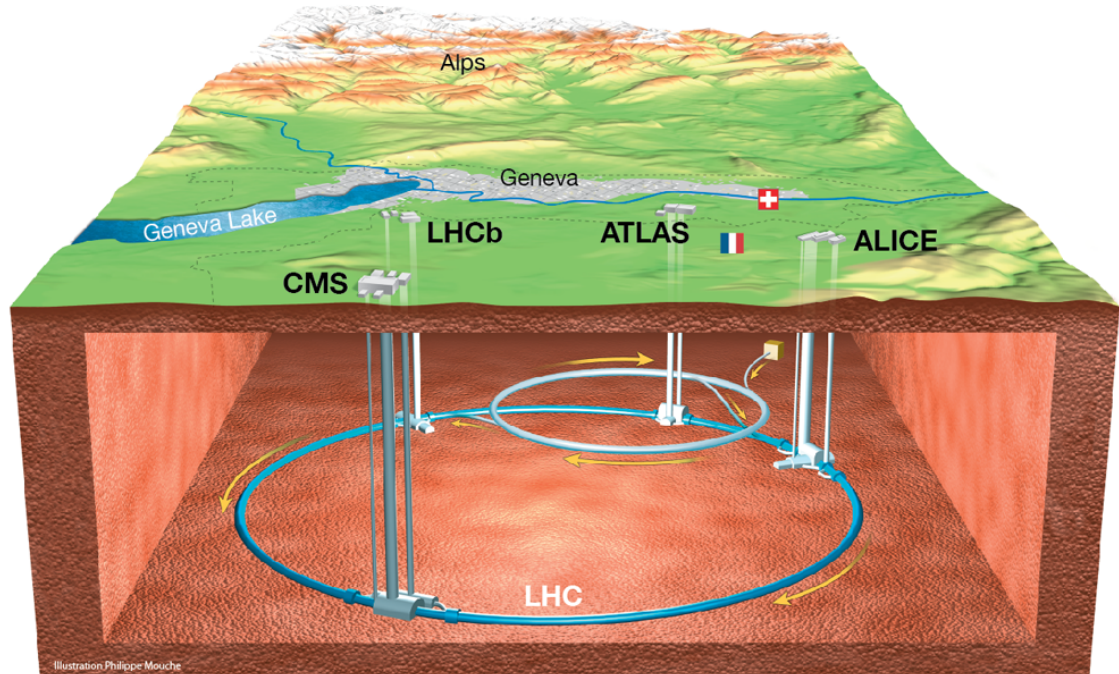


Figure 3.1: The overview of LHC [12]

## 3.2 The ATLAS detector

The ATLAS experiment at the LHC is a multi-purpose detector with a forward-backward symmetric cylindrical geometry and nearly  $4\pi$  coverage in solid angle. The overview of the ATLAS detector is shown in Fig. 3.2. From center to the outside, it consists of an inner tracking detector surrounded by a superconducting solenoid magnet creating a 2T axial magnetic field, electromagnetic and hadronic calorimeter and a muon spectrometer. The particle detection in the sub-detectors is illustrated in Fig. 3.3. The inner tracking detector covers the pseudorapidity range  $|\eta| < 2.5$ . The inner track detector consists of silicon pixel, silicon micro-strip and transition radiation tracking detectors, and serves for reconstructing the trajectories of the charged particles produced in the  $pp$  interactions with high precision and efficiency. Lead/liquid-argon (LAr) sampling calorimeters provide electromagnetic (EM) energy measurements with high granularity and longitudinal segmentation. A hadronic calorimeter covers the central pseudorapidity range ( $|\eta| < 1.7$ ). The endcap and forward regions are instrumented with LAr calorimeters for both EM and hadronic energy measurements up to  $|\eta| = 4.9$ . The muon spectrometer is located outside of the calorimeter systems. It includes a system of precision tracking chambers and detectors with sufficient timing resolution for triggering events.

The details for subdetectors are described in next sub-sections.

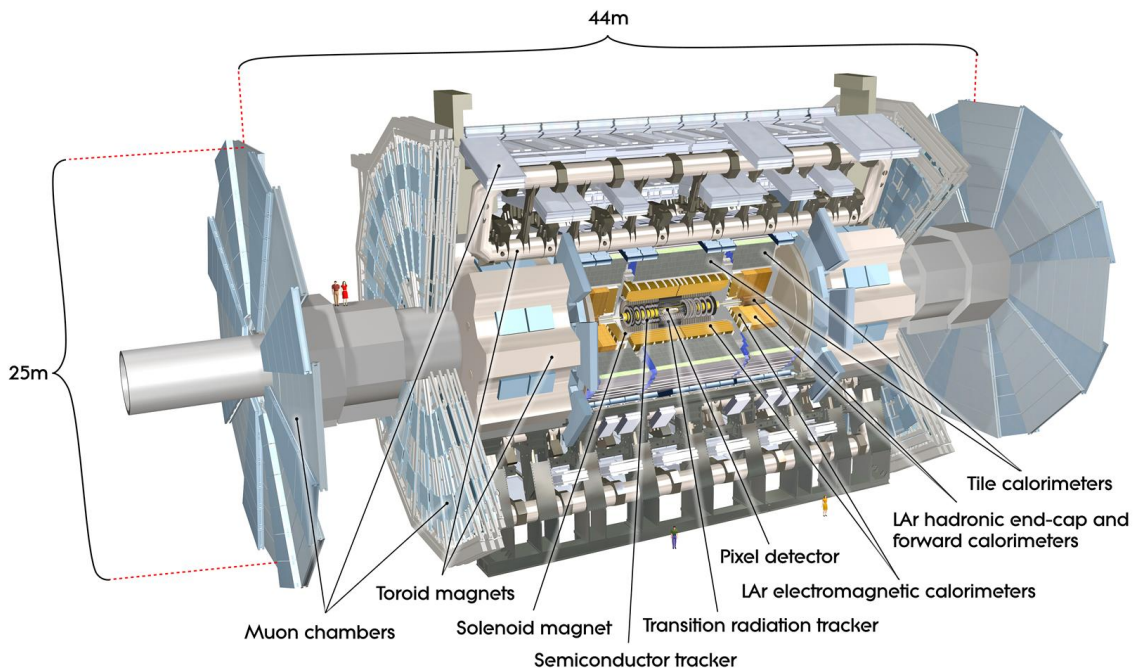


Figure 3.2: ATLAS detector [13]

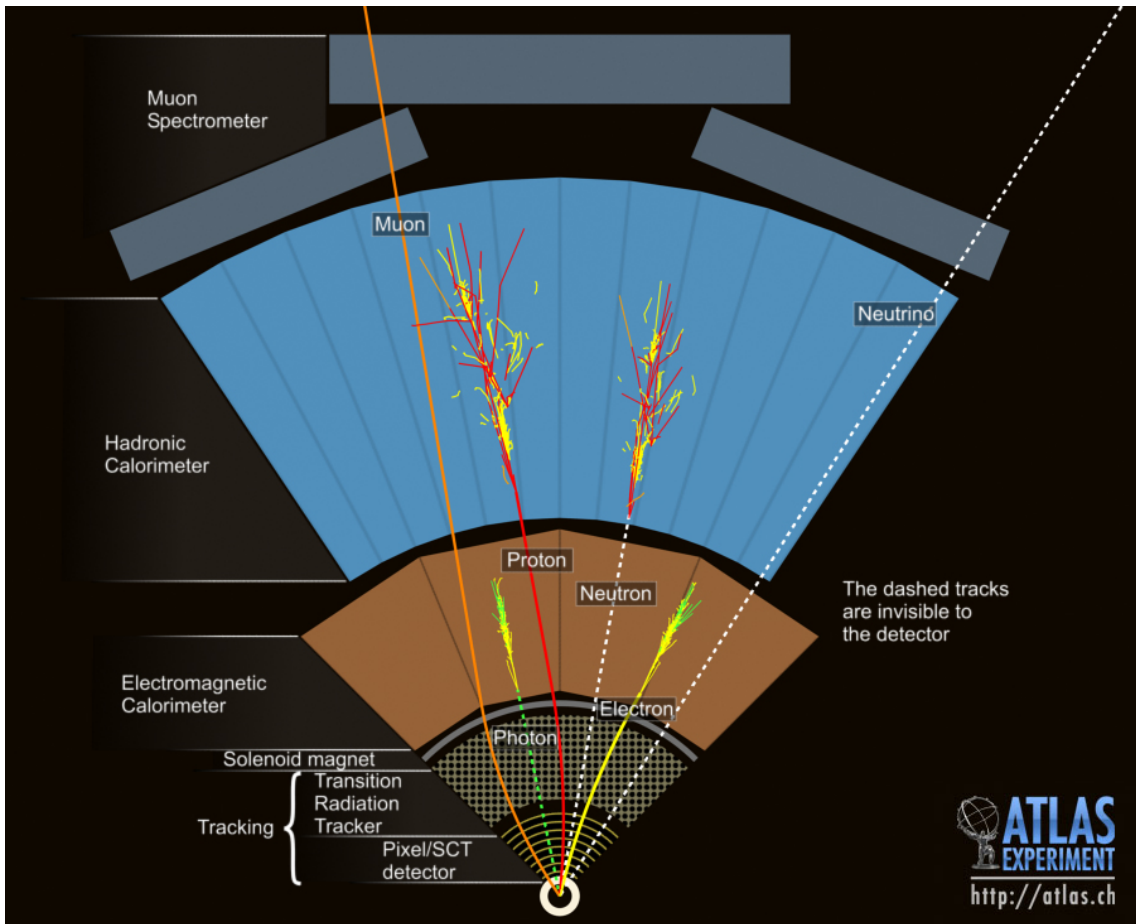


Figure 3.3: Particle detection in the ATLAS detector [14]

### 3.2.1 The coordinate system

The right-handed coordinate system is used in ATLAS. The  $z$  direction is defined along beam axis. The nominal interaction point is the origin. The ATLAS detector is divided into two sides according to the sign of  $z$  axis. The beam direction is counterclockwise from left to right in the ATLAS detector as shown in Fig. 3.4(a): A-side with positive  $z$  (toward Geneva) and C-side with negative  $z$  (toward France). The  $x-y$  plane is transverse to the beam. The positive  $x$ -direction points toward the center of the LHC ring. The positive  $y$ -direction points approximately the zenithal direction to form right-handed Cartesian coordinate system. The corresponding cylindrical coordinate system is illustrated in Fig. 3.4(b). The pseudorapidity  $\eta$  provides a convenient coordinate system. It is defined as

$$\eta = -\ln\left(\tan\frac{\theta}{2}\right), \quad (3.1)$$

where  $|\eta| < 1.05$  is barrel region,  $|\eta| > 1.05$  is endcap region. The rapidity is defined as

$$y = \frac{1}{2} \ln\left(\frac{E + p_z}{E - p_z}\right), \quad (3.2)$$

where  $E$  is the energy of a particle, and  $p_z$  is the component of momentum along the beam axis. The difference in rapidity of any two particles is independent of the Lorentz boost. Transverse momentum,  $p_T = |\vec{p}_T|$ ,  $\vec{p}_T = (p_x, p_y, 0)$  is defined as the momentum component perpendicular to the beam.

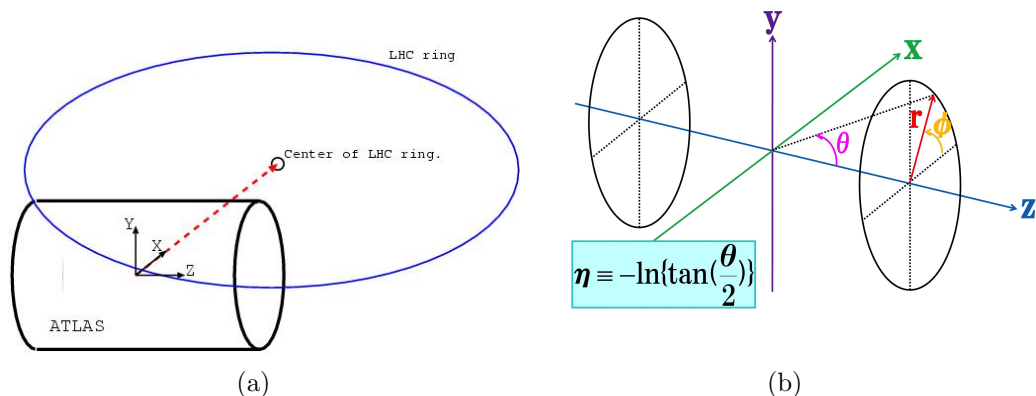


Figure 3.4: ATLAS coordinate system

### 3.2.2 Inner Detector

The inner detector is designed to give precision measurement of particle positions and momenta. It is immersed in a 2T solenoid magnetic field, which is located closest to beam interaction point with the pseudorapidity coverage  $|\eta| < 2.5$ . It

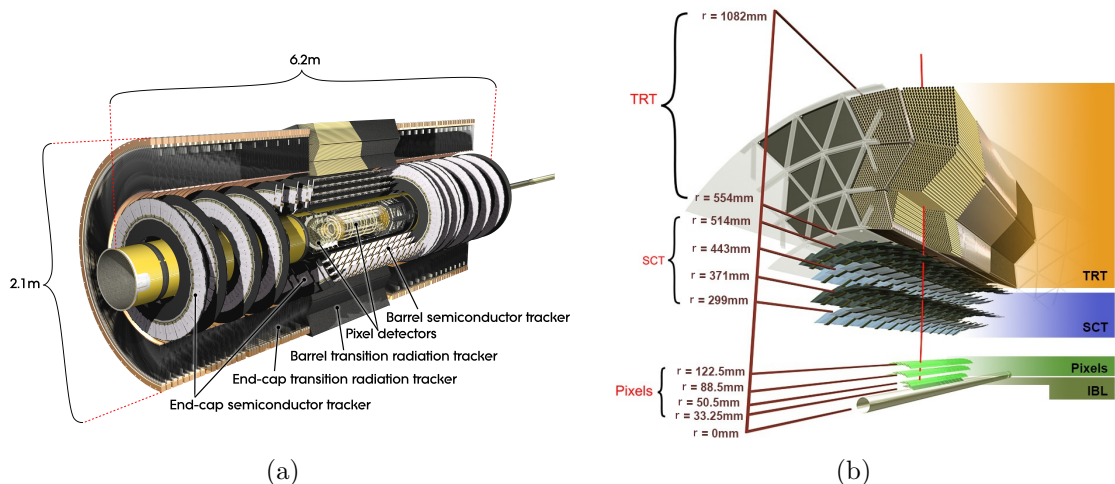


Figure 3.5: The schematic drawing of inner detector [15]

consists of Pixel (with Insertable B-layer), Silicon strip and Transition radiation detectors as shown in Fig. 3.5.

**Pixel: Silicon-pixel vertex detector** The pixel detector has position resolution of  $10 \mu\text{m}$  in  $r - \phi$  direction and  $115 \mu\text{m}$  in  $z$  direction to determine interaction point and vertices. The size of a pixel is  $50 \times 400 \mu\text{m}^2$ . There are a total of  $\sim 80 \text{ M}$  readout channels. After Run1, the insertable B-layer (IBL) was installed as the fourth layer between a new beam pipe and the inner most Pixel layer, located closer to the interaction point ( $33.25 \text{ mm}$  from the beam axis) in order to improve the tracking performance. Figure 3.6 describes the definition of track impact parameters. The  $d_0$  is the transverse impact parameter, where the resolution of which is  $\sigma_{d_0}$ ,  $z_0$  is the longitudinal impact parameter with respect to the primary vertex, and  $\theta$  is the polar angle of the track. As shown in Fig. 3.7, the transverse impact parameter ( $d_0$ ) resolution has been improved with the IBL, in particular for the low  $p_T$  region.

**SCT: Semi-Conductor Tracker** The SCT is located at the outside of the pixel detector. It consists of 4088 modules tilling four coaxial cylindrical layers in the barrel region and two endcaps each containing nine disk layers. The module consists of strip silicon detector to form stereo layer. The modules cover a surface of  $63 \text{ m}^2$  and provide hermetic coverage with precision space-point measurement. The position resolution for  $r - \phi$  direction is  $16 \mu\text{m}$  and for  $z$  direction is  $580 \mu\text{m}$ .

**TRT: Transition Radiation Tracker** The TRT is located at the outside of the SCT detector, consisting multi-layers of gaseous straw tube elements. There are 73 layers of straws in the barrel and 160 layers in the endcaps. The tube diameter is  $4 \text{ mm}$ , filled with mixed gas ( $\text{Xe} : \text{CO}_2 : \text{O}_2 = 70 : 27 : 3$ ). It provides to detect an  $X$ -ray photon of transition radiation from electrons as well as ionization by charged particles. The position resolution of a tube is  $130 \mu\text{m}$ .

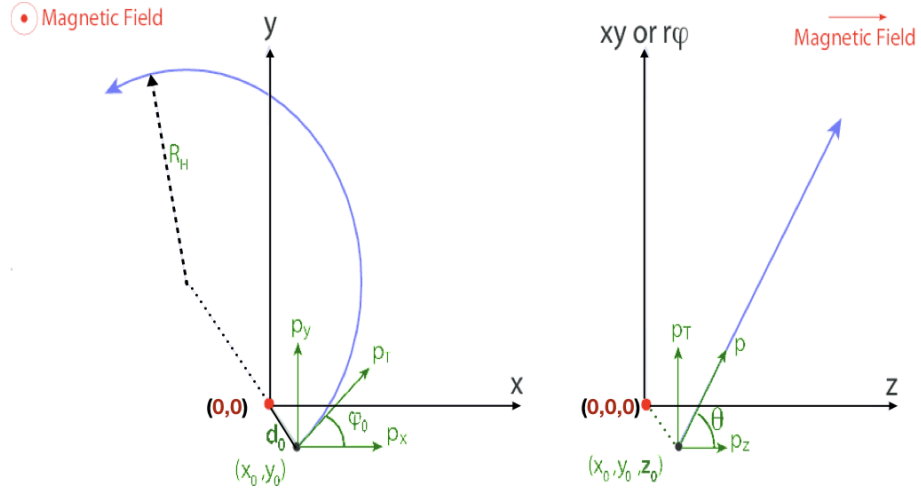


Figure 3.6: The definition of transverse and longitudinal track parameters [16].

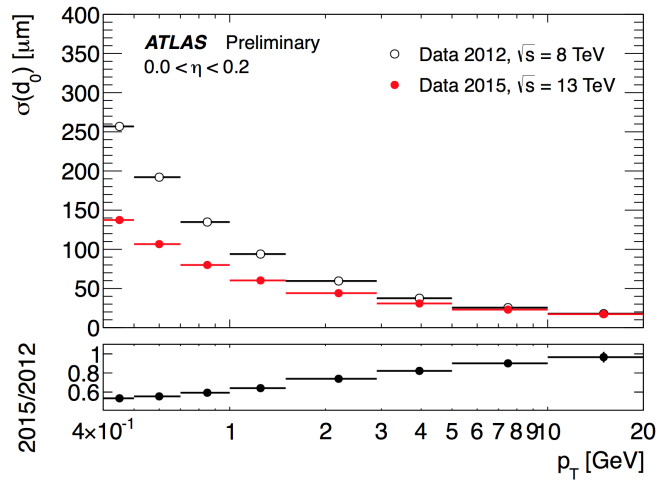
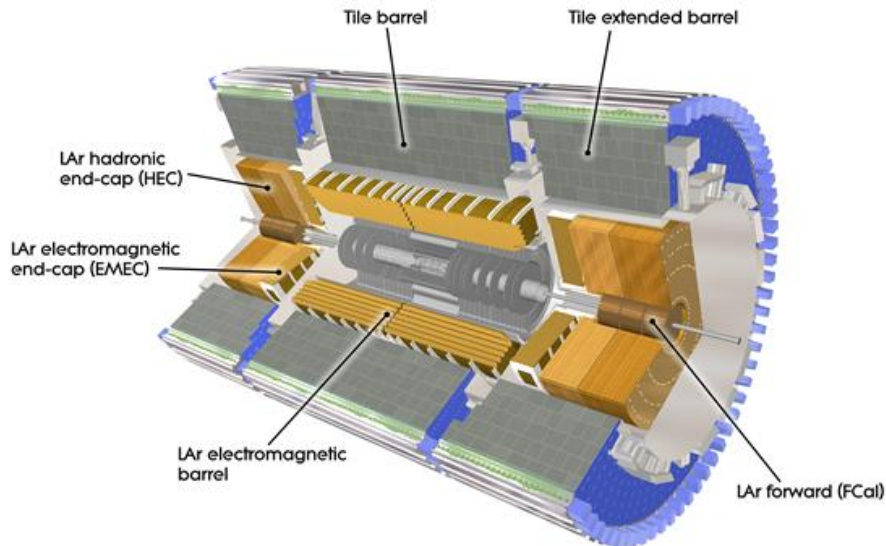


Figure 3.7: The comparison of  $d_0$  resolution without (2012) and with (2015) IBL [17].

### 3.2.3 Calorimeters

A schematic picture of the ATLAS calorimeters is shown in Fig. 3.8. The purpose of the calorimeters is to measure the energy and position of the electron, photon and hadrons. It consists of electromagnetic calorimeter system and a hadronic calorimeter system, the sensitive region of which is  $|\eta| < 4.9$ .



(a)

Figure 3.8: Overview of the Calorimeter [15]

**Electromagnetic calorimeter** The EM calorimeter consists of liquid argon (LAr) sampling calorimeters using Pb as the absorber with accordion shape illustrated in Fig. 3.9. It is positioned in the barrel region ( $|\eta| < 1.5$ ), and the endcap region ( $1.4 < |\eta| < 3.2$ ). This system measures the energy and position of a particle interacting via electromagnetic force. The energy resolution is  $\sigma_E/E \sim 10\%/\sqrt{E} \oplus 0.7\%$ .

**Hadronic calorimeter** The hadronic calorimeters cover the range  $|\eta| < 4.9$  through different techniques for widely varying requirements and radiation environment over the large  $\eta$  range. It consists of the Tile calorimeter and LAr Hadronic Endcap Calorimeter. It provides the energy resolution of  $\sigma_E/E \sim 50\%/\sqrt{E} \oplus 3\%$ .

- **Hadronic Tile Calorimeter** It is located outside of the EM calorimeter covering the pseudorapidity range of  $|\eta| < 1.7$ , which is a sampling calorimeter using steel as the absorber and plastic scintillator for sampling.
- **Hadronic Endcap Calorimeter** It is positioned behind the endcap LAr EM calorimeter with the pseudorapidity range of  $1.5 < |\eta| < 3.2$  using copper as the absorber and LAr for sampling. The wheels of copper absorber plates

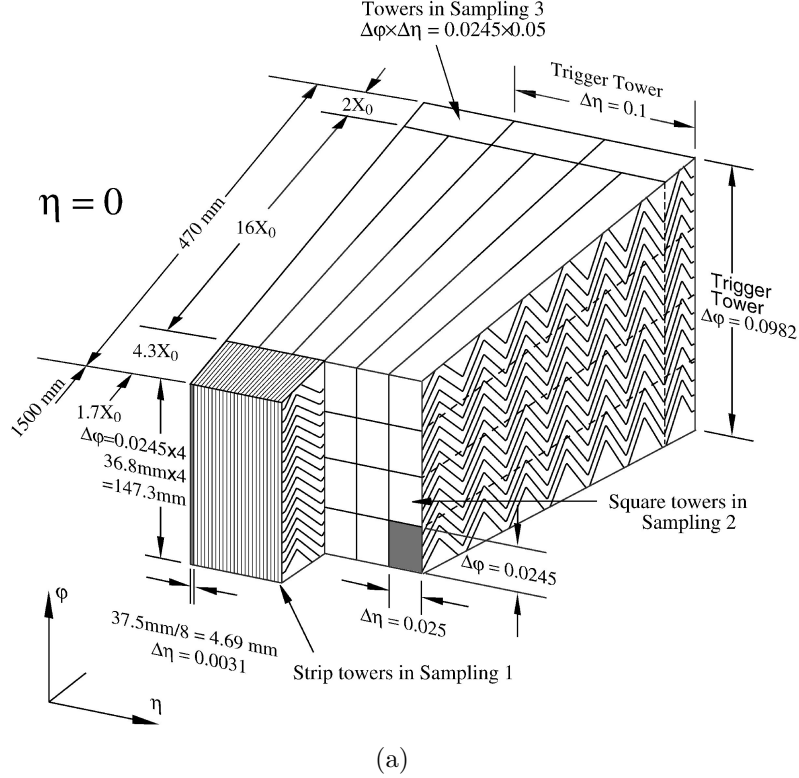


Figure 3.9: Accordion structure for the ATLAS EM calorimeter [18]

have cylindrical structure with outer radius of 2030 mm and grouped into two segments in depth. The front segment is made of 24 copper plates of 25 mm thick, and the rear segment consists of 16 copper plate of 50 mm thick.

The total thickness of the EM calorimeter is  $> 22$  radiation length ( $X_0$ ) in the barrel and  $> 24 X_0$  in the endcap. The approximate  $9.7$  interaction length ( $\lambda$ ) of active calorimeter in the barrel and  $10 \lambda$  or more in the endcap, is adequate to provide good resolution for high energy jets. Figure 3.10 shows the average energy response as a function of detector  $\eta_{det}$  for jets of a truth jet energy of different  $p_T$ , where the average energy response is defined as the mean of a Gaussian fit to the  $E_{jet}^{reco} / E_{jet}^{truth}$  distribution. Gaps and transitions between calorimeter subdetectors result in a lower energy response due to absorbed or undetected particles, evident when parameterized by  $\eta_{det}$ .

### 3.2.4 Muon Spectrometer

The Muon Spectrometer is designed to detect muons. It is located at the outermost of subsystems of the ATLAS detector. The layout is shown in Fig. 3.11(a) and 3.11(b). It consists of high precision tracking chambers for measuring the momentum and trigger chambers for fast readout to provide trigger decision. They are grouped to inner, middle and outer stations from the ATLAS detector center to outside.

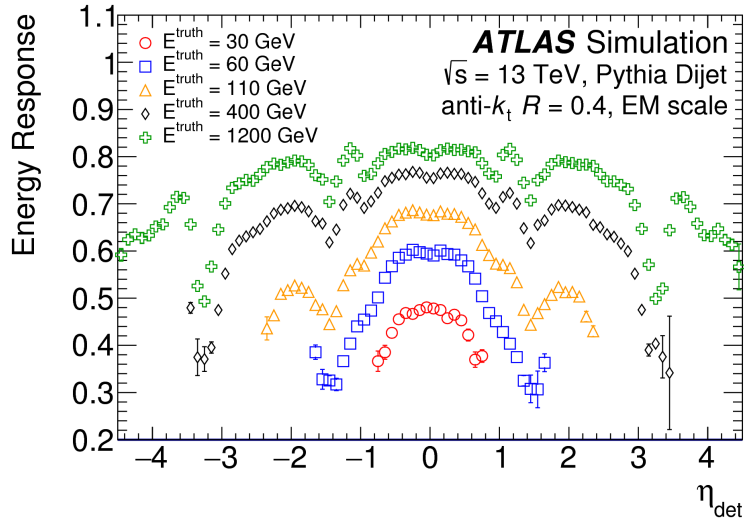


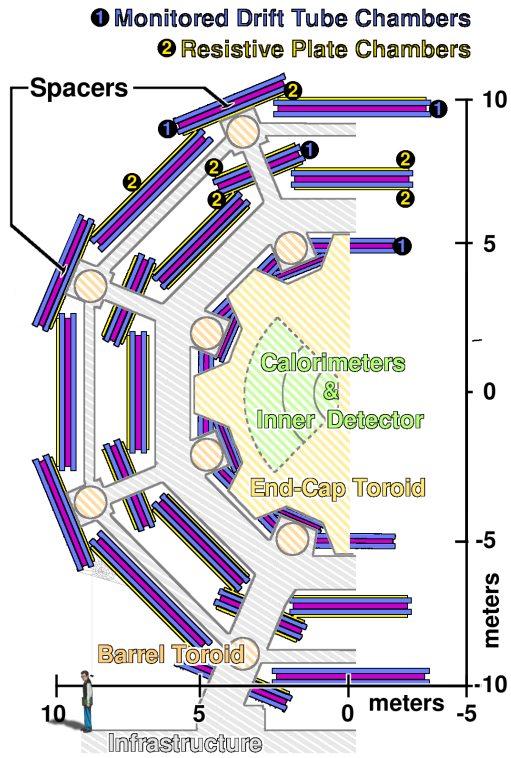
Figure 3.10: The average energy response as a function of  $\eta_{det}$  for jets of a truth energy of 30, 60, 110, 400, and 1200 GeV [19]

**Trigger Chambers** Two kinds of gas detectors are used for Level-1 trigger as illustrated in Fig. 3.12. The RPC is responsible for barrel region ( $|\eta| < 1.05$ ) and the TGC is responsible for endcap region ( $1.05 < |\eta| < 2.7$ ).

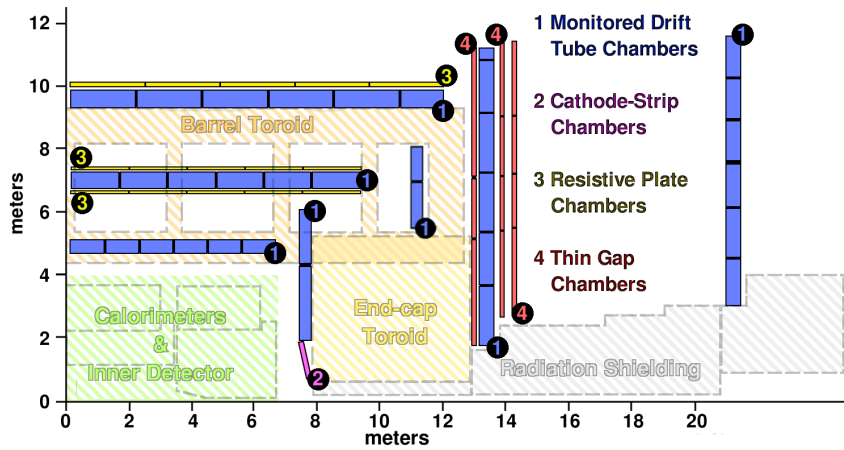
- **TGC: Thin Gap Chamber** The TGC covers the pseudorapidity range of  $1.05 < |\eta| < 2.7$ . It is a multiwire proportional chamber using a gas mixture of  $\text{CO}_2$  and  $\text{C}_5\text{H}_{12}$ . Both cathode strips and anode wires are read out. Since the cathode strip is orthogonal to the anode wire, two-dimensional positions can be measured. The position resolution in  $r$  direction is 2 – 6 mm and in  $\phi$  direction is 3 – 7 mm.
- **RPC: Resistive Plate Chamber** The RPC is used in the barrel region with the pseudorapidity range of  $|\eta| < 1.05$ . It is gas filled chamber consisting of resistive plates with 2 mm gaps, operated in streamer mode. Signal is read out by strips. It is a gaseous detector using a gas mixture of  $\text{C}_2\text{H}_2\text{F}_4$  and  $\text{SF}_6$ . It can also measure the two-dimensional positions because of orthogonal strips. The position resolution is 10 mm for both in  $z$  and  $\phi$  direction.

**Precision Tracking Chambers** MDT and CSC chambers are used to reconstruct a muon track when a muon passes through these chambers.

- **MDT: Monitored Drift Tube** The MDT covers the pseudorapidity range of  $|\eta| < 2.7$ . It consists of multi-layers of aluminum tubes with the structure shown in Fig. 3.13. A tube is filled with a gas mixture of Ar and  $\text{CO}_2$  and is with 30 mm outside diameter and a  $50 \mu\text{m}$  diameter central W-Re wire. Each tube has position resolution of about  $80 \mu\text{m}$ . Except the inner station of endcap where the number of layer of tubes is eight, the stations have six tube layers. Each station has position resolution of  $\sim 35 \mu\text{m}$ .



(a)



(b)

Figure 3.11: Muon spectrometer projected on (a): the  $x$ - $y$  plane; (b): the  $r$ - $z$  plane [20].

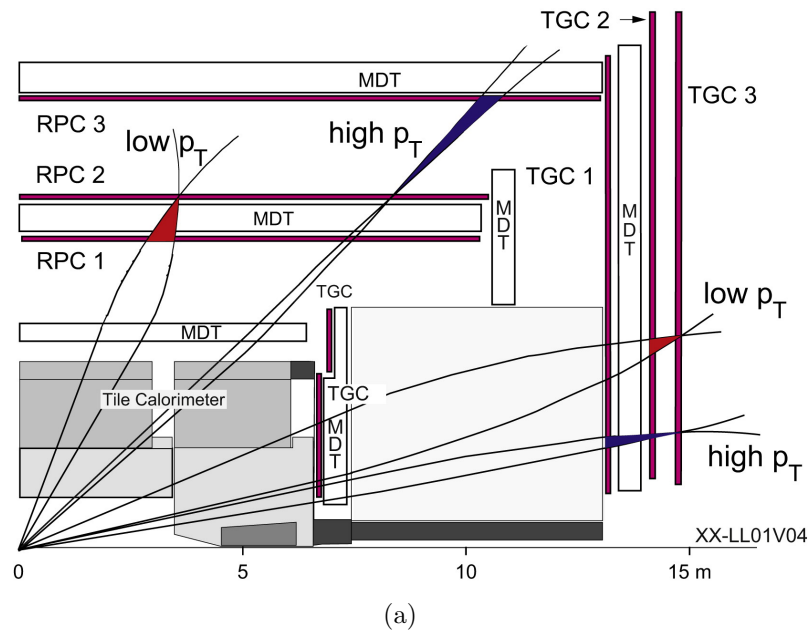


Figure 3.12: The schematic view of the muon trigger system [21]

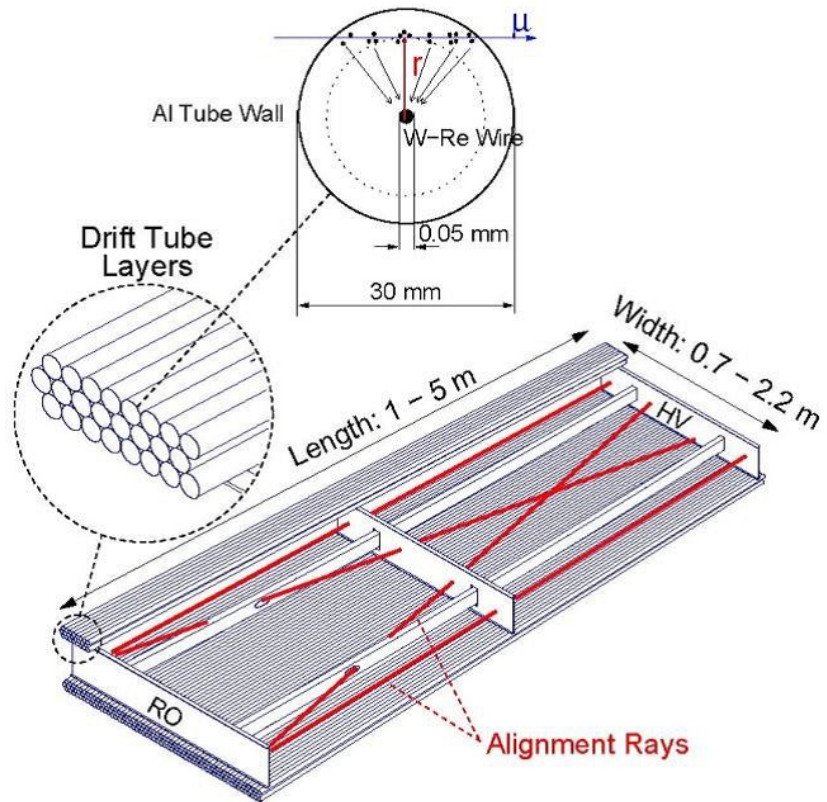


Figure 3.13: The MDT structure

- CSC: Cathode Strip Chamber** The CSC is multiwire proportional chamber measuring the charge induced on the segmented cathode by the avalanche formed on the anode wire to obtain the track position. Since the rate capacity of the CSC ( $1000 \text{ Hz/cm}^2$ ) is higher than the MDT ( $150 \text{ Hz/cm}^2$ ), it is placed in the inner station. It covers high pseudorapidity range ( $2.0 < |\eta| < 2.5$ ) close to the beam line. The position resolution of the CSC is  $40 \mu\text{m}$  in  $r$  direction.

### 3.2.5 Magnet System

In order to measure the momentum of a charge particle, two kinds of superconducting magnets, solenoid and toroid, provide magnetic field in the ATLAS detector. The schematic view is shown in Fig. 3.14.

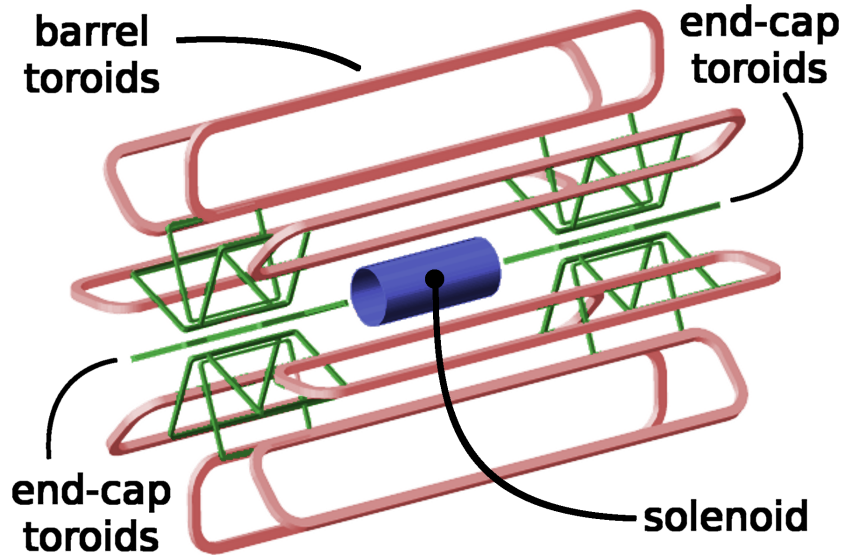
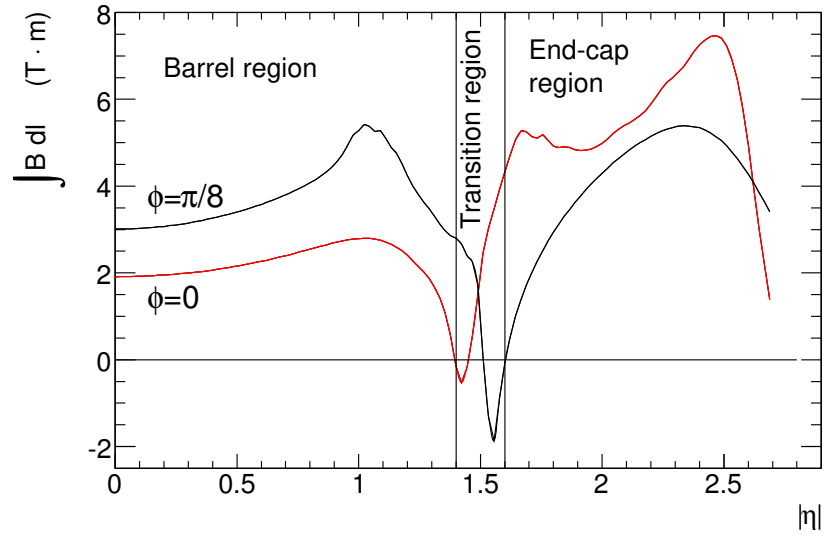


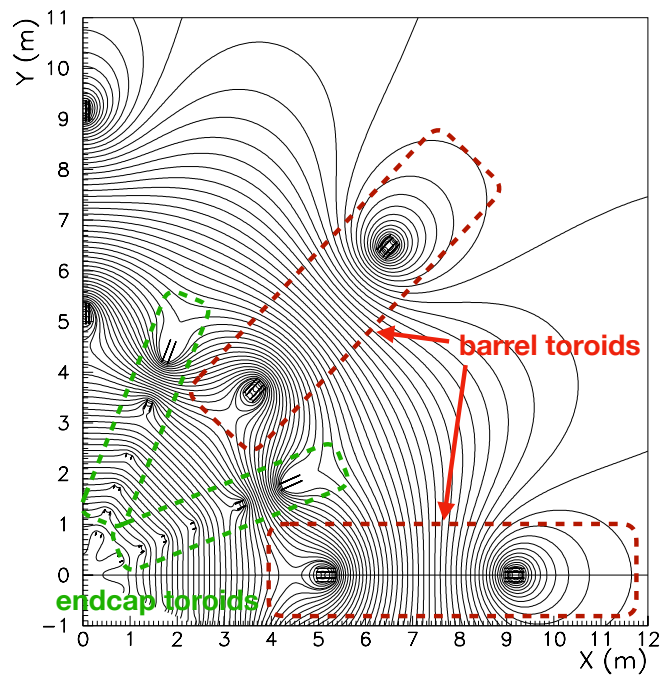
Figure 3.14: A schematic view of ATLAS magnet system [20]

**Solenoid Magnet** It is installed in between the Inner Detector and the calorimeter with a length of 5.3 m and a radius of 1.2 m. It provides 2 T magnetic field for charged tracks measured by the Inner Detector.

**Toroidal Magnet** The toroidal magnet system is constituted by a barrel toroid and two endcap toroids. The barrel toroid provides 0.5 T magnetic field in  $\phi$  direction for barrel region ( $|\eta| < 1.05$ ) with a length of 25.3 m, an inner core of 9.4 m and an outer diameter of 20.1 m. Similarly, the endcap toroids provide 1 T magnetic field in  $\phi$  direction for endcap region. There is a complicated magnetic field from the overlap between the barrel and endcap toroids in the pseudorapidity range of  $1.4 < |\eta| < 1.6$  as shown in Fig. 3.15. It is called transition region.



(a)



(b)

Figure 3.15: (a):  $\eta$  V.S. magnetic field; (b): magnetic field line in  $\phi$  direction [18]

### 3.3 ATLAS Trigger and Data Acquisition System

The ATLAS trigger and data acquisition system is designed to effectively collect as many interesting events as possible using two trigger levels, Level 1 and High Level Trigger. The first level hardware-based trigger uses a subset of the detector information to reduce the rate of accepted events to a design maximum of 100 kHz. This is followed by a software-based trigger system performed on a computer farm with a maximum average accepted event rate of about 1 kHz. The trigger scheme is illustrated in Fig. 3.16. The details are described below.

**Level-1 Trigger** The Level-1 trigger is to reduce the event rate from initial bunch-crossing rate of 40 MHz to 100 kHz by using signal from the calorimeter and muon detectors. The signals are processed by dedicated hardware to meet the requirement of the maximum latency of  $2.5 \mu\text{s}$ . A new topological trigger (L1Topo), which enables the Level-1 trigger to combine kinematics information from calorimeter and muon trigger objects, was installed for Run2 with higher collision energy ( $\sqrt{s} = 8 \rightarrow 13 \text{ TeV}$ ) and higher luminosity with about twice higher the event rate in Run1. The L1Topo is used to trigger, for instance, on high mass di-jet from vector boson fusion processes. To suppress pile-up effects, the preprocessor of calorimeters were replaced to FPGA from ASIC for Run2. In order to suppress the fake muons further, muon endcap trigger requires the coincidence with hits from the inner station [22].

**High Level Trigger** High level trigger uses software to discard non-interesting events by refining the reconstruction of physics objects, such as electron, muon, jet etc, found in the angular regions-of-interest (RoI) identified by the Level-1 trigger. A seed is constructed for each trigger accepted by Level 1, which consists of a  $p_T$  threshold and an  $\eta - \phi$  position. For example, in L2MuonSA algorithm, which is the first step of the muon HLT algorithm uses a window of this seed to reconstruct the muon track in the MDT and CSC chambers and measure the momentum. These track properties are used to refine the events. The HLT processing time is about 0.2 s on average. The final accepted event rate is reduced to  $\sim 1.5 \text{ kHz}$ .

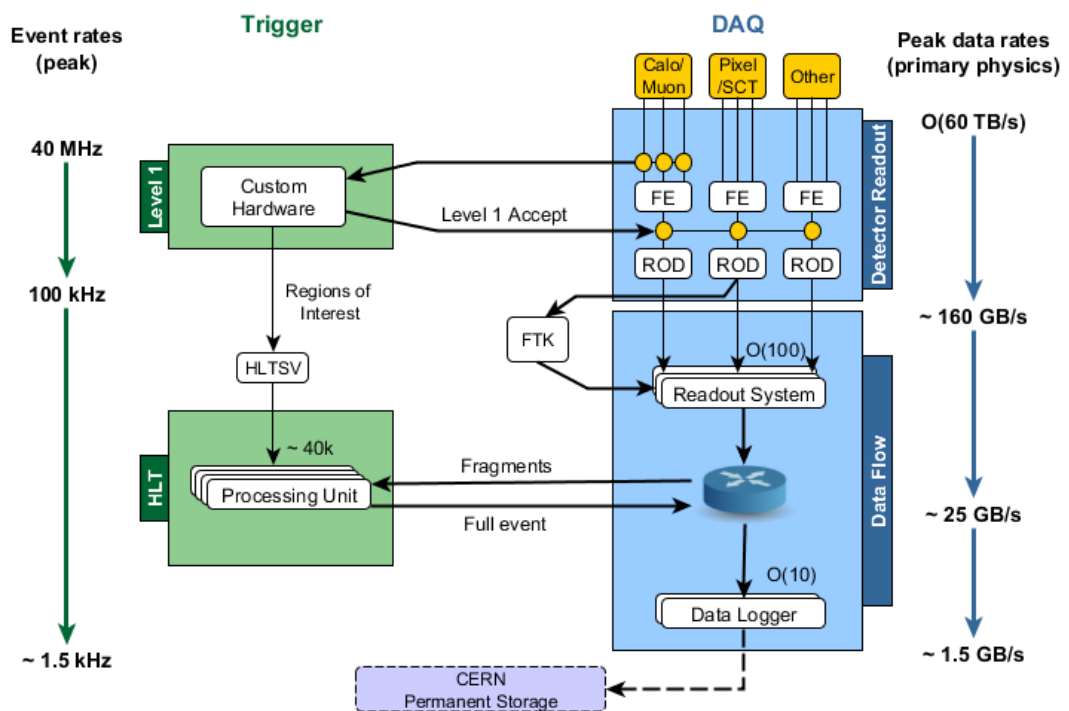


Figure 3.16: The schematic of ATLAS TDAQ system in Run-2 [23].

**Data Quality (DQ)** The DQ monitoring is responsible for assuring the quality of data taking and providing information on periods of data taking where the quality of the data is adequate for physics analysis. The DQ monitoring is done for each detector objects such as jets and muons as well as for each detector subsystem. There are two systems for DQ monitoring, online and offline. Two tools are provided perform the online DQ monitoring:

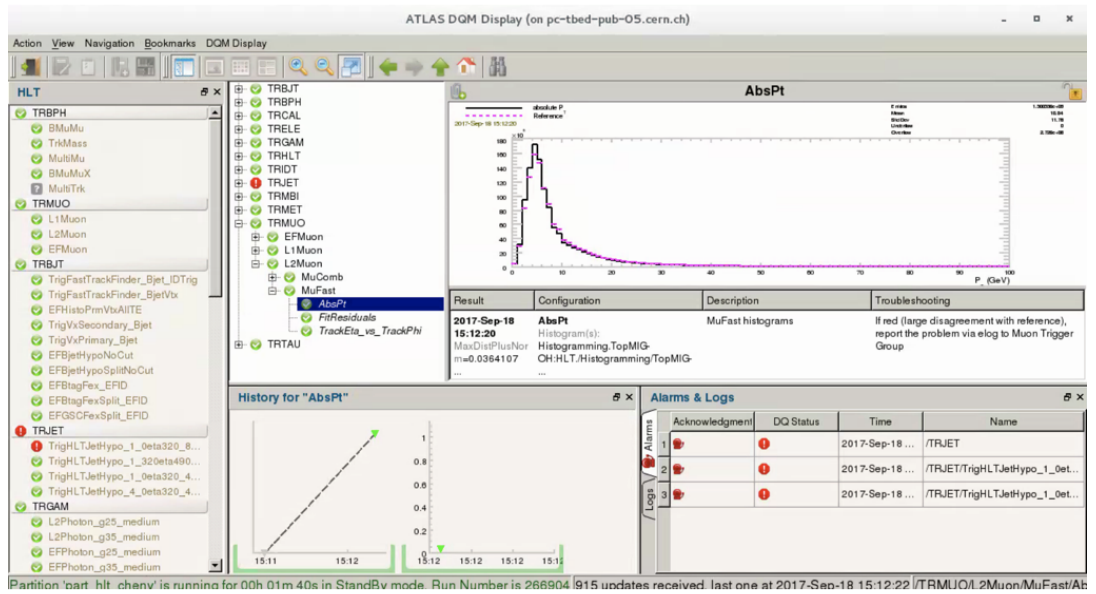
- **DQMF:** The Data Quality Monitoring Framework is the online framework for data quality assessment. It analyses histograms through user-defined algorithms and relays the summary of this analysis in the form of DQ flags. Results are visualized with the DQMD (Data Quality Monitoring Display). The framework is based on xml configuration files.
- **OHP:** The Online Histogram Presenter allows for histogram visualization. It displays a set of pre-defined monitoring histograms. It is also based on xml configuration files, which reside at ATLAS control room and can be directly edited there.

The example of DQMD for HLT muons is shown in Fig. 3.17(a). The ongoing run is compared to a past good run to raise a flag in case of anomaly. For example, the flag of the red exclamation mark in the jet part indicates potential problem, to call for attention of experts to investigate the situation.

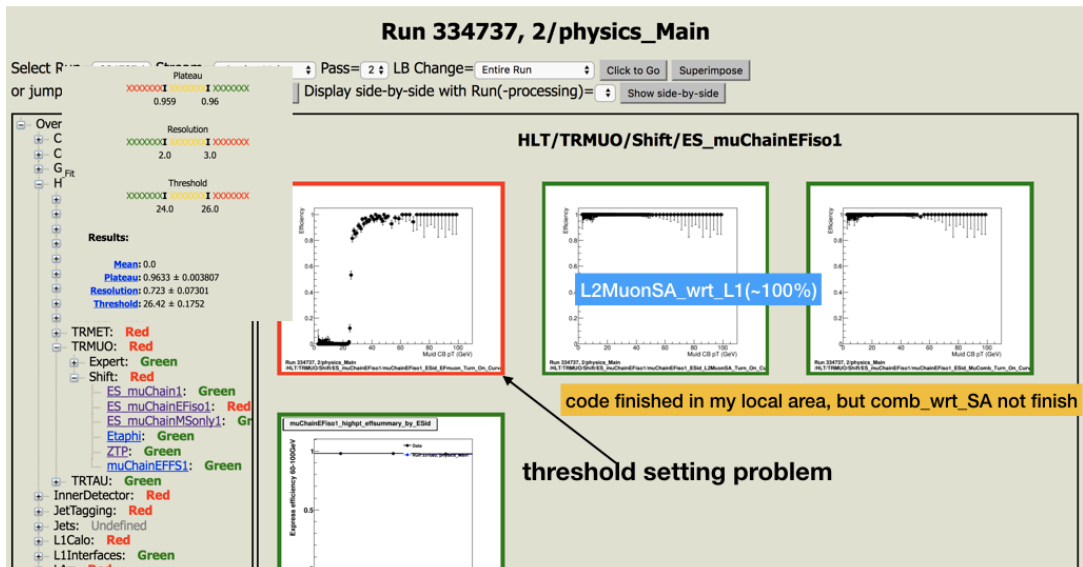
The online data quality monitoring mainly guides the experts to debug the trigger system as quickly as possible. The data quality assessment for physics analysis is performed by the offline DQ, which uses the full data information of all the data saved offline after reconstruction jobs. The runs were signed-off by checking the histograms, e.g. efficiency, which are rapidly processed and available within 24 hours after a run finished. The example of offline DQ display is shown in Fig. 3.17(b), where the flags are raised by user-defined algorithms.

### 3.4 Luminosity measurement

Precise luminosity is measured bunch-by-bunch with the two luminosity detectors [24], BCM (Beam Conditions Monitor) and LUCID (LUminosity measurement using a Čerenkov Integrating Detector). The BCM consists of four  $8 \times 8 \text{ mm}^2$  diamond sensors ( $\sim 1 \text{ cm}^2$ ) arranged around the beam pipe at  $z = \pm 184 \text{ cm}$  on each side of the ATLAS interaction point. LUCID is a Čerenkov detector, located at distance of  $\pm 17 \text{ m}$  from the interaction point, covering the pseudorapidity range of  $5.6 < |\eta| < 6.0$ . The calibration of luminosity is performed by the beam separation scan (Van der Meer method [25]). The luminosity has been measured with a precision of 2.1% (2.2%) for the data acquired in 2015 (2016). The luminosity recorded by the ATLAS detector. It shows that the data taking for year 2017 went well as shown in Fig. 3.18.



(a)



1

(b)

Figure 3.17: (a) Online DQ for DQMD, (b) Offline DQ webdisplay.

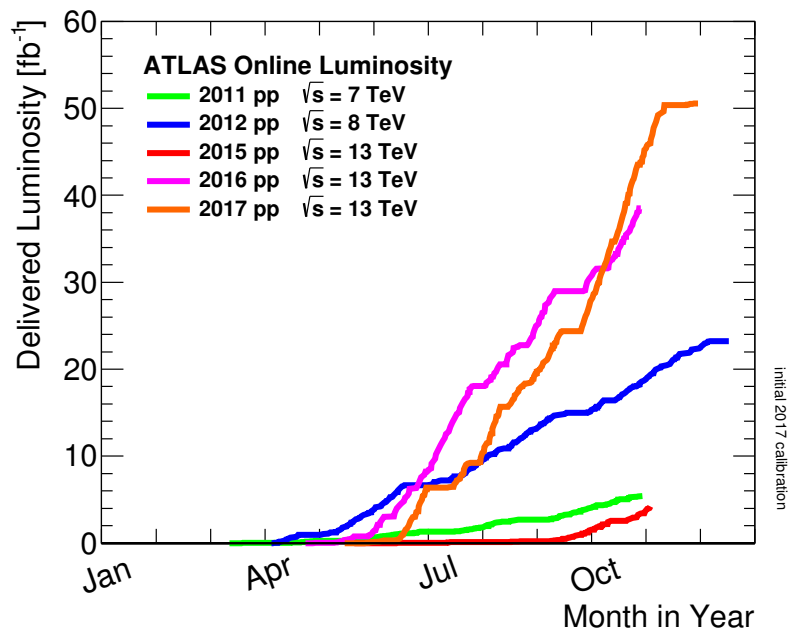


Figure 3.18: Delivered Luminosity V.S. time for 2011-2017 in pp collisions [26].

# Chapter 4

## Datasets and Simulated Samples

This chapter explains about the data sample in this analysis. Simulated sample using Monte Carlo method are also described, which are used to predict the signal and estimate the background and modelling uncertainties.

### 4.1 Data sample

Figure 4.1 shows distribution of number of pile-ups from 2015 to 2017, indicating the number of interactions per bunch crossing as illustrated in Fig. 4.2. The structure in Fig. 4.1 is a reflection of bunch size profile for each year. Figure 4.3 shows an example of event display with two pile-ups in  $pp$  collisions. The data samples of 2015 and 2016 is used in this analysis, corresponding to an integrated luminosity of  $36.1 \text{ fb}^{-1}$  at a center-of-mass energy  $\sqrt{s} = 13 \text{ TeV}$ . Only data taken under stable beam conditions and with fully operational subdetectors are considered, i.e. the data must be validated by the Data Quality described in Section 3.3.

### 4.2 Simulated samples

Number of physics processes related to this analysis are simulated using generators, which simulates the final state particles of given physics processes according to certain theoretical models. They are often called “MC samples” as it uses Monte Carlo (MC) technique in generating events. These samples are used for several purposes, e.g. estimating the signal acceptance, the contributions of the background events and systematics errors. Events in MC samples are generated according to theoretical probability distributions of observables in physics processes. In theoretical calculations, the models of hard collisions use perturbative QCD calculation at a finite order of  $\alpha_s$ , which is called Matrix Element (ME) part. The generated a few partons subsequently are fragmented into more number of partons by Parton Shower (PS) algorithm. The many partons are finally hadronized into many hadrons using phenomenological models. The general structure of a simulated event is illustrated in Fig. 4.4. These events subsequently undergo the detector simulation with

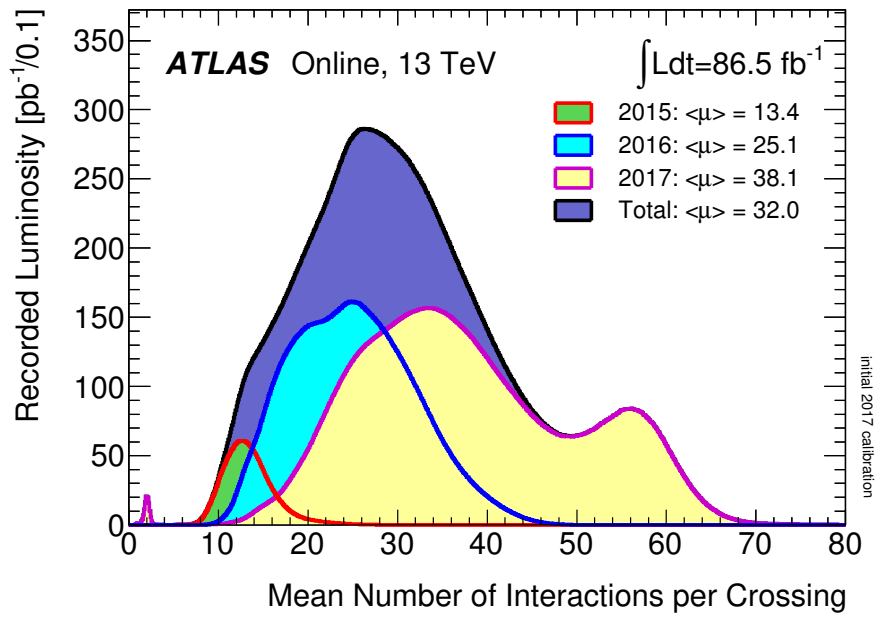


Figure 4.1: Number of Interactions per Crossing (Pile-up) [26]

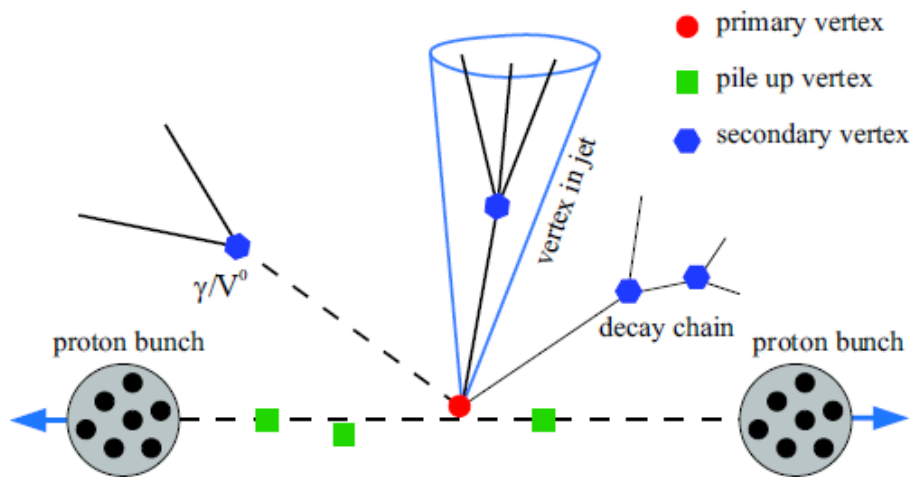


Figure 4.2: A sketch of pile-up [27]

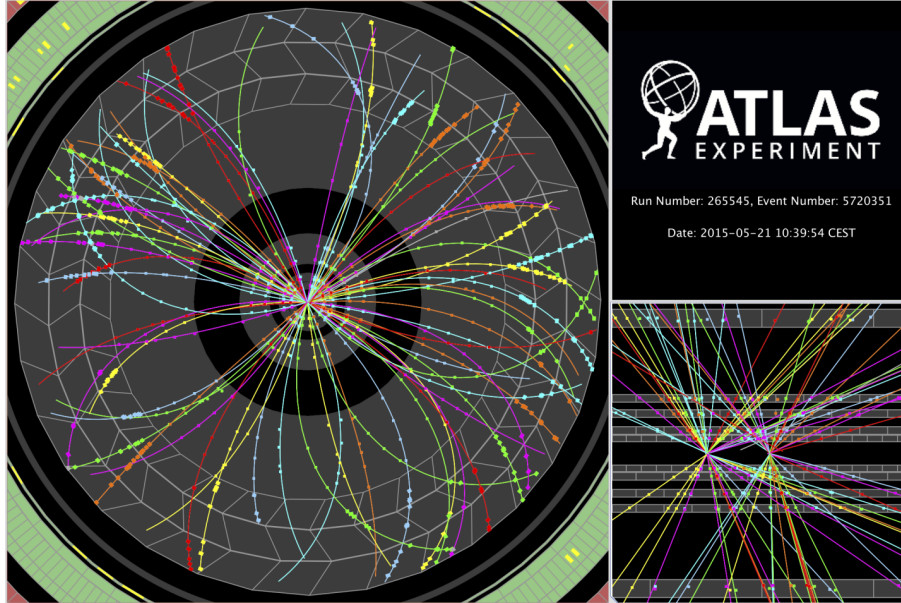


Figure 4.3: Pile-up eventdisplay: there are 2 pile-ups [28].

GEANT4 [29].

#### 4.2.1 Matrix Element calculation

**POWHEG** POWHEG [31] is an NLO ME generator to generate the hard emission with positive event weights. It can be interfaced to PYTHIA, HERWIG for parton showering and hadronization.

**aMC@NLO** aMC@NLO [32] is another next-to-leading order ME generator. In this analysis, it is used in combination with PYTHIA for parton shower and hadronization.

#### 4.2.2 Parton shower and hadronization models

**PYTHIA** PYTHIA [33] is a general purpose MC event generator. It can be used as standalone generator. In this analysis, it is used in combination with other ME generators for simulation of various samples and takes care of the parton shower and hadronization part. In PYTHIA, the parton shower is  $p_T$ -ordered. The hadronization is based on the string fragmentation model.

**HERWIG** HERWIG [34] is another general purpose MC event generator. In this analysis, it is used in combination with the POWHEG ME generator. It is based on angular-ordered parton shower. The hadronization part is based on the cluster model.

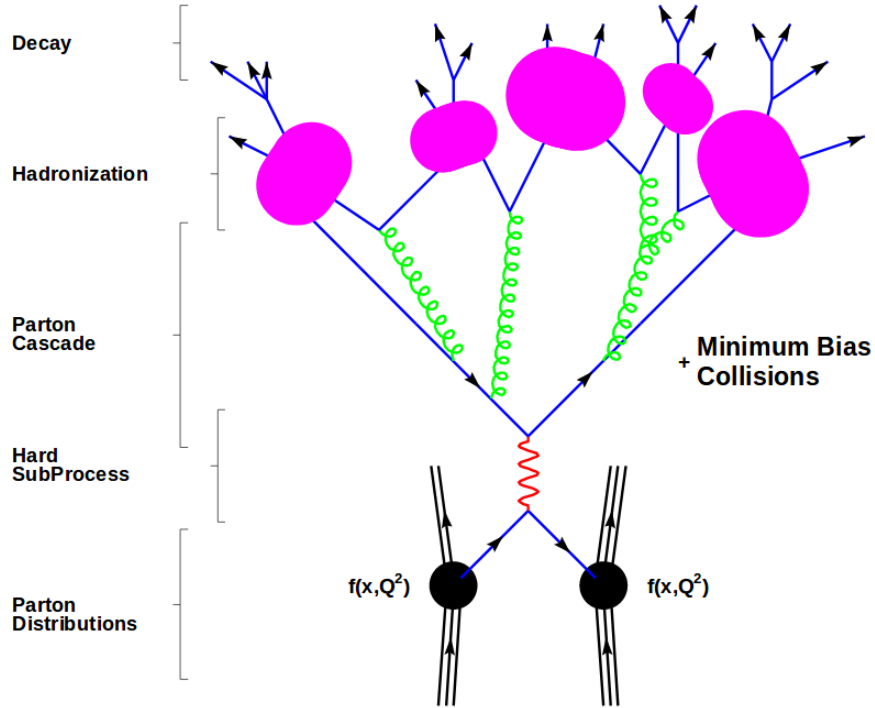


Figure 4.4: A conceptual drawing of a showering and hadronization in a generated event [30]

**SHERPA** SHERPA [35] is a multi-purpose MC event generator. It is largely developed independently of the other general purpose MC event generators, PYTHIA and HERWIG. It also can generate multi-parton processes with LO calculation and can treat the parton shower and hadronization processes. Its parton shower and hadronization processes is based on PYTHIA, but not all of PYTHIA.

### 4.2.3 Signal and background samples

The MC samples relevant to  $t\bar{t}$  cross section measurement are listed in Table 4.1, including  $t\bar{t}$  signal samples and various backgrounds. A top-quark mass of  $m_t = 172.5$  GeV is assumed when generating samples. The  $t\bar{t}$  samples are normalised to total cross section obtained from the next-to-next-to-leading order calculation with next-to-next-to-leading log corrections (NNLO+NNLL):  $\sigma_{t\bar{t}} = 832_{-51}^{+46}$  pb.

The background samples represent different physics processes, which have similar decay products as the  $t\bar{t}$  signal and therefore can also pass the  $t\bar{t}$  selection criteria. The descriptions of the background sources and their estimation is presented in Chapter 6.

Monte Carlo Generator	PDF	$\sigma$ (pb)	Comment
<b><i>tt</i> Signal samples</b>			
POWHEG+PYTHIA8	A14 NNPDF23LO	832	<i>tt</i> all-hadronic
POWHEG+PYTHIA8	A14 NNPDF23LO	832	Increased ISR/FSR <i>tt</i> all-hadronic
POWHEG+PYTHIA8	A14 NNPDF23LO	832	Decreased ISR/IFSR <i>tt</i> all-hadronic
POWHEG+HERWIG7	H7UE NNPDF23LO	832	<i>tt</i> all-hadronic alternative shower and hadronization model
aMC@NLO+PYTHIA8	A14 NNPDF23LO	832	<i>tt</i> all-hadronic alternative matrix element model
SHERPA	NNPDF3.0 NNLO	832	<i>tt</i> all-hadronic model used in final comparison only
<b>Background samples</b>			
POWHEG+PYTHIA8	A14 NNPDF23LO	832	<i>tt</i> non-hadronic
POWHEG+PYTHIA6	CT10 and Perugia2012	72	<i>Wt</i> inclusive single top
POWHEG+PYTHIA6	CT10 and Perugia2012	72	<i>Wt</i> inclusive single anti-top
MCatNLO+PYTHIA8	A14 NNPDF23LO	0.603	<i>ttW</i> inclusive sample
MCatNLO+PYTHIA8	A14 NNPDF23LO	0.586	<i>ttZ</i> sample with <i>Z</i> decaying to <i>qq</i>
MCatNLO+PYTHIA8	A14 NNPDF23LO	0.508	<i>ttH</i> dileptonic sample
MCatNLO+PYTHIA8	A14 NNPDF23LO	0.508	<i>ttH</i> semileptonic sample
MCatNLO+PYTHIA8	A14 NNPDF23LO	0.508	<i>ttH</i> all hadronic sample

Table 4.1: MC samples list.  $t\bar{t}$  signal samples is used to predict the  $t\bar{t}$  signal events and assess the modelling uncertainties. POWHEG+PYTHIA8 is nominal sample, while generating the more or less ISR/FSR samples by change its parameters related to radiation.  $\sigma$  indicates the cross section of these samples predicted by Standard Model. Background samples are used to predict the background events.

# Chapter 5

## The reconstruction of physics objects in ATLAS

The particles from the proton collisions are reconstructed with dedicated algorithms by using the information from the ATLAS sub-detectors. The reconstructed elements such as electron, muon and jet, are called physics object. For this analysis of  $t\bar{t}$  all-hadronic decay channel, the main physics objects are jets. The details on jet reconstruction and how to tag the jets originated from a  $b$ -quark or a top quark are described in next sub-sections.

### 5.1 Jet reconstruction

In this analysis, the jet reconstruction uses the anti- $k_t$  algorithm [36]. The principle of this algorithm is that among clusters within a certain distance  $R$ , the cluster with the largest transverse-momentum-weighted distance  $d_{ij}$  in an event are merged.

More in detail, the procedure has the following steps. Firstly, the algorithm calculates the  $d_{ij}$  for all the combinations of  $i$ -th and  $j$ -th clusters. The  $d_{ij}$  is defined as

$$\begin{aligned}d_{ij} &= \min(k_{t_i}^{-2}, k_{t_j}^{-2}) \frac{\Delta R_{ij}}{R}, \\d_{ii} &= k_{t_i}^{-2}, \\ \Delta R_{ij} &= \sqrt{\Delta \eta_{ij}^2 + \Delta \phi_{ij}^2},\end{aligned}\tag{5.1}$$

where  $k_i$  is the transverse momentum of the  $i$ -th cluster.  $R$  is distance parameter, which reflects the size of a jet; both  $R = 0.4$  and  $1.0$  are used in this analysis.  $\Delta R_{ij}$  is the distance between the  $i$ -th and  $j$ -th cluster in the  $y - \phi$  plane. If  $d_{ij}$  is the minimum value among the combinations, the  $i$ -th and  $j$ -th clusters are considered to be merged into a new cluster. If  $d_{ii}$  is the minimum, the  $i$ -th cluster are considered as a reconstructed jet, to be removed from the cluster list and added to the list of jet candidates. This algorithm repeats the process until no cluster is left.

This algorithm is used for jet finding in the detector level as well as in the particle level. In the detector level, the jet reconstruction starts with finding a cluster of

significant energy deposit in the calorimeters. The cluster is formed by the ‘three-dimensional TopoCluster’ algorithm [37]. These clusters are used as the input to the jet reconstruction algorithm. In the particle level, the jet reconstruction is performed from final state particles.

It is necessary to calibrate the jet energy after the reconstruction of these jets because the observed energy in the calorimeter does not represent the original energy from the parton (a quark or gluon) due to the undetected particles, such as part of neutron and neutrino etc, the initial and final state radiation, and imperfect calorimeter response. Jet energy is calibrated to the hadronic energy scale which is called JES (Jet energy scale), which is derived as a simple correction relating the calorimeter’s response to the true jet energy using MC simulations. In this analysis, the energy of the reconstructed jet is calibrated using MC simulations and *in – situ* techniques [38].

### 5.1.1 *b*-tagging

The ability to identify the flavour of a reconstructed jet as the *b*-quark jet from *c*-quark, gluon and other light quarks, is provided by exploiting the characteristics of *b*-hadrons. The *b*-hadron with long lifetime ( $c\tau \sim 420 \mu\text{m}$ ) tends to decay after travelling a few millimeters from the interaction point. This identification of *b*-quark jet is called “*b*-tagging”, where a jet is said to be a *b*-jet when an identified *b*-hadron with a transverse momentum of more than 5 GeV is found with  $\Delta R(b, jet) < 0.3$ . In this analysis, the reconstructed jet with anti- $k_t$   $R = 0.4$  is used for *b*-tagging. The identification of *b*-quark jets in ATLAS is based on combination from the following three basic *b*-tagging algorithms: IP3D, SV and JetFitter [39].

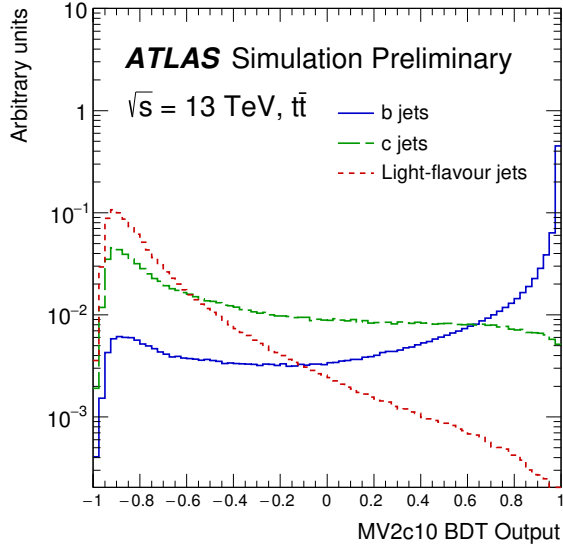
**IP3D: Impact Parameter based Algorithm** It uses the information from transverse and longitudinal impact parameters ( $d_0$  and  $z_0$ ), as introduced in Section 3.2.2, of all the tracks associated to the jet.

**SV: Secondary Vertex Finding Algorithm** The SV algorithm uses the information from secondary vertex formed by the decay products of a *b*-hadron within the jet as illustrated in Fig. 5.1(a).

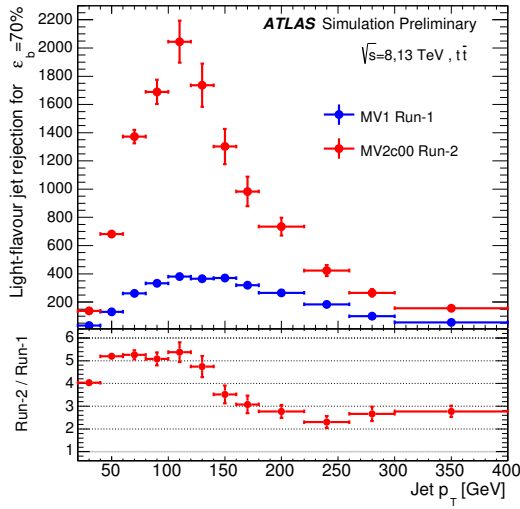
**JetFitter: Decay Chain Multi-Vortex Algorithm** The JetFitter exploits the topology of *b* and *c* hadron decay chain inside the jet. This algorithm uses Kalman Filter to find a common line on primary vertex  $\rightarrow b \rightarrow c$ -hadron as shown in Fig. 5.1(b).

To achieve a better discrimination, a Boosted Decision Tree (BDT) algorithm, one of the ROOT Toolkit for Multivariate Data Analysis (TMVA) [40], is a multivariate analysis technique that simultaneously evaluates several properties of a physics object when making a selection decision. The BDT algorithm uses the information from IP3D, SV and JetFitter algorithms to discriminate the flavour of a

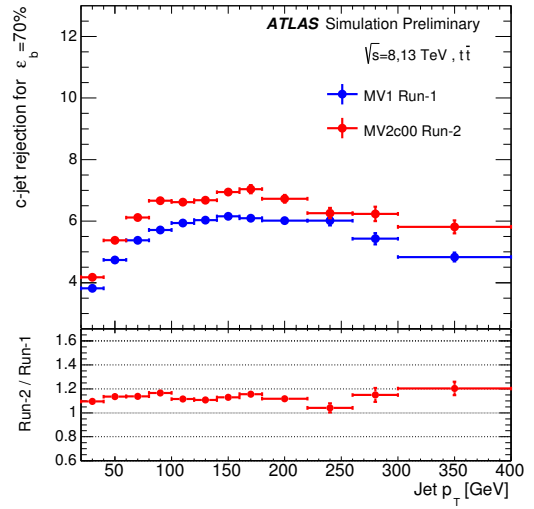




(a)

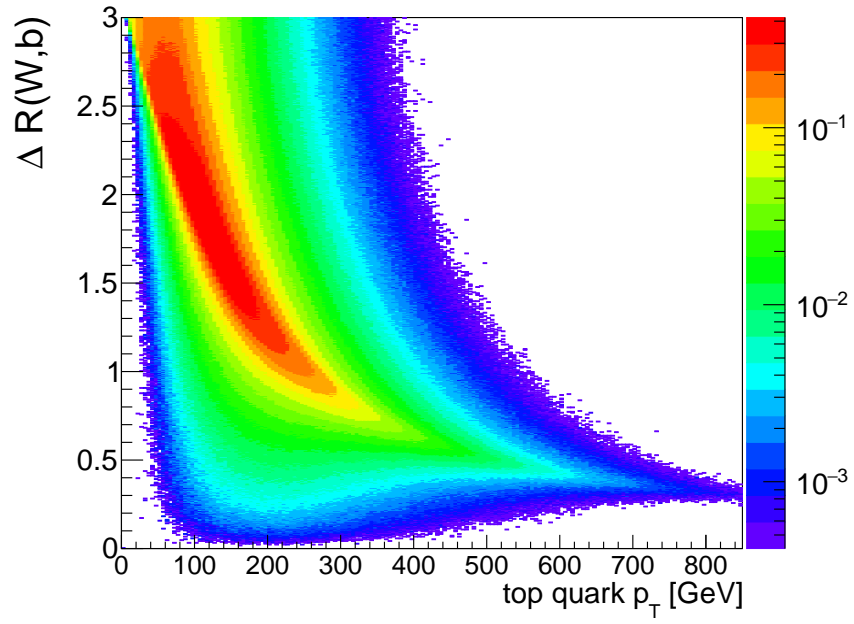


(b)

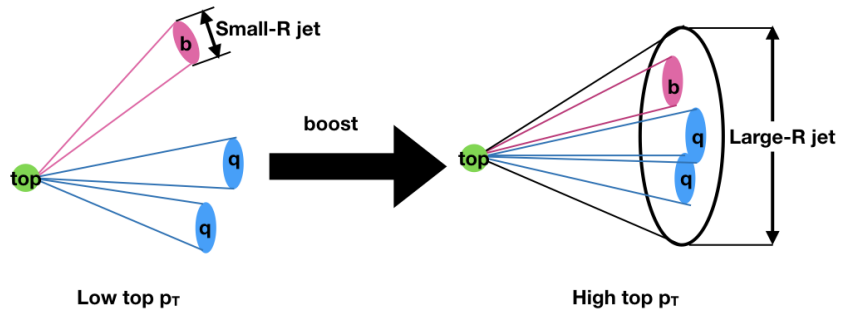


(c)

Figure 5.2: (a) Discrimination with BDT for  $b$ -tagging; (b) and (c) the  $c$ -jet or light-quark jets rejection with fixed  $b$ -tagging efficiency 70% in each  $p_T$  bin[41, 42]



(a)



(b)

Figure 5.3: (a): Distance  $\Delta R$  between  $W$ -boson and  $b$ -quark in  $\eta$ - $\phi$  space as a function of top-quark  $p_T$ ; (b) illustration of a top quark observed as a boosted jet with Large-R.

often much softer than hard-scattering partons products. The trimming procedure uses  $k_t$  algorithm with a smaller cone radius ( $R = 0.2$ ) reconstruct smaller sub-jets from the Large-R jet constituents, putting on them the constraint  $p_T^i/p_T^{\text{jet}} < f_{\text{cut}}$ , where  $p_T^i$  is the transverse momentum of the  $i$ -th sub jet ( $R_{\text{sub}} = 0.2$ ), and the  $f_{\text{cut}}$  was chosen as 0.05 [43]. The procedure is illustrated in Figure 5.4.

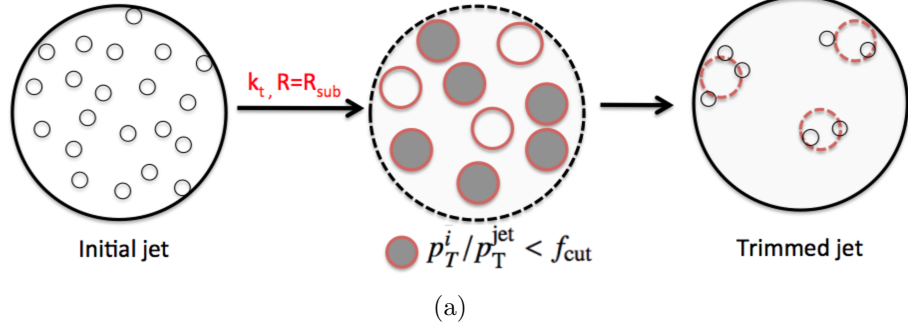


Figure 5.4: Diagram depicting the jet trimming procedure [43].

#### Observables for top tagging

Two observables are used for top tagging, jet mass and N-Subjettiness.

- **Jet Mass** Jet Mass is calculated from the energies and momentum of the constituents of the Large-R jet as given in the equation

$$m_{\text{jet}} = \sqrt{\left(\sum_i E_i\right)^2 - \sum_i p_i^2} \quad (5.2)$$

where  $E_i$  and  $p_i$  are the energy and momentum of the  $i$ -th constituent, respectively. An example for the distribution of the Large-R jet mass in signal and background with low and high Large-R jet  $p_T$  is shown in Fig. 5.5. The peak around 170 GeV for the mass spectrum of the  $t\bar{t}$  signal indicates the top mass and the peak around 80 GeV indicates the  $W$ -boson mass. The mass peak of the background coming from light jets distributes in the low value with clear discrimination with the high mass peak of the top quark.

- **N-Subjettiness** N-Subjettiness variable  $\tau_N$  is an observable related to the sub-jet multiplicity. The  $\tau_N$  variable is calculated by clustering the constituents of the jet requiring exactly N sub-jets to be found with the following definition.

$$\tau_N = \frac{1}{d_0} \sum_k p_{T_k} \times \min(\delta R_{1k}, \delta R_{2k}, \delta R_{3k}, \dots, \delta R_{Nk}), \quad (5.3)$$

$$d_0 = \sum_k p_{T_k} \times R$$

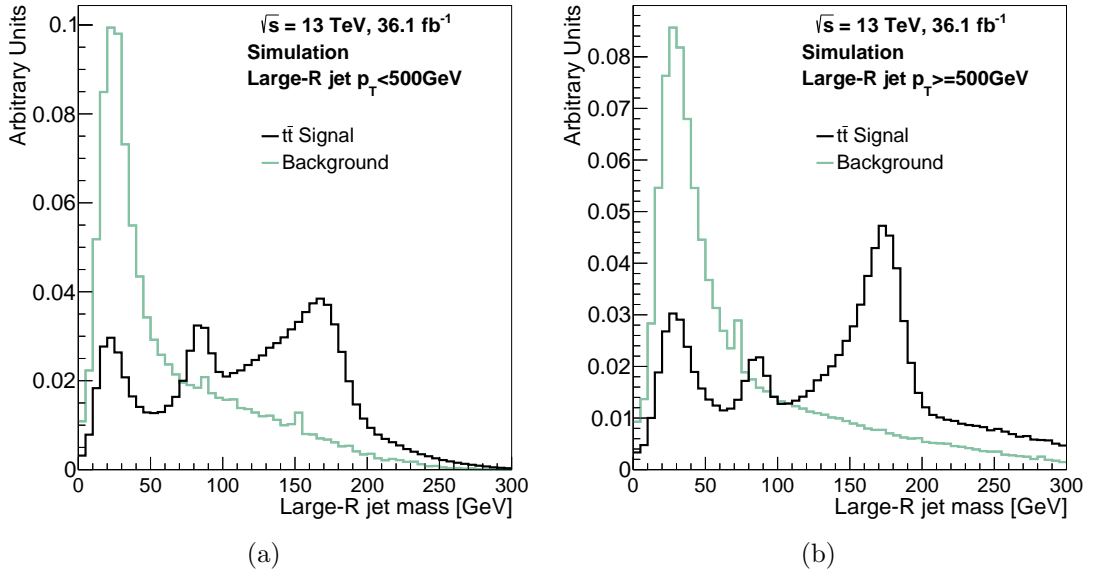


Figure 5.5: Distribution of mass for Large-R jet. The distribution of  $t\bar{t}$  and Background histograms are normalized to unity respectively.

where  $R$  is the Large-R jet radius parameter,  $p_{T_k}$  is the  $p_T$  of the  $k$ -th constituent and  $\delta R_{ik}$  is the distance between the  $i$ -th sub-jet to  $k$ -th constituent. The value of  $\tau_N$  is large when the jet is composed of  $N+1$  object, the corresponding value  $\tau_{N+1}$  is small. In order to discriminate a Large-R jet derived from a boosted top quark with respect to one originated by the parton shower of a light quark or a gluon, the Large-R jet comes from top with the ratio of  $\tau_{32} = \frac{\tau_3}{\tau_2}$ . The  $\tau_{32} \cong 1$  corresponds to the Large-R jet that is very well described by two subjets, whereas a lower value implies the Large-R jet that is much better described by three subjets than two. An example for the distribution of  $\tau_{32}$  in signal and background with low and high Large-R jet  $p_T$  is shown in Fig. 5.6.

The top tagging is performed by applying cuts on Large-R jet mass and  $\tau_{32}$ . Since the two variables distributions are different in different Large-R jets  $p_T$  region, the optimal cuts as a function of  $p_T$  are shown in Fig. 5.7. The Large-R jet, passing the two variables cut is considered the as top candidate, while cuts are varied as a function of  $p_T$  to obtain a flat 50% efficiency and maximum multi-jet rejection over the relevant  $p_T$  range. The top tagging efficiency and background rejection as a function of jet  $p_T$  are shown in Fig. 5.8.

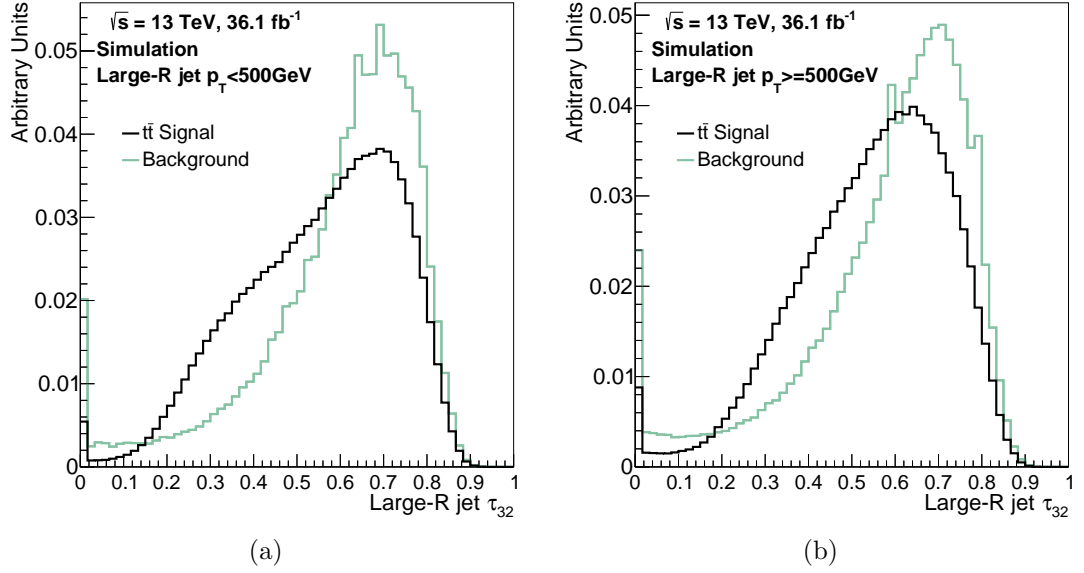


Figure 5.6: Distribution of  $\tau_{32}$  for Large-R jet. The distribution of  $t\bar{t}$  and Background histograms are normalized to unity respectively.

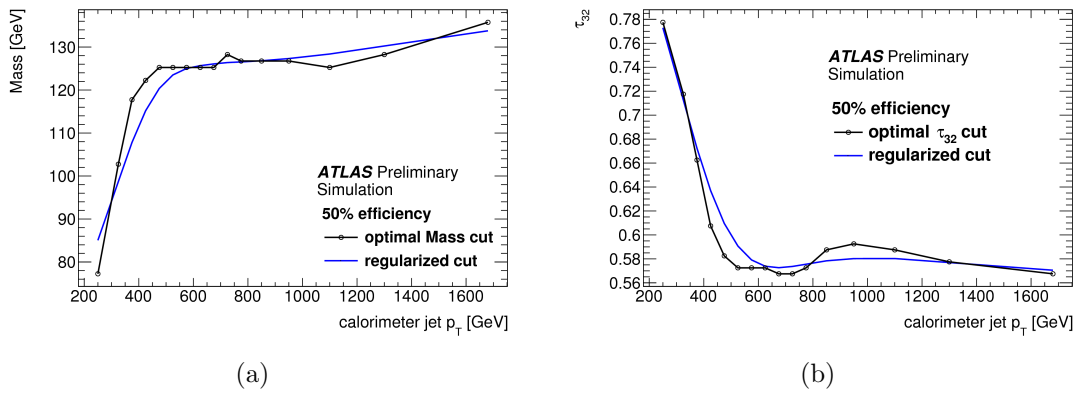


Figure 5.7: Values of the selection requirements in the top-tagging algorithm: (a) the lower threshold on Large-R jet mass and (b)  $\tau_{32}$  for the 50% working point [44].

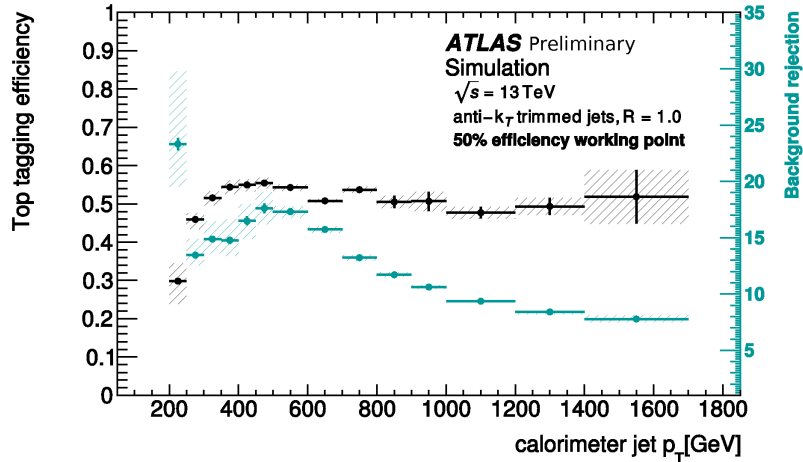


Figure 5.8: Top tagging efficiency and background rejection for Large-R jet [44].

## 5.2 Lepton reconstruction

In order to reject top quark events where a top quark with leptonic decay results in a lepton produced in the final state, the events are required to contain no reconstructed electron or muon candidate.

**Electron reconstruction** Electron candidates are identified as objects with a high quality inner detector track matched to calorimeter deposits consistent with an electromagnetic shower [45]. A likelihood-based requirement is used to reject fake candidates. The isolation with the combination of calorimeter- and track-based isolation requirements are imposed so that electron identification efficiencies is  $\sim 90\%$  for electrons with  $p_T > 25$  GeV and  $96\%$  for electrons with  $p_T > 60$  GeV. The calorimeter deposits have to form a cluster with transverse energy  $E_T > 25$  GeV,  $|\eta| < 2.47$  and be outside the transition region  $1.37 \leq |\eta| \leq 1.52$  between the barrel and endcap calorimeters.

**Muon reconstruction** Muon candidates are reconstructed using the combination of high quality inner detector tracks and tracks reconstructed in the muon spectrometer [46]. Only muon candidates with  $p_T > 25$  GeV and  $|\eta| < 2.5$  are considered. The isolation similar to those used for electrons are used.

# Chapter 6

## Event selection and Background estimation

This chapter describes the event selection of this analysis in Section 6.1 and the estimation of background in Section 6.2. Then, the distributions for detector level are presented.

### 6.1 Event selection

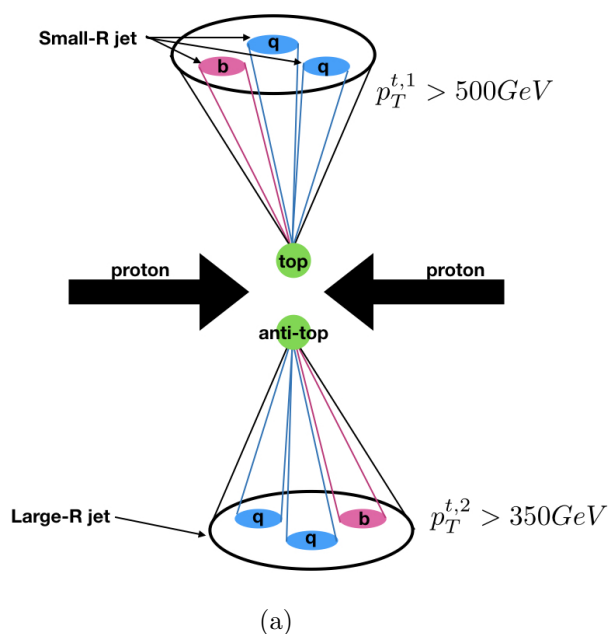


Figure 6.1: Two Large-R jets from  $t\bar{t}$  production in a  $pp$  collision.

The event selection is designed to enhance the purity of the  $t\bar{t}$  candidates (signal) while minimizing background contamination. Since the decay products from the boosted top quark are observed as a Large-R jet for high- $p_T$  top quarks, at least

two Large-R jets are required in the events as illustrated in Fig. 6.1. The angular separation between two-body decay products from a heavy particle can be given by:

$$\Delta R \sim \frac{2m}{p_T}, \quad (6.1)$$

where  $m$  and  $p_T$  are the mass and transverse momentum of the heavy particle. Taking  $\Delta R = 1.0$  and  $m_{\text{top}} = 173 \text{ GeV}$  into above formula, the  $p_T$  is about 346 GeV. In this analysis, the transverse momentum  $p_T$  of the two Large-R jets is required above 350 GeV for each event.

The applied cuts for event selection in detail are the following:

- (1) Hadronic trigger for Large-R jet: where Large-R with  $R = 1.0$  and Small-R with  $R = 0.4$  are used. The used trigger chains are HLT\_j360\_a10r\_L1J100 for 2015 and HLT\_j420\_a10r\_L1J100 for 2016, where L1J100 denotes 100 GeV for threshold of Level 1 trigger and j360 denotes 360 GeV for threshold of HLT trigger in HLT\_j360\_a10r\_L1J100.
- (2) Kinematic requirement on Large-R jet: the largest  $p_T$  Large-R jet is called Leading Large-R jet. For selecting the Leading Large-R jet,  $p_T > 500 \text{ GeV}$  and  $|\eta| < 2.0$  are required in order to keep the trigger efficiency 100% as shown in Fig. 6.2. This jet is considered as a top candidate and therefore denoted as  $p_T^{t,1}$ . The 2nd Leading Large jet requires  $p_T^{t,2} > 350 \text{ GeV}$  and  $|\eta| < 2.0$ .
- (3) To reduce the pile-up effect, a primary vertex includes five or more associated tracks with  $p_T > 0.4 \text{ GeV}$ . Pile-up events mainly consist of soft  $pp$  collisions, which produce only small number of high  $p_T$  tracks.
- (4) No isolated lepton in the final state to reduce the events from top leptonic decay and other process with a high- $p_T$  lepton in the final state. The requirements for Muons:  $p_T > 25 \text{ GeV}$  and  $|\eta| < 2.5$ , for electrons:  $p_T > 25 \text{ GeV}$  and  $|\eta| < 2.47$ .
- (5) Large-R jet mass cut around top mass:  $|m_{J1} - m_{\text{top}}| < 50 \text{ GeV}$  and  $|m_{J2} - m_{\text{top}}| < 50 \text{ GeV}$ , where J1 denotes Leading Large-R jet and J2 denotes 2nd Leading Large-R jet.
- (6) For selecting  $b$ -jets: at least two Small-R jets,  $p_T > 25 \text{ GeV}$ ,  $|\eta| < 2.5$  are in the final state of the event. For each selected Small-R jet, the MVA cut  $> 0.8244$  as described in Section 5.1.1. This is to keep  $b$ -tagging efficiency of around 70%.
- (7) Large-R  $b$ -tagging:  $\Delta R(J, b) < 1.0$ , where  $J$  denotes the Large-R jets and  $b$  is the  $b$ -tagged Small-R jet as defined in 5, to require that the  $b$ -tagged Small-R jet is matched to the Large-R jet.
- (8) For selecting a Large-R jet as a top candidate: passing the top-tagging condition described in Section 5.1.2.

Signal region: Leading Large- $R$  jet and 2nd Leading Large- $R$  jet both pass the condition (1 $\sim$ 5 and 8). The Leading and 2nd Leading Large- $R$  jet both contain at least a Small- $R$  jet tagged by  $b$ -tagging (condition: 1 $\sim$ 7), which indicates the Large- $R$  jet has a  $b$ -jet inside. It is labeled with “S” in the following table.

The green regions (e.g. A, B etc.), called “control regions”, are used to estimate the multijet background. The blue regions (e.g. L, N etc.), called “validation region”, are used to validate the estimation method of multijet background.

2nd Large- $R$ jet	1t1b	J	K	L	S
	0t1b	B	D	H	N
	1t0b	E	F	G	M
	0t0b	A	C	I	O
		0t0b	1t0b	0t1b	1t1b
	Leading large- $R$ jet				

Table 6.1: Definition of the signal (red), control region (green) and validation region (blue). A top-quark tagged jet is denoted “1t” in the table, while a jet that is not top-tagged is labeled “0t”. The labels “1b” and “0b” represent large- $R$  jets that are  $b$ -tagged and not  $b$ -tagged, respectively.

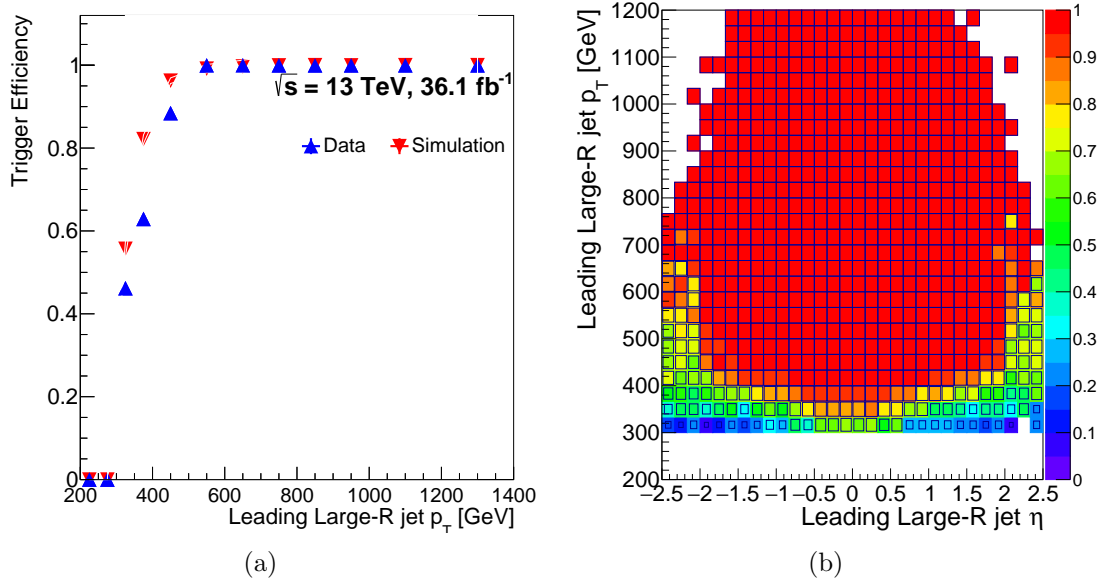


Figure 6.2: (a) Trigger efficiency v.s.  $p_T$ ; (b) trigger efficiency map between  $\eta$  and  $p_T$  of Leading Large- $R$  jet.

After these event selections, the Leading Large- $R$  jet mass distribution shows the mass peak around top mass (172.5 GeV) as shown in Fig. 6.3. Other kinematical distributions are shown after estimating background.

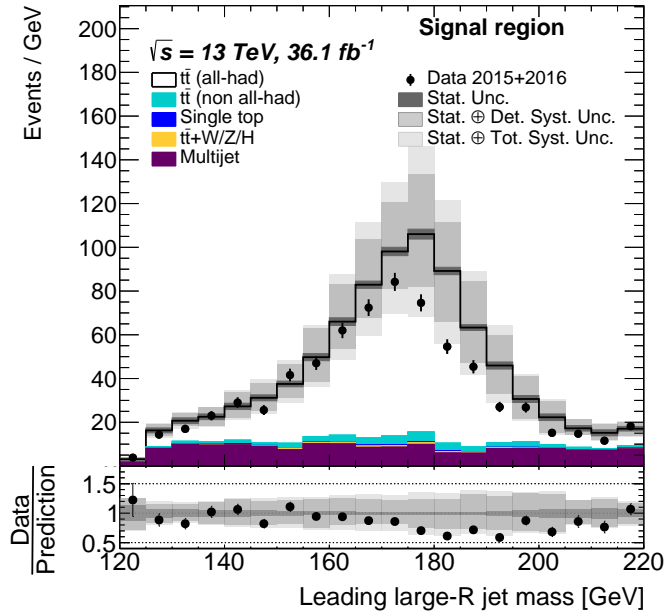


Figure 6.3: Mass distribution for Leading Large-R jet after selection in signal region.

## 6.2 Background sources

There are two kinds of background sources: those involving one or more top quarks in the final state and those sources where no top quarks is involved. The former backgrounds is estimated using MC simulations. The latter background is the largest background source. It is event where the two Leading Large-R jets both come from gluons,  $u$ ,  $d$ ,  $s$ ,  $c$ -quarks or  $b$  quarks (called ‘multijet’ or ‘QCD’). To avoid large uncertainties using MC predictions, the multijet background is determined using data-driven technique.

The event yields are shown in Table 6.2 for data, simulated signal, and backgrounds. The data-driven method for multijet background determination is described below.

$t\bar{t}$ (all-hadronic)	3250	$\pm$	470
$t\bar{t}$ (non-all-hadronic)	200	$\pm$	40
Single top-quark	24	$\pm$	12
$t\bar{t}+W/Z/H$	33	$\pm$	10
Multijet events	810	$\pm$	50
Prediction	4320	$\pm$	530
Data ( $36.1fb^{-1}$ )	3541		

Table 6.2: Event yields in the signal region for the expected  $t\bar{t}$  signal process and the background processes. The uncertainties represent the sum in quadrature of the statistical and systematic uncertainties in each sub-process.

### 6.2.1 Data-driven QCD background estimation

The method used in this analysis is based on a study in a previous work [47].

**Basic principle of the ABCD method** This estimation uses so-called ‘‘ABCD method’’. The general idea of the ABCD method is described below. First, the data samples are divided into four regions A, B, C and D, according to values of two indices for event selection criteria  $i$  and  $j$ , where  $i$  or  $j=0$  indicates the category of events failing the criteria  $i$  or  $j$ , and  $i$  or  $j=1$  is the category of events passing the criteria  $i$  or  $j$ . The distribution of variable  $x$  ( $p_T$  etc.) from background sources in region D (signal region) is estimated from known data distributions in regions A, B and C, which are dominated by background sources. There is an assumption to estimate the background distribution in signal region (D), namely parameters  $i, j$  are statistically independent variables. The total number of events in region D can then be estimated by the formula

$$D = \frac{B}{A} \times C \quad (6.2)$$

where A, B, C and D denote the number of events in region A, B, C and D, respectively.

selection	$j$ failed	$j$ passed
$i$ failed	A	B
$i$ passed	C	D

Table 6.3: Four regions classified according to properties  $i$  and  $j$

This method can be used for an estimation of a differential distribution of the variable  $x$  in region D. By applying the Eq. 6.2 bin-by-bin, the differential distribution in signal region D for  $k$ -th bin is estimated using

$$D_k = \frac{B_k}{A_k} C_k. \quad (6.3)$$

**Extended ABCD method** In this analysis, the signal, validation regions as defined in Table 6.4 is used for applying the ABCD method. It is called ‘Extended ABCD method’. This method is to reduce the bias in background estimation due to possible correlation of the rate of between b-tagging and top-tagging. A refined data-driven estimate of the size of the multijet background in the signal region (S)

given by

$$S = \frac{J \times O}{A} \cdot k_{t_1, b_2} \cdot k_{t_2, b_1} \cdot k_{t_1, t_2} \cdot k_{b_1, b_2} \quad (6.4)$$

$$\begin{aligned} &= \frac{J \times O}{A} \cdot \frac{D \times A}{B \times C} \cdot \frac{G \times A}{E \times I} \cdot \frac{F \times A}{E \times C} \cdot \frac{H \times A}{B \times I} \\ &= \frac{J \times O \times H \times F \times D \times G \times A^3}{(B \times E \times C \times I)^2}, \end{aligned} \quad (6.5)$$

where the region names (A-O and S): the number of observed events in that region,  $J \times O/A$  is from basic ABCD method. The factor  $k$ , e.g.  $k_{t_1, b_2}$  is equal to unity if  $t_1$  and  $b_2$  are independent. The factor  $k_{t_1, b_2}$  becomes larger than unity when the two tagging method  $t_1$  and  $b_2$  are positively correlated, and below unity when negatively correlated. If  $k_{t_1, b_2} > 1.0$ , the amount of the background in S (signal region) is likely underestimated by the standard ABCD method  $S = (J \times O)/A$ . The factor  $k_{t_1, b_2}$  compensates such possible correlation effect.

2nd Large- $R$ jet	1t1b	J (7.6%)	K (21%)	L (42%)	S
	0t1b	B (2.2%)	D (5.8%)	H (13%)	N (47%)
	1t0b	E (0.7%)	F (2.4%)	G (6.4%)	M (30%)
	0t0b	A (0.23%)	C (0.76%)	I (2.2%)	O (11%)
		0t0b	1t0b	0t1b	1t1b
Leading large- $R$ jet					

Table 6.4: Region labels and expected proportion of  $t\bar{t}$  events used for the data-driven background prediction of multijet events.

Regions L and N are expected to contain large levels of background than in the signal region, with approximately the same numbers of  $t\bar{t}$  signal events and multijet background events. They are used as validation regions to verify that the signal and background estimates are robust. The data distributions in validation regions and signal region are compared to the sum of the prediction of models and the estimated multijet background. The input for the extended ABCD method is obtained by using the following formula. Then the multijet background in the signal region is estimated by Eq. 6.5.

$$N_{input} = N_{data} - N_{(background\ except\ multijet)} - N_{(t\bar{t}\ signal\ events)} \quad (6.6)$$

### Result of the estimation

- The non-resonant tails ( $m_{top} < 140$  GeV,  $m_{top} > 200$  GeV) in the validation region, as given in Fig. 6.4(b) and 6.4(c), are dominated by multijet background and well described by the estimated multijet background.
- The number of multijet events in the signal region is  $(810 \pm 50)$  with POWHEG+PYTHIA8 presented number of 3250 by the extended ABCD method, while

the number is 815 with the POWHEG+HERWIG7 signal predicted number of 2546. Within the statistical uncertainty, the two numbers for multijet are same despite different numbers of signal predicted.

- A difference between the observed and predicted numbers of events are observed in the signal region as seen in Fig. 6.4(a), but not found in validation as seen in Fig. 6.4(b) for POWHEG+PYTHIA8, while for POWHEG+HERWIG7, the difference is not observed in both validation and signal regions as seen in Fig. 6.4(c) and Fig. 6.4(d). This indicates the difference between the observed and predicted number of events does not come from multijet background estimation method, but from prediction of the  $t\bar{t}$  signal.
- A shift between the observed and predicted jet mass distributions is found in both validation and signal regions as shown in Fig. 6.4(b) and 6.4(a). The shift behaviour is consistent with the uncertainties from the calibration for Large-R jets. And the shape and event yield by POWHEG+HERWIG7 are closer to observed events than POWHEG+PYTHIA8 in signal region as shown in Fig. 6.4(a) and 6.4(d).

In the signal region with the nominal sample (POWHEG+PYTHIA8), the detector level of agreement between the observed and predicted distributions can be seen in kinematic distributions of the top candidates and  $t\bar{t}$  system as seen in Fig. 6.5 and 6.6. The prediction is generally in agreement with the data in shape. The distributions for the Leading and 2nd Leading Large-R jet  $p_T$  and rapidity in validation region N and L are also compared to the nominal sample (POWHEG+PYTHIA8) in Fig. 6.7. Additional distributions of detector level for other variables with POWHEG+HERWIG7 and POWHEG+PYTHIA8 are given in Appendix 11.3.1.

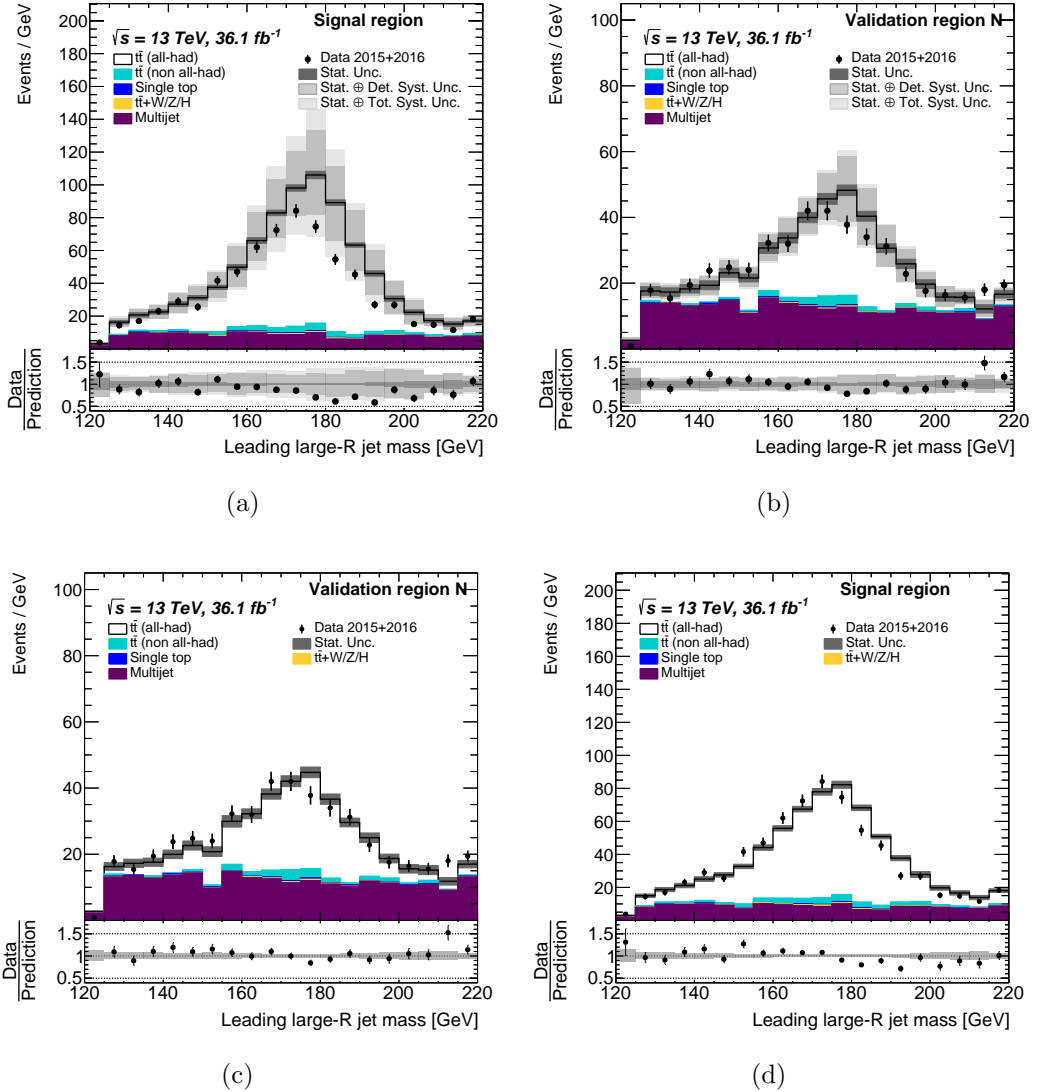
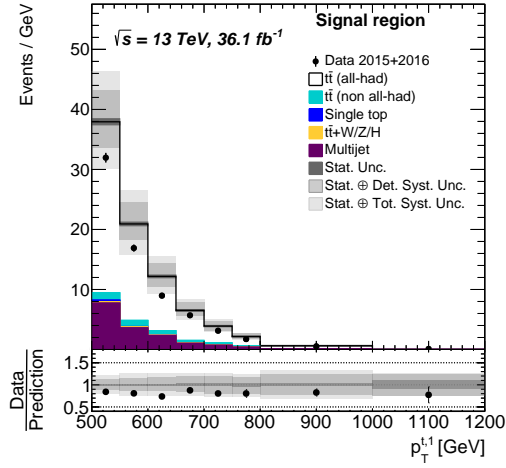
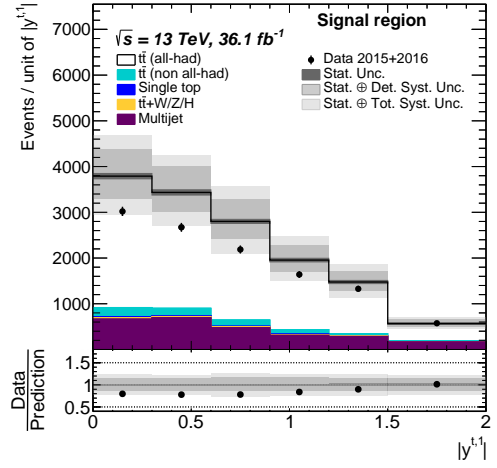


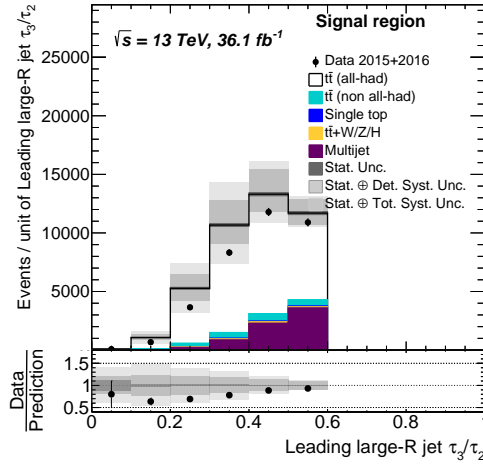
Figure 6.4: Kinematic distributions of top-quark candidate jets in the signal region S and in the validation regions N. The Leading Large-R jet mass distributions for the events in the signal region S and the validation region N are shown in (a) and (b), respectively. Top: POWHEG+PYTHIA8 Bottom: POWHEG+HERWIG7



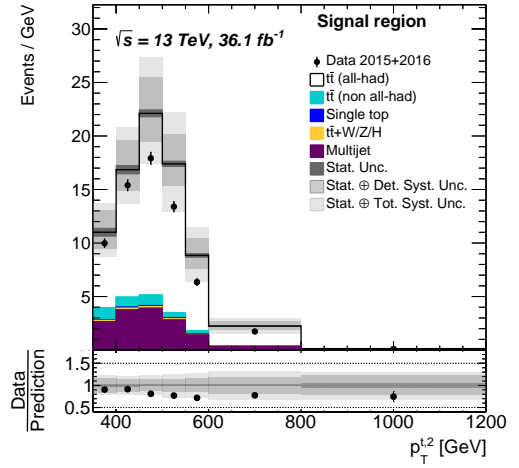
(a)



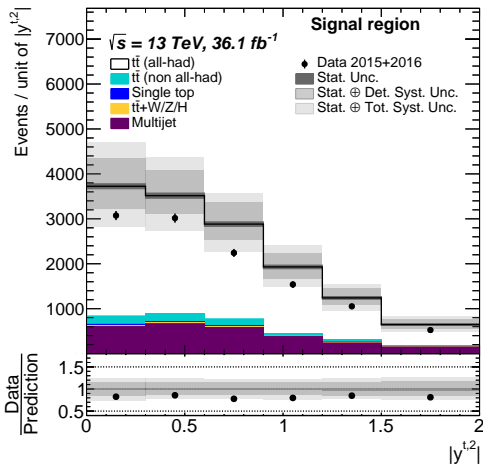
(b)



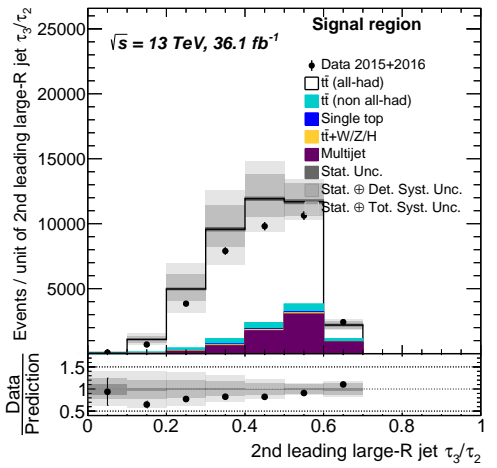
(c)



(d)



(e)



(f)

Figure 6.5: Kinematic distributions of top-quark candidate jets in the signal region S: (a) transverse momentum and (b) absolute value of the rapidity of the Leading top-quark jet and (c)  $\tau_{32}$ , (d) transverse momentum and (e) absolute value of the rapidity of the 2nd Leading top-quark jet and (f)  $\tau_{32}$ .

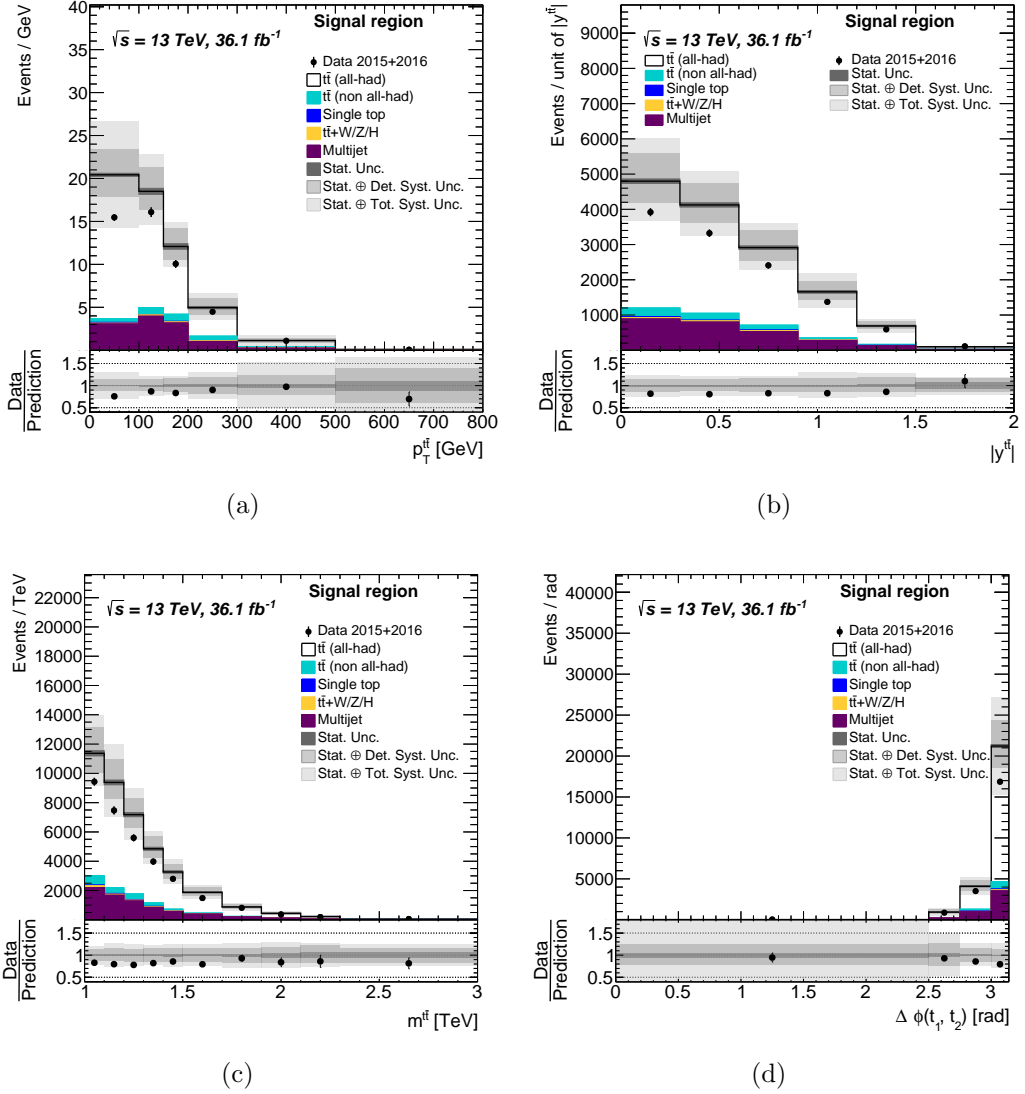


Figure 6.6: Kinematic distributions of top-quark candidate jets in the signal region S: (a) transverse momentum of the  $t\bar{t}$  system and (b) absolute value of the rapidity of the  $t\bar{t}$  system, (c) invariant mass of the  $t\bar{t}$  system and (d) azimuthal angle between the two top-quarks.

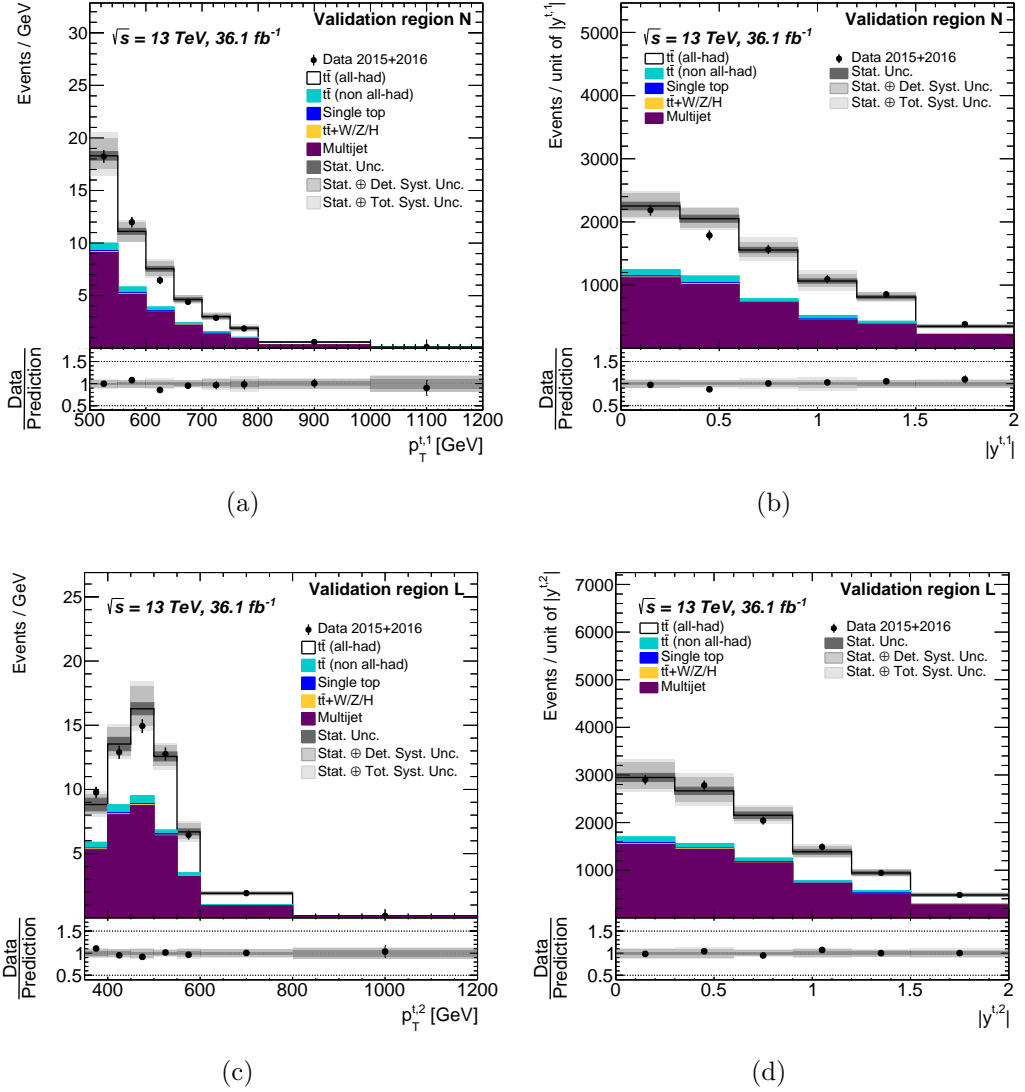


Figure 6.7: Kinematic distributions of top-quark candidate jets in the two validation regions  $N$  and  $L$ : (a) transverse momentum and (b) absolute value of the rapidity of the Leading large- $R$  jet, (c) transverse momentum and (d) absolute value of the rapidity of the 2nd Leading large- $R$  jet.

# Chapter 7

## Particle level fiducial phase-space cross sections

The differential cross sections are obtained from detector level distributions using an unfolding technique. This technique is to correct for detector effects such as efficiency, acceptance and resolution. The correction is made to the particle level using a restricted part of the phase space (fiducial phase-space), defined to be as close to the experimental acceptance and hence to avoid large extrapolation relying on modelling in generators.

### 7.1 Fiducial phase space

The particle-level fiducial phase-space definition models the kinematic requirements used to select the  $t\bar{t}$  processes. The following requirements on particle level objects in the all-hadronic  $t\bar{t}$  MC events are applied to define the particle-level fiducial phase-space:

- 1) no electrons or muons with  $p_T > 25$  GeV and  $|\eta| < 2.5$  being in the event,
- 2) 2nd Leading Large-R jet with  $p_T > 350$  GeV and  $|\eta| < 2.0$ ,
- 3) Leading Large-R jet with  $p_T > 500$  GeV and  $|\eta| < 2.0$ ,
- 4) the masses of the two Large-R jets be within 50 GeV of the top-quark mass of 172.5 GeV,
- 5) at least two Small-R jets with  $p_T > 25$  GeV and  $|\eta| < 2.5$ , and
- 6) the two Large-R jets both including at least a  $b$ -hadron inside the jet area.

In the process of top quark decaying into a  $W$  boson and a  $b$ -quark, virtual particles ( $E^2 - p^2 \neq m^2$ ) are sometimes generated. Usually, momentum, mass and position are used for the particle reconstruction. Correspondingly, the observables to be used for cross section definition should use properties of the final state particles,

which should be well defined in terms of quantum mechanics, i.e. the properties that have corresponding classical limit. The virtual state, therefore, can not be used for phase space definition. In particle level, the particles are real, conserving  $E^2 - p^2 = m^2$ . The reconstruction of top quarks is defined by using these real particles on the particle level. The Large-R jets are considered to be top-tagged if the conditions 4, 5 and 6 are fulfilled. The momenta of the Large-R jets are regarded as the top quark momenta.

Variables related to individual top quarks and related to the production of  $t\bar{t}$  are listed below.

- $p_T^{t,1}$  : Transverse momentum of Leading Large-R jet
- $|y^{t,1}|$  : Rapidity of the Leading Large-R jet
- $p_T^{t,2}$  : Transverse momentum of 2nd Leading Large-R jet
- $|y^{t,2}|$  : Rapidity of the 2nd Leading Large-R jet
- $p_T^{t\bar{t}}$  : Transverse momentum of the  $t\bar{t}$  system
- $m^{t\bar{t}}$  : Invariant mass of the  $t\bar{t}$  system.
- $|y^{t\bar{t}}|$  : Rapidity of the  $t\bar{t}$  system
- $\Delta\phi(t_1, t_2)$  : Azimuthal angle between the Leading and 2nd Leading Large-R jets.

Rapidity reflects the angular position of the particle production. Invariant mass is sensitive to the presence of a resonance state of the new particle.  $\Delta\phi(t_1, t_2)$  reflects the imbalance between the Leading and 2nd Leading Large-jets. In this analysis, differential cross sections as a function of these variables are measured.

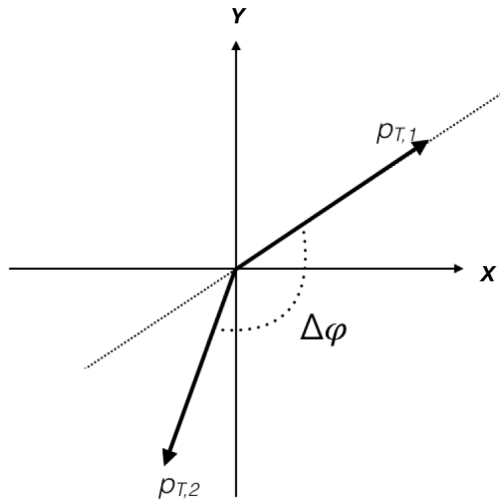


Figure 7.1: Diagram to illustrate the physical meaning of the variable  $\Delta\phi_{t\bar{t}}$ .

## 7.2 Unfolding procedure

Measurements of physical observables are usually distorted or biased by the limited resolution and acceptance of the detector, which prevents a direct comparison of the measured distributions with theoretical predictions. In order to make the comparison possible, the data must be corrected for these detector effects via a procedure called unfolding. To obtain a value for data on the particle level, the value of an observable on particle level is calculated by the following formula,

$$Y_{data}|_{\text{particle level}} = k (Y_{MC}|_{\text{particle level}}) \times \left( \frac{Y_{data}}{Y_{MC}} \Big|_{\text{detector level}} \right) \quad (7.1)$$

where generic factor  $k$  relates to many effects, such as detector efficiencies. Since bin-to-bin correlations are taken account in this study, each term of above formula is expressed by vectors and matrices, which is described later in this sub-section.

The unfolding starts from the detector level event distributions after subtraction of the estimated backgrounds. Since not all events in particle level can be reconstructed in detector level, The efficiency corrections  $\epsilon_{\text{eff}}$  (Eq. 7.2) correct for events that are in the fiducial phase space but are not reconstructed at the detector level.

$$\epsilon_{\text{eff}} = \frac{\text{events passing particle and detector level}}{\text{events passing particle level}} \quad (7.2)$$

Eq. 7.1 are modified to the following formula.

$$Y_{data}|_{\text{particle level}} = \frac{1}{\epsilon_{\text{eff}}} \times k' \times (Y_{MC}|_{\text{particle level}}) \times \left( \frac{Y_{data}}{Y_{MC}} \Big|_{\text{detector level}} \right), \quad k' = k \times \epsilon_{\text{eff}} \quad (7.3)$$

It is also the case that not all events passing the detector level are from the production of fiducial phase space. An acceptance correction  $f_{\text{acc}}$  is applied accounting for events, which are generated outside the fiducial phase space but pass the detector-level selection.

$$f_{\text{acc}} = \frac{\text{events passed particle and detector level}}{\text{events passed detector level}} \quad (7.4)$$

In a case like several bins in the distribution of detector level, the Eq.7.3 is modified to the following formula.

$$Y_{data}^i|_{\text{particle level}} = \frac{1}{\epsilon_{\text{eff}}^i} \times \sum_j k''^{(j)} \times \left( \frac{Y_{MC}^i|_{\text{particle level}}}{Y_{MC}^j|_{\text{detector level}}} \right) \times f_{\text{acc}}^j \times (Y_{data}^j|_{\text{detector level}}) \quad (7.5)$$

The term  $\left( \sum_j k''^{(j)} \times \left( \frac{Y_{MC}^i|_{\text{particle level}}}{Y_{MC}^j|_{\text{detector level}}} \right) \right)$  represents propagation of the generated particle-level distribution to the binned detector-level distribution. When the distribution of  $Y_{data}|_{\text{particle level}}$  has several bins, it is possible that the contents of a bin  $i$  on the particle level may propagate into a different bin on detector level. Migration matrix  $M_{ij}$  is defined as the conditional probability that a selected event, generated

in a bin  $i$  on the particle level, is reconstructed in a bin  $j$  on the detector level. It makes the sum of all bin in the detector from the propagation of  $i$ -th in the particle level 100% as the following formula.

$$\sum_j k''^{(j)} \times \left( \frac{Y_{MC}^i |_{\text{particle level}}}{Y_{MC}^j |_{\text{detector level}}} \right) \times M_{ij} = 1 \quad (7.6)$$

The term  $\left( k''^{(j)} \times \left( \frac{Y_{MC}^i |_{\text{particle level}}}{Y_{MC}^j |_{\text{detector level}}} \right) \right)$  is equal to the elements of the inverse of  $M_{ij}$ . The  $M_{ij}^{-1}$  is determined by the iterative Bayesian method [48]. Using the  $M_{ij}^{-1}$ , the Eq. 7.5 for  $i$ -th bin of distribution in fiducial phase space are modified to the following formula.

$$Y_{data}^i |_{\text{particle level}} = \frac{1}{\epsilon_{eff}^i} \times \sum_j M_{ij}^{-1} \times f_{acc}^j \times (Y_{data}^j |_{\text{detector level}}) \quad (7.7)$$

In order to correct the data to differential cross section, the luminosity and the bin width are taken into account and the value  $Y_{data}^j |_{\text{detector level}}$  is replaced the number of signal events, the  $t\bar{t}$  events  $(N_{\text{detector level}}^j - N_{\text{background}}^j)$ , where  $N_{\text{detector level}}$  and  $N_{\text{background}}$  refer to the number of reconstructed signal and background events, respectively. The index  $j$  runs over bins of  $X$  at the detector level while the index  $i$  labels the  $i$ -th bin at the particle level;  $\Delta X^i$  is the  $i$ -th bin width while  $\int \mathcal{L} dt$  is the integrated luminosity. The unfolding procedure for an observable  $X$  at particle level is summarized by the expression,

$$\frac{d\sigma^{\text{fid}}}{dX^i} \equiv \frac{1}{\int \mathcal{L} dt \cdot \Delta X^i} \cdot \frac{1}{\epsilon_{eff}^i} \cdot \sum_j M_{ij}^{-1} \cdot f_{acc}^j \cdot (N_{\text{detector level}}^j - N_{\text{background}}^j). \quad (7.8)$$

This contains a set of matching requirements. The matching requirements is that for an event to be considered well reconstructed the detector and particle level objects regarded as top-quarks must be angularly matched and have the same rank (first or second) when ordered by transverse momentum. The angular matching requires that each detector level top quark candidate is matched to a particle level top quark with  $\Delta R < 1.0$ . The angular matching is found to be fully efficient as shown in Fig. 7.2. On the other hand, it is observed that, for about 13% of events, the  $p_T$ -ordering of the two Leading jets at detector and particle level is inverted. The loss of the acceptance corrections as shown in Fig. 7.3 and 7.4 comes from the  $p_T$ -ordering effect. The efficiency corrections as a function of each observable in the above correction distributions are observed very low because, besides the matching loss, the loss is mainly governed by the working points of the  $b$ -tagging (70%) and top-tagging (50%) algorithms as shown in Fig. 7.5 and 7.6. The off-diagonal elements describe the fraction of particle level events that migrate into other bins. Examples of the migration matrices for several variables are shown in Fig 7.7 and 7.8.

The inclusive cross-section for  $t\bar{t}$  pairs in the fiducial phase space, obtained by

integrating the absolute differential cross-section  $d\sigma^{\text{fid}}/dX^i$ , is used to determine the normalized differential cross-section  $1/\sigma^{\text{fid}} \cdot d\sigma^{\text{fid}}/dX^i$ .

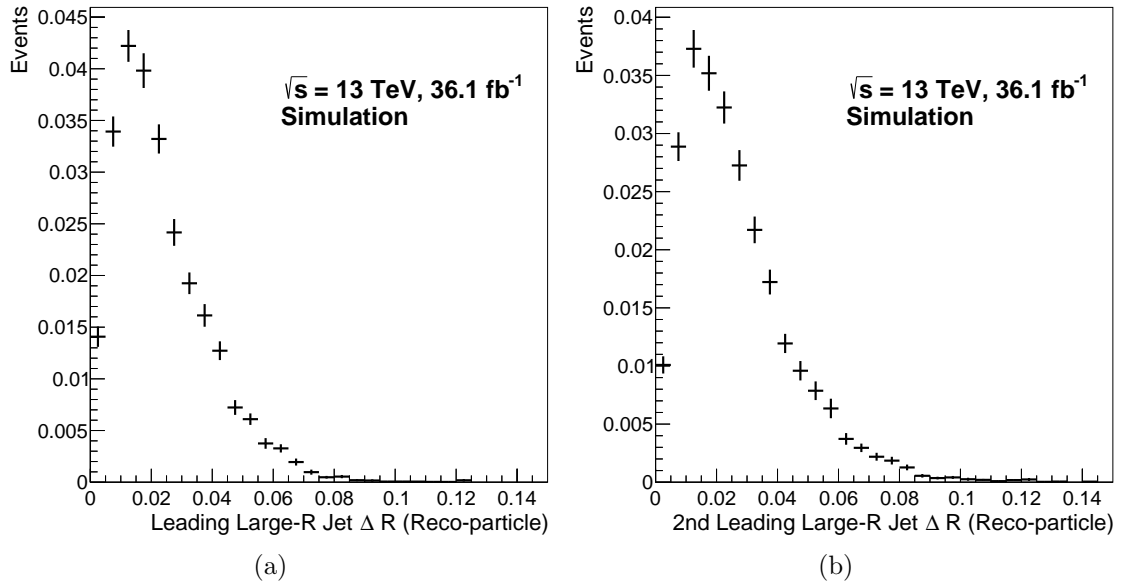
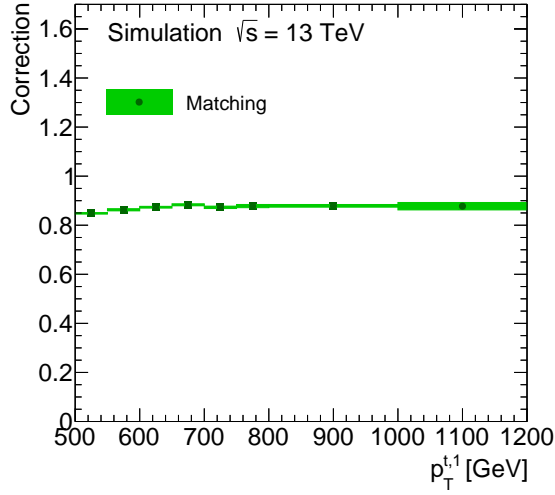
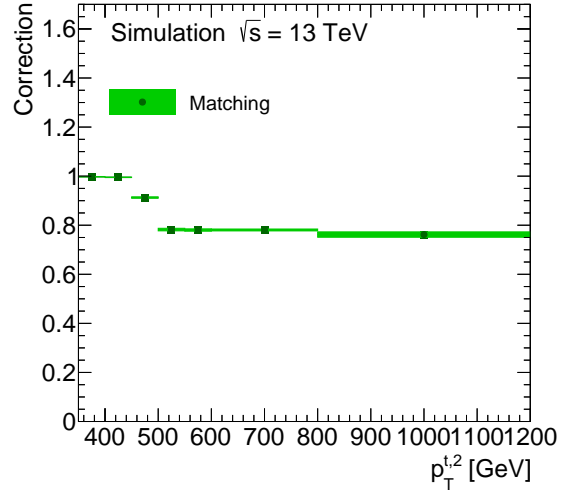


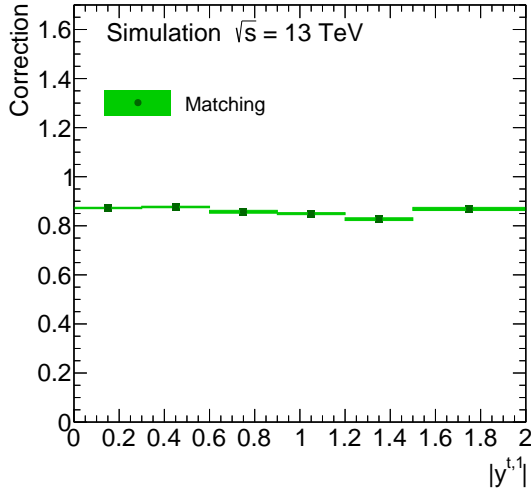
Figure 7.2: Angular separation between detector- and particle-level for (a) Leading and (b) 2nd Leading Large-R jets.



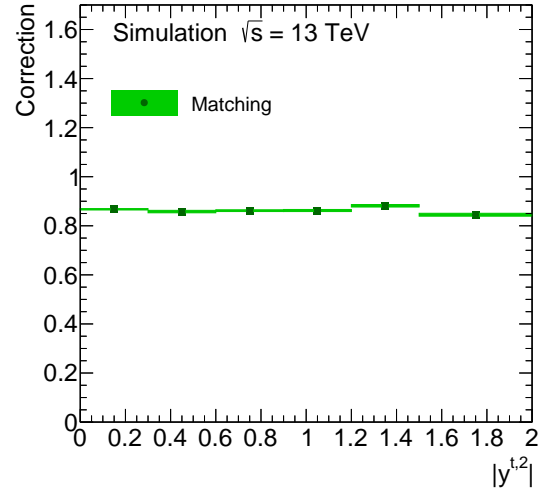
(a)



(b)

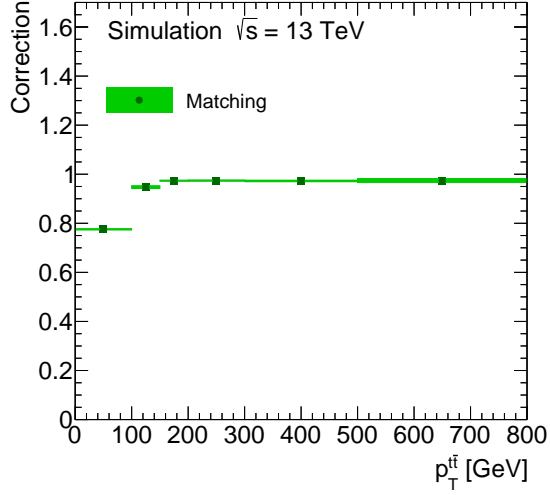


(c)

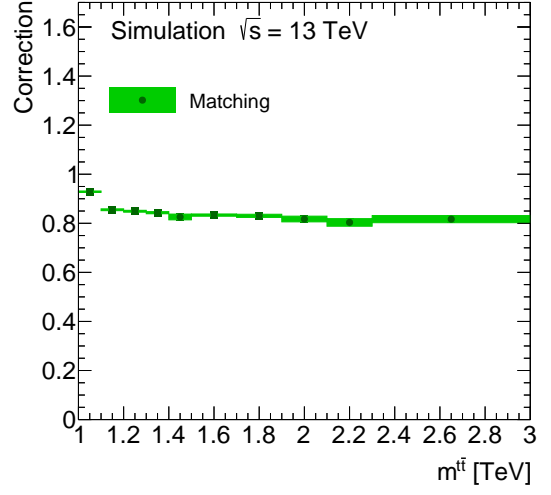


(d)

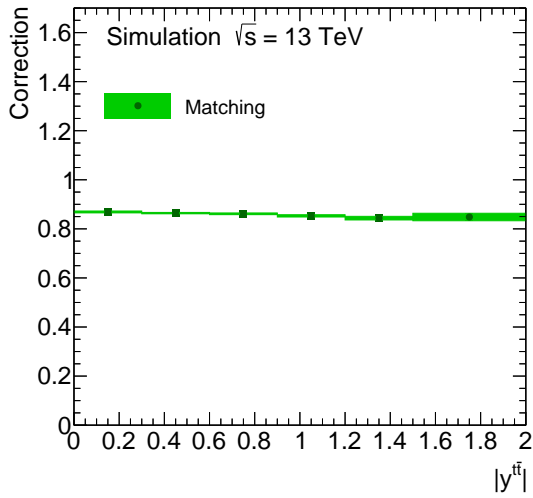
Figure 7.3: Fiducial phase-space matching correction as a function of (a) transverse momentum and (c) absolute value of the rapidity of the Leading top-quark, and (b) transverse momentum and (d) absolute value of the rapidity of the 2nd Leading top-quark. The green bands indicate the statistical uncertainty.



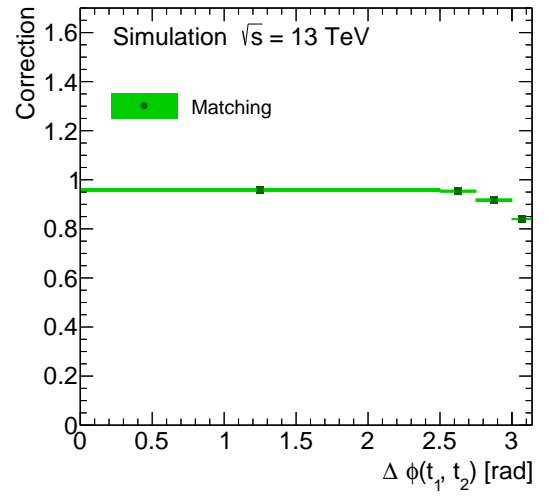
(a)



(b)

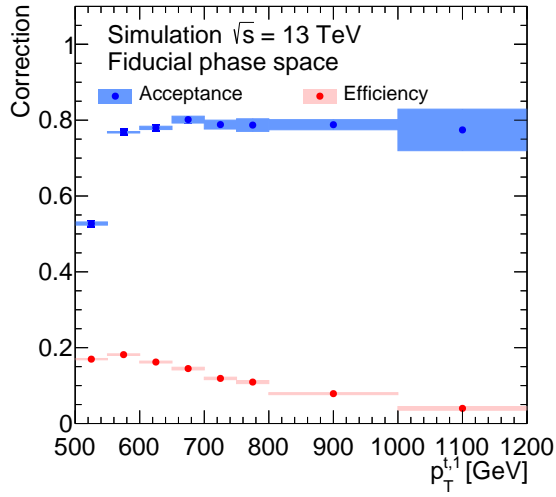


(c)

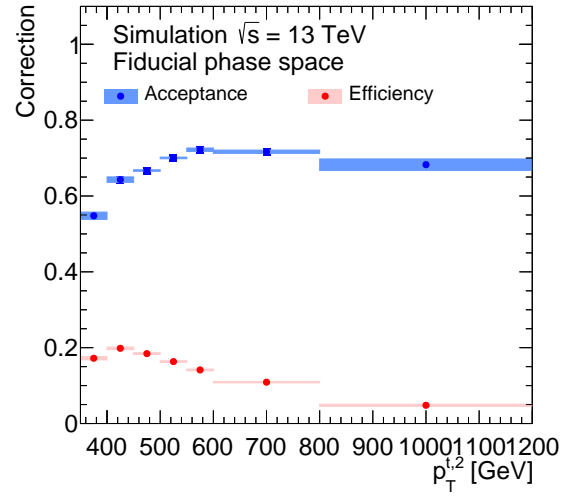


(d)

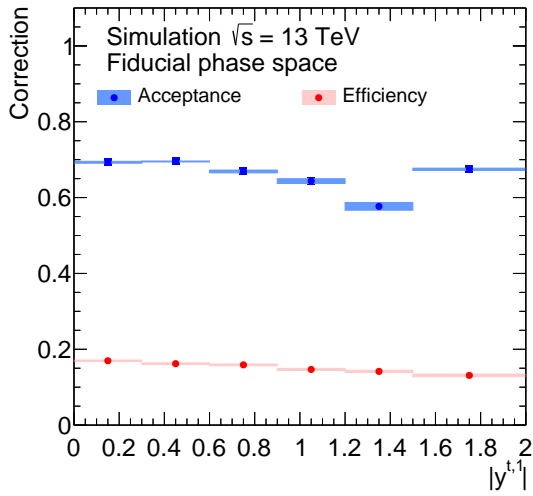
Figure 7.4: Fiducial phase-space matching correction of (a) transverse momentum, (b) invariant mass, (c) absolute value of the rapidity and (d)  $\Delta\phi(t_1, t_2)$  of the  $t\bar{t}$  system. The green bands indicate the statistical uncertainty.



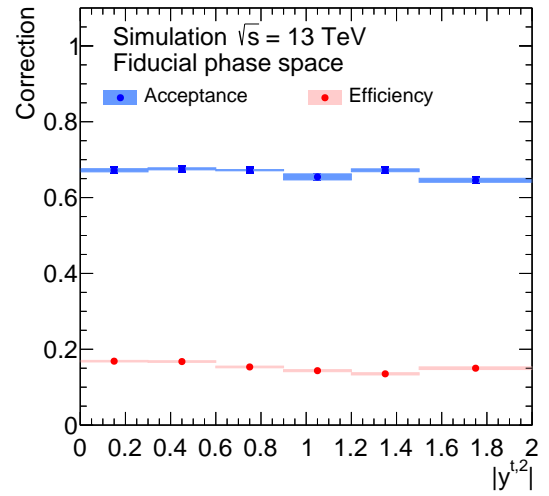
(a)



(b)

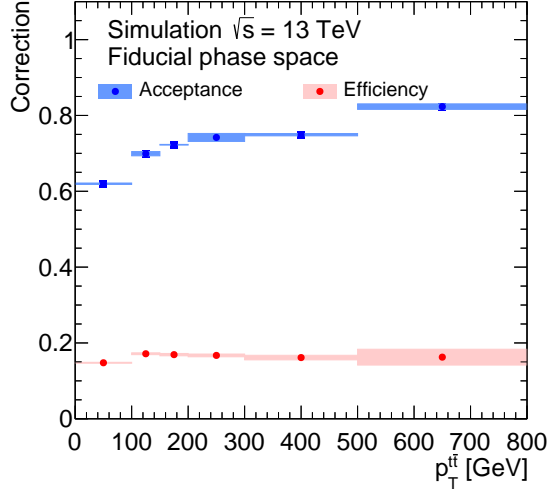


(c)

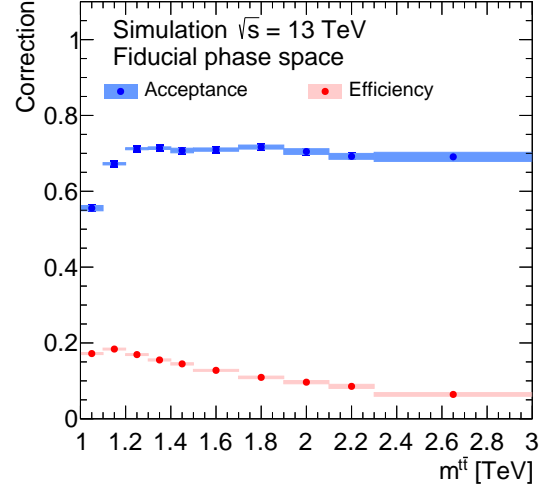


(d)

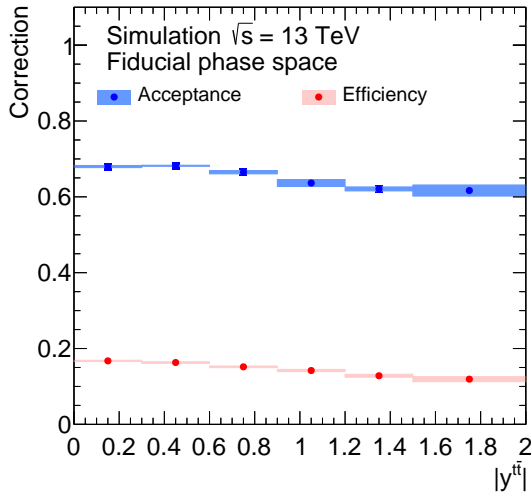
Figure 7.5: Fiducial phase-space acceptance and efficiency corrections as a function of (a) transverse momentum and (c) absolute value of the rapidity of the Leading top-quark, and (b) transverse momentum and (d) absolute value of the rapidity of the 2nd Leading top-quark.



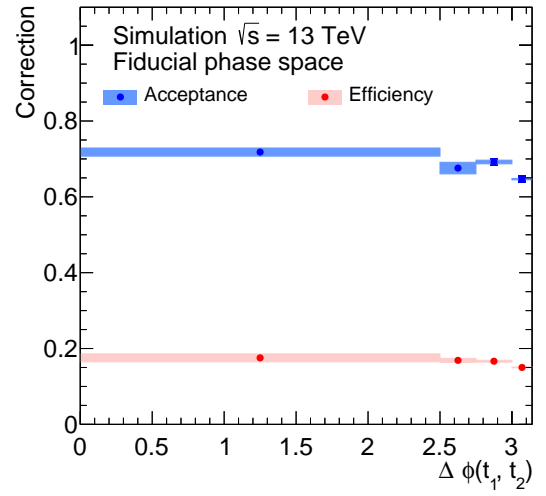
(a)



(b)



(c)



(d)

Figure 7.6: Fiducial phase-space acceptance and efficiency corrections as a function of (a) transverse momentum, (b) invariant mass, (c) absolute value of the rapidity and (d)  $\Delta\phi(t_1, t_2)$  of the  $t\bar{t}$  system.

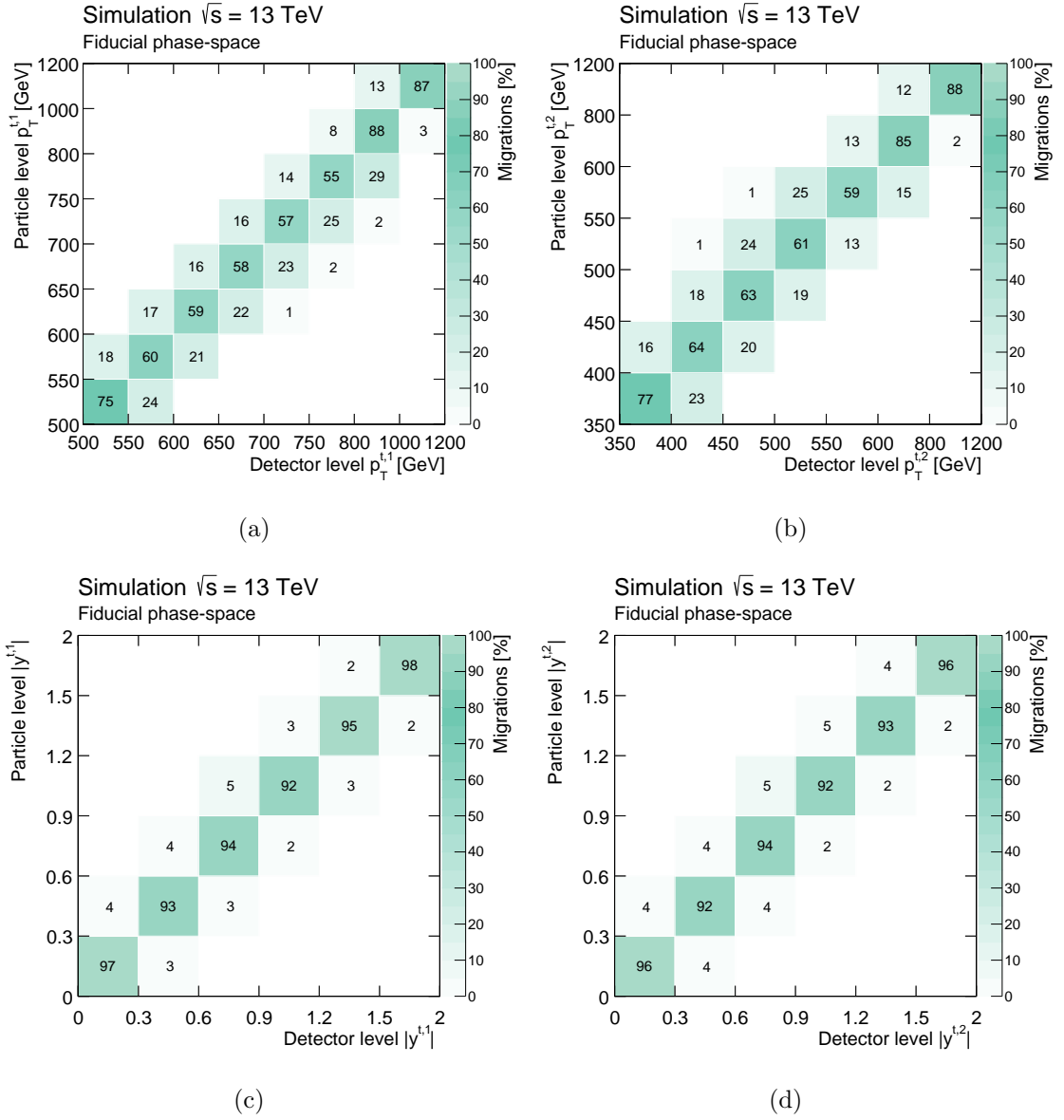


Figure 7.7: Fiducial phase-space migration matrices of (a) transverse momentum and (c) absolute value of the rapidity of the Leading top-quark, and (b) transverse momentum and (d) absolute value of the rapidity of the 2nd Leading top-quark.

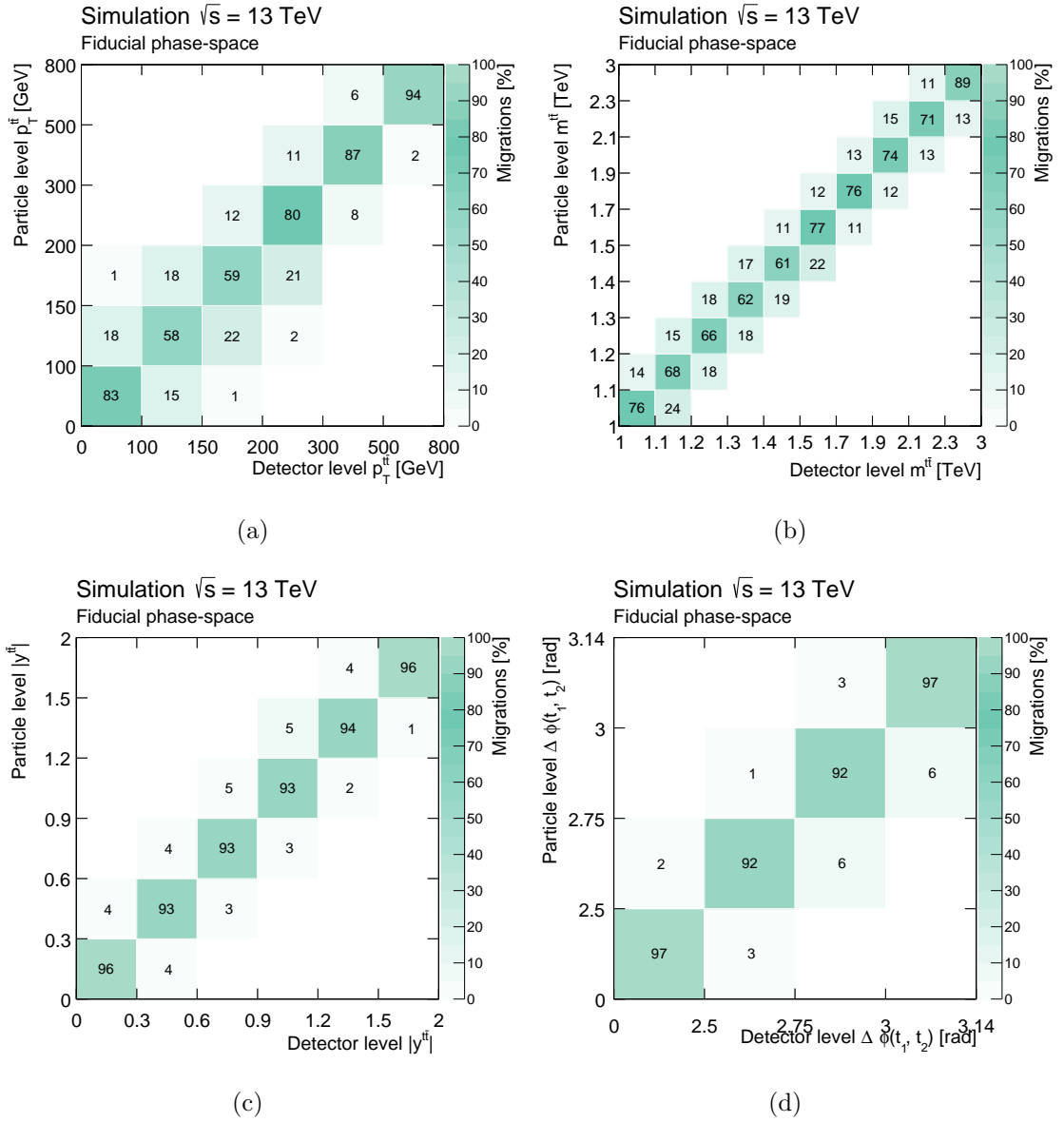


Figure 7.8: Fiducial phase-space migration matrices of (a) transverse momentum, (b) invariant mass, (c) absolute value of the rapidity, and (d)  $\Delta\phi(t_1, t_2)$  of the  $t\bar{t}$  system.

# Chapter 8

## Systematic uncertainties

The statistical and systematic uncertainties for the particle level results are propagated and combined through so-called pseudo-experiment technique, estimated using the data as well as the nominal and alternative MC samples. Section 8.1 briefly describes about the pseudo-experiment by taking a simple example. Covariance provides a measure of the strength of the correlation between two or more sets of random variates. For instance, the covariance for two random variates  $x$  and  $y$ ,  $\text{cov}(x,y)$ , is formulated Eq. 8.1. The corresponding correlation is Eq. 8.2, the value  $\text{cov}(x,y)$  is zero if  $x$  and  $y$  are uncorrelated. The section 8.1 also details how to construct the covariance in this analysis using the pseudo-experiment technique. The description related to systematic uncertainties is given in Section 8.2. Section 8.3 is devoted to detailed discussion on one of the major source of systematic uncertainties, namely the signal modelling uncertainty.

$$\begin{aligned}\text{Cov}(x, y) &= \langle (x_i - \langle x \rangle)(y_i - \langle y \rangle) \rangle \\ &= \langle xy \rangle - \langle x \rangle \langle y \rangle\end{aligned}\tag{8.1}$$

$$\text{Corr}(x, y) = \frac{\text{Cov}(x, y)}{\sigma_x \sigma_y}\tag{8.2}$$

### 8.1 Propagation of systematic uncertainties and treatment of correlations

#### 8.1.1 Pseudo-experiment

The pseudo-experiment is widely used in particle physics in order to evaluate the performance of hypothesis and estimate the uncertainty. The pseudo-experiment is generated based on “Toy” MC simulation. The Toy MC simulation is to deal with fluctuation on final distributions without performing a full simulation. For instance, it gives the procedure of estimating statistical uncertainty using a series of pseudo-experiments. The scheme of the serial pseudo-experiments shows in Fig. 8.1. The blue histogram is the original distribution and the distribution with red dash

line is fluctuated by Poisson distribution independently for each bin according to its number of events. To obtain the error of each bin in the original distribution, the first bin is as an example, a new histogram is filled with the contents of these fluctuated distributions from the first bin (red dash histograms). The standard deviation of this new histogram (red histogram) as shown in Fig. 8.1, is obtained as the standard deviation of the first bin of the original distribution.

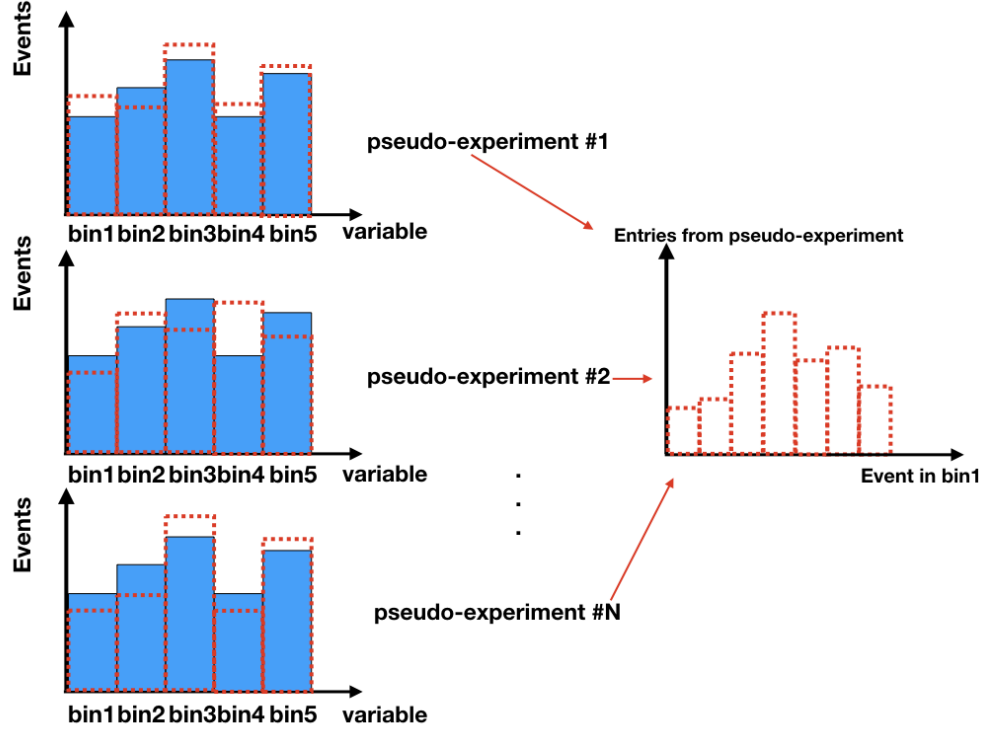


Figure 8.1: Pseudo-experiment, blue represents original distribution, dashed red line represents fluctuated distribution after doing an pseudo-experiment. The standard deviation of the first bin is obtained from the red histogram filled by a serial pseudo-experiments.

The formula for propagation of error for  $Y = f(X_1, X_2, \dots)$ , a function of one or more variables with measurements  $(X_1, X_2, \dots)$ , gives the following estimate for the standard deviation of  $Y$ :

$$\sigma_Y = \sqrt{\left(\frac{\partial Y}{\partial X_1}\right)^2 \sigma_{X_1}^2 + \left(\frac{\partial Y}{\partial X_2}\right)^2 \sigma_{X_2}^2 + \dots} \quad (8.3)$$

Assuming the variables  $X_1, X_2, \dots$ , are uncorrelated, the error  $\sigma_Y$  can also be estimated by taking the standard deviation of the distribution of pseudo-experiments on the distribution  $N_Y$ :

$$Y_j^{toy} = \left(\frac{\partial Y}{\partial X_1}\right)(X_1 + \lambda_1 \sigma_1) + \left(\frac{\partial Y}{\partial X_2}\right)(X_2 + \lambda_2 \sigma_2) + \dots, \quad (8.4)$$

where  $Y_j^{toy}$  is the result obtained from the  $j$ -th pseudo-experiment,  $\lambda_1$  is a Gaussian

random number with mean  $\mu = 0$  and standard derivation of  $\sigma = 1$ . In case of the variable  $X_i$  which is a integer number (e.g. number of events), such as  $X_i \equiv N_i$ ,  $X_i + \lambda_i \sigma_i$  can be replaced with Poisson fluctuated number of events,  $\mathcal{P}(N_i)$ . This procedure can be extended to the total systematic error estimation from  $N_{syst}$  number of systematic uncertainty sources.

In this analysis, the correlations of bin-to-bin and systematics are taken into account by constructing a covariance matrix, as described below.

## 8.1.2 Covariance Matrix

The covariance matrix of all the uncertainties considered in the analysis was also derived using the pseudo-experiment technique. The covariance matrix used to allow quantitative comparisons with theoretical predictions, will be presented in Chapter 9. Because of different source of uncertainties, the covariance matrix is derived by summing two covariance matrices following the same approach used in Refs. [49, 50].

The first covariance matrix incorporates uncertainties from statistical effects, detector related sources, background modelling and limited size of the simulated samples. This covariance matrix is called “non-modelling part”. The procedure of a given pseudo-experiment is described below:

- the data distribution  $dN/dX$  contains the signal and background. The statistical uncertainty contribution for  $i$ -th bin is estimated as  $\Delta_i^{stat,toy} = \mathcal{P}(N_i^{obs}) - N_i^{obs}$  independently for each bin, where  $\mathcal{P}(N_i^{obs})$  is the number obtained from a Poisson distribution with  $N_i^{obs}$  as mean value.
- For each systematic uncertainty  $k$ :
  - a Gaussian random number  $\lambda_k^{toy}$  is given by with mean  $\mu = 0$  and  $\sigma = 1$ .
  - for  $i$ -th bin:
    - \* the difference  $\delta_{k,i}^\pm = N_{k,i}^{MC} - N_{nominal,i}^{MC}$ , where  $N_{k,i}^{MC} = (N_{signal}^{MC} + N_{bkg}^{MC})_{k,i}$  is the number of events expected in the systematically varied estimate for the  $k$ -th systematic uncertainty estimate and  $N_{nominal,i}^{MC} = (N_{signal}^{MC} + N_{bkg}^{MC})_{nominal,i}$  is the number of events expected in the nominal estimate. The  $\delta_{k,i}^+$  difference refers to the  $1\sigma$  variation of the systematic contribution in the positive direction (usually indicated as “up”) while the  $\delta_{k,i}^-$  difference refers to the  $1\sigma$  variation in the negative direction (usually indicated as “down”). In the case of a one sided systematic uncertainty, the contribution is symmetrized:  $\delta_{k,i}^+ = |\delta_{k,i}^-|$ .
    - \* a systematic variation is evaluated as  $\Delta_{k,i}^{toy} = \delta_{k,i}^\pm \cdot |\lambda_k^{toy}|$ , where the  $\delta_{k,i}^+$  is used in the case  $\lambda_k^{toy} > 0$  and  $\delta_{k,i}^-$  in the case  $\lambda_k^{toy} < 0$ .
    - \* assuming the same relative systematic shift in data and MC, the variation in the pseudo-experiment is rescaled to the statistically varied number of event  $\tilde{\Delta}_{k,i}^{toy} = \frac{\mathcal{P}(N_i^{obs})}{(N_{signal}^{MC} + N_{bkg}^{MC})_{nominal,i}} \cdot \Delta_{k,i}^{toy}$

- the procedure to obtain the  $i$ -th bin content in  $l$ -th pseudo-experiment varied for statistical and  $N_{syst}$  systematics contributions is formulated in the following equation:

$$\begin{aligned}
N_{i,l}^{toy} &= N_i^{obs} + \Delta_i^{stat,toy} + \sum_{k=1}^{N_{syst}} \tilde{\Delta}_{k,i}^{toy} \\
&= N_i^{obs} + (\mathcal{P}(N_i^{obs}) - N_i^{obs}) + \sum_{k=1}^{N_{syst}} \frac{\mathcal{P}(N_i^{obs})}{(N_{signal}^{MC} + N_{bkg}^{MC})_{nominal,i}} \cdot \Delta_{k,i}^{toy} \quad (8.5) \\
&= \mathcal{P}(N_i^{obs}) \cdot \left(1 + \sum_{k=1}^{N_{syst}} \frac{1}{(N_{signal}^{MC} + N_{bkg}^{MC})_{nominal,i}} \cdot \delta_{k,i}^{\pm} \cdot |\lambda_k^{toy}|\right)
\end{aligned}$$

Assuming the number of trials is 10000, for example, the 10000 resulting differential cross sections obtained from these pseudo-experiments are used to produce a covariance matrix following the formula:

$$d\sigma_{i,l} = N_{i,l}^{toy} / \Delta X_{(bin \ width)}, \quad l = 0, 1, \dots, 10000 \quad (8.6)$$

$$\text{Cov}^{non-mod}(i, j) = \langle (d\sigma_{i,l} - \langle d\sigma_i \rangle) \cdot (d\sigma_{j,l} - \langle d\sigma_j \rangle) \rangle, \quad (8.7)$$

where  $i, j$  are the  $i$ -th and  $j$ -th bins and the averages are performed over the number of pseudo-experiments. The corresponding correlation matrices are evaluated by the following equation.

$$\text{Corr}^{non-mod}(i, j) = \text{Cov}^{non-mod}(i, j) / \sqrt{\text{Cov}^{non-mod}(i, i) \text{Cov}^{non-mod}(j, j)}. \quad (8.8)$$

The second covariance matrix, called ‘‘modelling part’’, refers to the uncertainties related to  $t\bar{t}$  generators such as variation in ME, parton shower and hadronisation, ISR/FSR and PDF uncertainties as described in Section 4.2. The uncertainties from these sources are estimated by taking difference between models. It is not clear, however, how these uncertainties between the bins are correlated and it is necessary to assume the correlations. In this analysis, the bin-to-bin uncertainties are assumed to be fully correlated using the following procedure.

- Assuming the systematic uncertainty is varied on nominal distribution which is as baseline, replacing both  $\mathcal{P}(N_i^{obs})$  and  $(N_{signal}^{MC} + N_{bkg}^{MC})_{nominal,i}$  with  $N_{nominal,i}$ , the Eq. 8.5 is changed as:

$$N_{k,i}^{toy} = N_{nominal,i} \cdot \left(1 + \frac{1}{N_{nominal,i}} \cdot \delta_{k,i}^{\pm} \cdot |\lambda_k^{toy}|\right). \quad (8.9)$$

The standard deviation for the systematic uncertainty is obtained also by using 10000 pseudo-experiments. This gives diagonal part of the covariance matrix  $\text{Cov}^k(i, i) = \sigma_{toy}^2(i, i)$ .

- Assuming the bin-to-bin correlation value being set to unity, the covariance matrix of  $k$ -th generator uncertainty can be obtained by Eq. 8.11.

$$\text{Corr}^k(i, j) = 1 \quad (8.10)$$

$$\text{Cov}^k(i, j) = \text{Corr}^k(i, j) \cdot \sqrt{\text{Cov}^k(i, i) \text{Cov}^k(j, j)}. \quad (8.11)$$

The covariance matrix for modelling part obtained by summing the covariance matrices of all generator uncertainties, and the corresponding correlation matrix are evaluated as the following formulas.

$$\text{Cov}^{\text{mod}}(i, j) = \sum_k \text{Cov}^k(i, j) \quad (8.12)$$

$$\text{Corr}^{\text{mod}}(i, j) = \text{Cov}^{\text{mod}}(i, j) / \sqrt{\text{Cov}^{\text{mod}}(i, i) \text{Cov}^{\text{mod}}(j, j)}. \quad (8.13)$$

In order to obtain the full covariance matrix, the above two covariance matrices, non-modelling and modelling parts, are combined by summing them with the following formula. The example for full covariance and correlation shows in the following tables. Details of covariance and correlation as other variables are shown in Appendix 11.2.

$$\text{Cov}^{\text{total}}(i, j) = \text{Cov}^{\text{non-mod}}(i, j) + \text{Cov}^{\text{mod}}(i, j) \quad (8.14)$$

$$\text{Corr}^{\text{total}}(i, j) = \text{Cov}^{\text{total}}(i, j) / \sqrt{\text{Cov}^{\text{total}}(i, i) \text{Cov}^{\text{total}}(j, j)}. \quad (8.15)$$

bin [GeV]	500-550	550-600	600-650	650-700	700-750	750-800	800-1000	1000-1200
500-550	$2.60 \times 10^{-7}$	$1.72 \times 10^{-7}$	$1.00 \times 10^{-7}$	$8.19 \times 10^{-8}$	$4.89 \times 10^{-8}$	$3.07 \times 10^{-8}$	$1.59 \times 10^{-8}$	$2.83 \times 10^{-9}$
550-600	$1.72 \times 10^{-7}$	$1.32 \times 10^{-7}$	$7.25 \times 10^{-8}$	$5.51 \times 10^{-8}$	$3.36 \times 10^{-8}$	$2.16 \times 10^{-8}$	$1.09 \times 10^{-8}$	$1.83 \times 10^{-9}$
600-650	$1.00 \times 10^{-7}$	$7.25 \times 10^{-8}$	$4.82 \times 10^{-8}$	$3.38 \times 10^{-8}$	$1.93 \times 10^{-8}$	$1.29 \times 10^{-8}$	$6.71 \times 10^{-9}$	$1.21 \times 10^{-9}$
650-700	$8.19 \times 10^{-8}$	$5.51 \times 10^{-8}$	$3.38 \times 10^{-8}$	$3.35 \times 10^{-8}$	$1.76 \times 10^{-8}$	$9.70 \times 10^{-9}$	$5.60 \times 10^{-9}$	$1.06 \times 10^{-9}$
700-750	$4.89 \times 10^{-8}$	$3.36 \times 10^{-8}$	$1.93 \times 10^{-8}$	$1.76 \times 10^{-8}$	$1.54 \times 10^{-8}$	$7.20 \times 10^{-9}$	$3.24 \times 10^{-9}$	$7.74 \times 10^{-10}$
750-800	$3.07 \times 10^{-8}$	$2.16 \times 10^{-8}$	$1.29 \times 10^{-8}$	$9.70 \times 10^{-9}$	$7.20 \times 10^{-9}$	$6.66 \times 10^{-9}$	$2.12 \times 10^{-9}$	$3.29 \times 10^{-10}$
800-1000	$1.59 \times 10^{-8}$	$1.09 \times 10^{-8}$	$6.71 \times 10^{-9}$	$5.60 \times 10^{-9}$	$3.24 \times 10^{-9}$	$2.12 \times 10^{-9}$	$1.65 \times 10^{-9}$	$1.84 \times 10^{-10}$
1000-1200	$2.83 \times 10^{-9}$	$1.83 \times 10^{-9}$	$1.21 \times 10^{-9}$	$1.06 \times 10^{-9}$	$7.74 \times 10^{-10}$	$3.29 \times 10^{-10}$	$1.84 \times 10^{-10}$	$3.79 \times 10^{-10}$

Table 8.1: Covariance matrix for the absolute particle-level fiducial phase-space differential cross-section as a function of the transverse momentum of the leading top-quark jet , accounting for the statistical and systematic uncertainties.

bin [GeV]	500-550	550-600	600-650	650-700	700-750	750-800	800-1000	1000-1200
500-550	<b>1.00</b>	0.93	0.90	0.88	0.77	0.74	0.77	0.28
550-600	0.93	<b>1.00</b>	0.91	0.83	0.75	0.73	0.74	0.26
600-650	0.90	0.91	<b>1.00</b>	0.84	0.71	0.72	0.75	0.28
650-700	0.88	0.83	0.84	<b>1.00</b>	0.78	0.65	0.75	0.30
700-750	0.77	0.75	0.71	0.78	<b>1.00</b>	0.71	0.64	0.32
750-800	0.74	0.73	0.72	0.65	0.71	<b>1.00</b>	0.64	0.21
800-1000	0.77	0.74	0.75	0.75	0.64	0.64	<b>1.00</b>	0.23
1000-1200	0.28	0.26	0.28	0.30	0.32	0.21	0.23	<b>1.00</b>

Table 8.2: Correlation matrix for the absolute particle-level fiducial phase-space differential cross-section as a function of the transverse momentum of the leading top-quark jet , accounting for the statistical and systematic uncertainties.

## 8.2 Dominant systematic uncertainties

Systematic uncertainties resulting from object reconstruction and calibration, MC generator modeling and background estimation, are described below. A summary of all the systematic uncertainties for integrated cross section is presented in Tab. 8.3. The detail for the contribution of all the systematic uncertainties is in Appendix 11.1.

Source	
Total Uncertainty [%]	$\pm 24.4$
Statistics [%]	$\pm 2.3$
Systematics [%]	$\pm 24.3$
Luminosity [%]	$\pm 2.01$
Large- $R$ jets JES [%]	$\pm 5.91$
Large- $R$ jets JMS [%]	$\pm 1.44$
Large- $R$ jets top-tagging ( $\tau_{32}$ ) [%]	$\pm 12.5$
Flavor tagging [%]	$\pm 8.29$
Small- $R$ jets [%]	$\pm 0.28$
Pile-up [%]	$\pm 0.55$
Background [%]	$\pm 0.89$
(MOD) Monte Carlo sample statistics [%]	$\pm 0.90$
(MOD) ISR/FSR + scale [%]	$\pm 1.13$
(MOD) Alternative hard-scattering model [%]	$\pm 11.2$
(MOD) Alternative parton-shower model [%]	$\pm 13.7$
Lepton energy scale and resolution [%]	$\pm 0.02$
PDF [%]	$\pm 2.67$

Table 8.3: Summary of the largest systematic and statistical relative uncertainties for the absolute particle level fiducial phase space cross section measurement in percent.

**Luminosity** The uncertainty on the integrated luminosity is  $\pm 2.0\%$ . It is derived from the calibration of the luminosity scale using  $x - y$  beam separation scans by comparing luminosity result from Van der Meer scans with a given specific luminosity with same luminosity monitor.

**Object reconstruction and calibration** The estimation of Large- $R$  jet energy scale (JES) and jet mass (JMS) uncertainties [51] are derived from studying tracking and calorimeter measurements and comparing these in data and MC simulations. The total uncertainty from jet calibration and reconstruction on differential cross section ranges from  $\pm 11\%$  to  $\pm 30\%$  for Large- $R$  jet  $p_T$  over the range 350 to 900 GeV as shown in Fig. 8.2. The Small- $R$  jet energy scale uncertainty is derived the difference between data and MC simulations by *in situ* calibration method [52, 53, 54]. This method is to obtain the difference by balancing the  $p_T$  of a jet against other well measured reference objects, such as  $Z/\gamma$ +jet balance, the  $p_T$  of a jet against a  $Z$  boson or a photon, where  $Z$  boson momenta are precisely reconstructed by muon

pairs in muon detector. Additional uncertainty contributions come from calorimeter response to the jet flavour and simulated jet composition of light quark ( $u, d$  etc.),  $b$ -quark, and gluon initiated jets. Uncertainties in the jet energy resolution (JER) are obtained with an *in situ* measurement of the jet response asymmetry in dijet events [55]. It is based on momentum conservation in the transverse plane to measure the dijet balance. The lepton energy scale and resolution are varied within their uncertainties [56, 57].

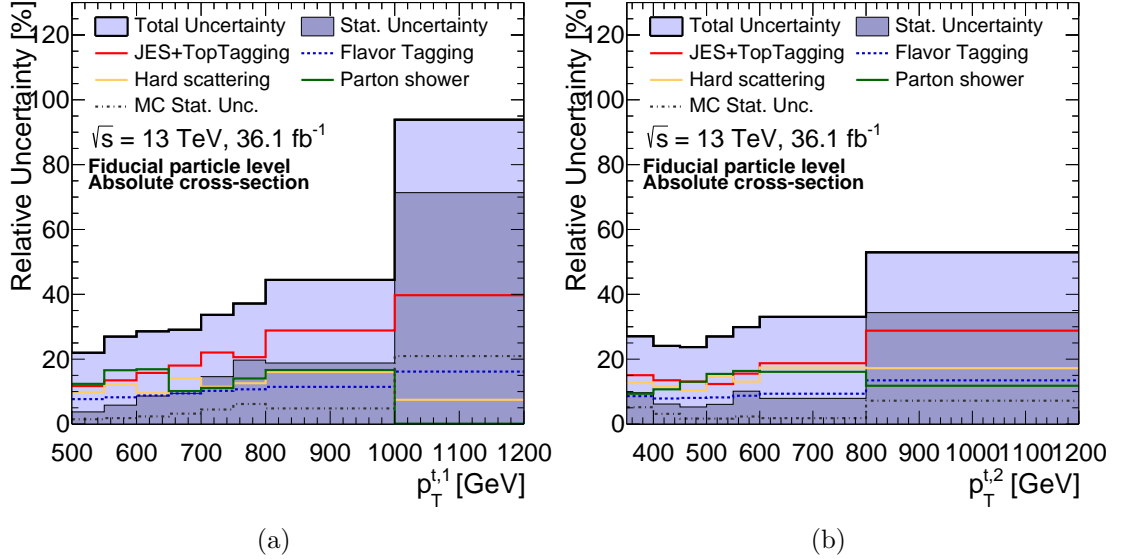


Figure 8.2: Fractional uncertainties as a function of transverse momentum of (a) the Leading Large-R jet and (b) 2nd Leading Large-R jet in the fiducial phase-space.

**Background** Background uncertainty comes from the background estimates. It is from the subtraction of other background in the control regions and the uncertainty with tagging correction coefficients ( $k_{t_1, b_2}, k_{t_2, b_1}, k_{t_1, t_2}$  and  $k_{b_1, b_2}$ ) in the formula of multijet background estimation (Eq. 6.5). The uncertainty in the subtraction of the all-hadronic  $t\bar{t}$  events in the control regions comes from the uncertainties on the  $t\bar{t}$  cross section and  $b$ -tagging algorithms. The uncertainty is estimated by the Eq. 6.5 with the fluctuation on all regions of the formula by pseudo-experiments. The background uncertainty ranges from  $\pm 2$  to  $\pm 5\%$  for Large-R jet  $p_T$  ranging from 350 to 900 GeV, respectively.

**Signal modelling** The difference between the unfolded distribution of an alternative model and its own particle-level distribution is used as the estimate of the corresponding systematic uncertainty on the unfolded differential cross sections.

To evaluate the uncertainty related to the different ME (introduced in Section 4.2) simulation, aMC@NLO+PYTHIA8 events are unfolded using the migration matrix and correction factors derived from the nominal POWHEG+PYTHIA8 sample. This uncertainty is depending on the variables, 20 – 30% at Large-R jet  $p_T^t$  as

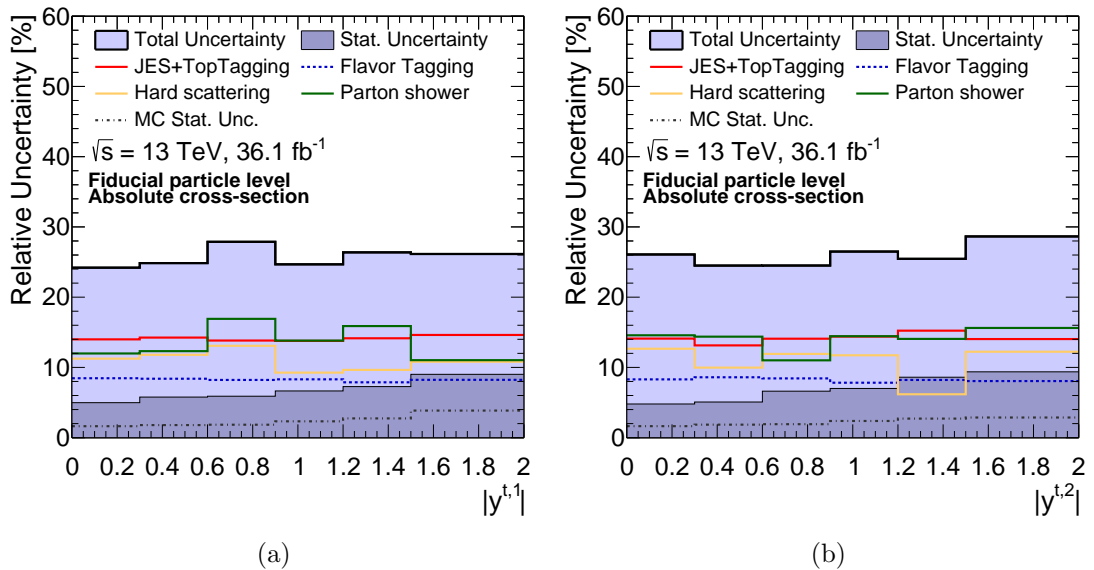


Figure 8.3: Fractional uncertainties as a function of rapidity of (a) the Leading Large-R jet and (b) 2nd Leading Large-R jet in the fiducial phase-space.

shown in Fig. 8.2, and 10 – 15% at Large-R jet rapidity as shown in Fig 8.3, Fractional uncertainties related to other observables are shown in Fig. 8.4 shows other observables.

To estimate the uncertainty associated with the choice of parton shower and hadronization models, comparison is made of the unfolded particle level distribution of simulated events generated by POWHEG interfaced to the HERWIG7 parton shower and hadronization using nominal POWHEG+PYTHIA8 corrections and unfolding matrices. The resulting systematic uncertainties are 5 – 15%.

In order to evaluate the uncertainty related to the modelling initial and final state radiation (ISR/FSR) introduced in Section 4.2, two  $t\bar{t}$  MC samples are produced with more or less QCD radiation by changing renormalization ( $\mu_f$ ), factorization ( $\mu_R$ ) and `hdamp` parameters, where `hdamp` is to regulate the high  $p_T$  emission against which the  $t\bar{t}$  system recoils. The two samples use same PDF set as for the nominal sample. This uncertainty is within 10 – 15%.

The uncertainty related to PDF is assessed using the POWHEG+PYTHIA8 sample. The spectra is determined by reweighting the central prediction of the PDF4LHC PDF set [58] and applying relative variation to the nominal distributions. This uncertainty is about 3%.

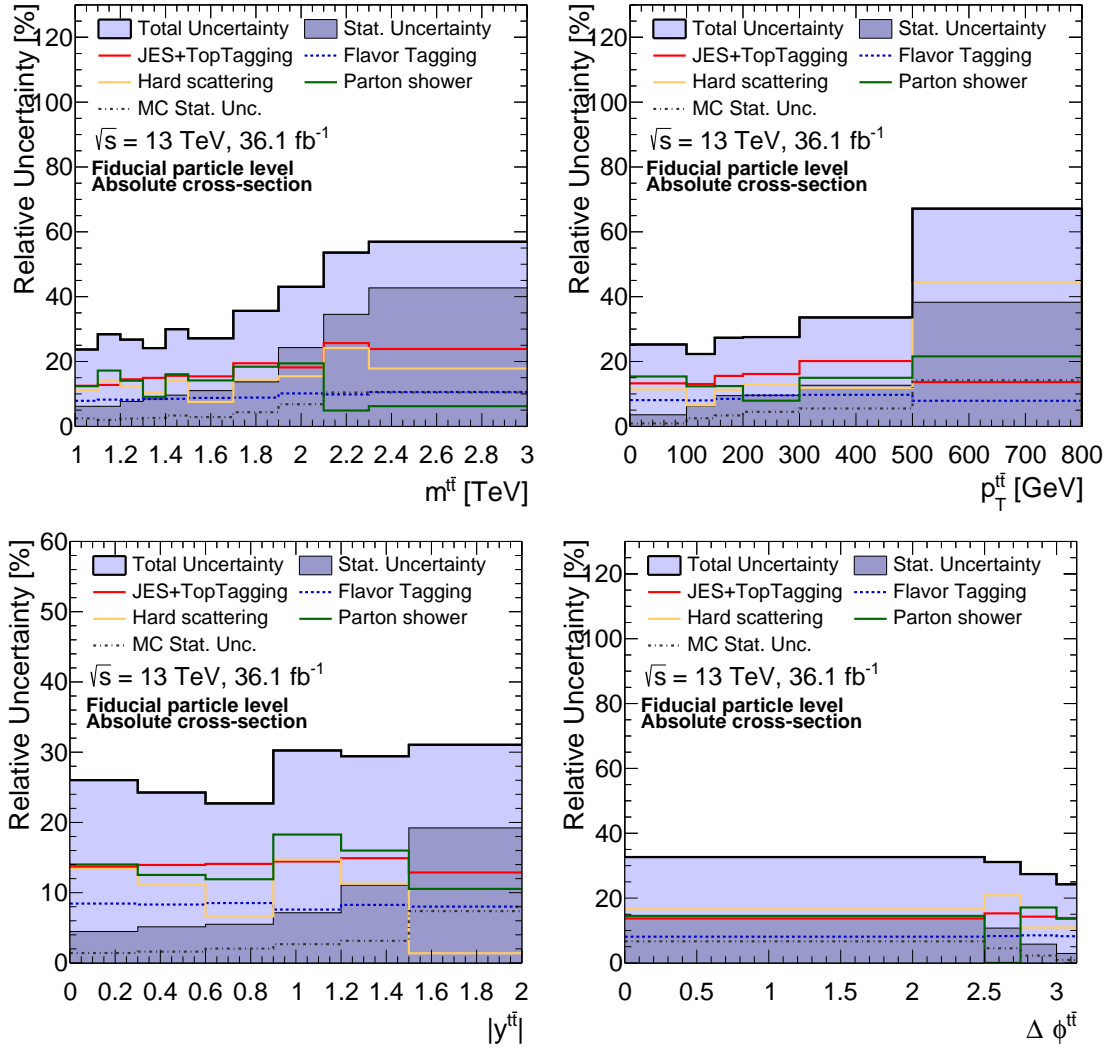


Figure 8.4: Fractional uncertainties for the absolute differential cross-sections as a function of the  $t\bar{t}$  invariant mass, transverse momentum, rapidity and  $\Delta\phi(t_1, t_2)$  in the fiducial phase-space.

## 8.3 Detailed study on signal modelling uncertainties

### 8.3.1 Comparison of POWHEG+PYTHIA8 with POWHEG+HERWIG7

The parton shower and top tagging are the two largest uncertainties as seen in the source of uncertainties with Tab. 8.3. In order to understand this problem, the variables used in the top tagging, i.e.  $\tau_{32}$  and the large jet mass distributions, are studied for these two models in this section. The study was done by comparing the two models in each step of the event selection to see where in selection criteria the two models start to differ.

Fig. 8.5, 8.6 and 8.7 shows the  $\tau_{32}$  distributions for each cut step on detector level. A clear difference appeared in the ratio of POWHEG+HERWIG7 (hereafter PWG+H7) to POWHEG+PYTHIA8 (PWG+PY8) after the mass cut ( $|\Delta m| < 50$  GeV) step as seen in Fig. 8.6(b). In order to investigate the cause of the difference at the mass cut step, the mass distributions themselves are also investigated. They are shown in Fig.8.8. PWG+H7 gives more events in the low mass region than PWG+PY8, while the top mass peak is more prominent in PWG+PY8. This results in larger decrease in the number of events after the mass cut for PWG+H7.

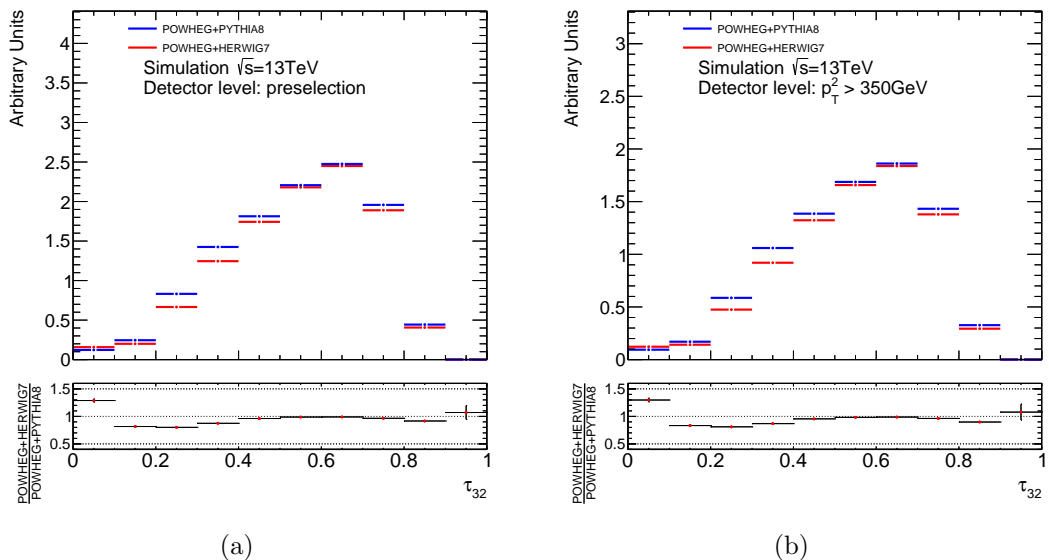


Figure 8.5:  $\tau_{32}$  for each step of event selection at the detector level. (a) after preselection and trigger. (b) after selecting two large jets  $p_T > 350$  GeV. Cuts are applied sequentially.

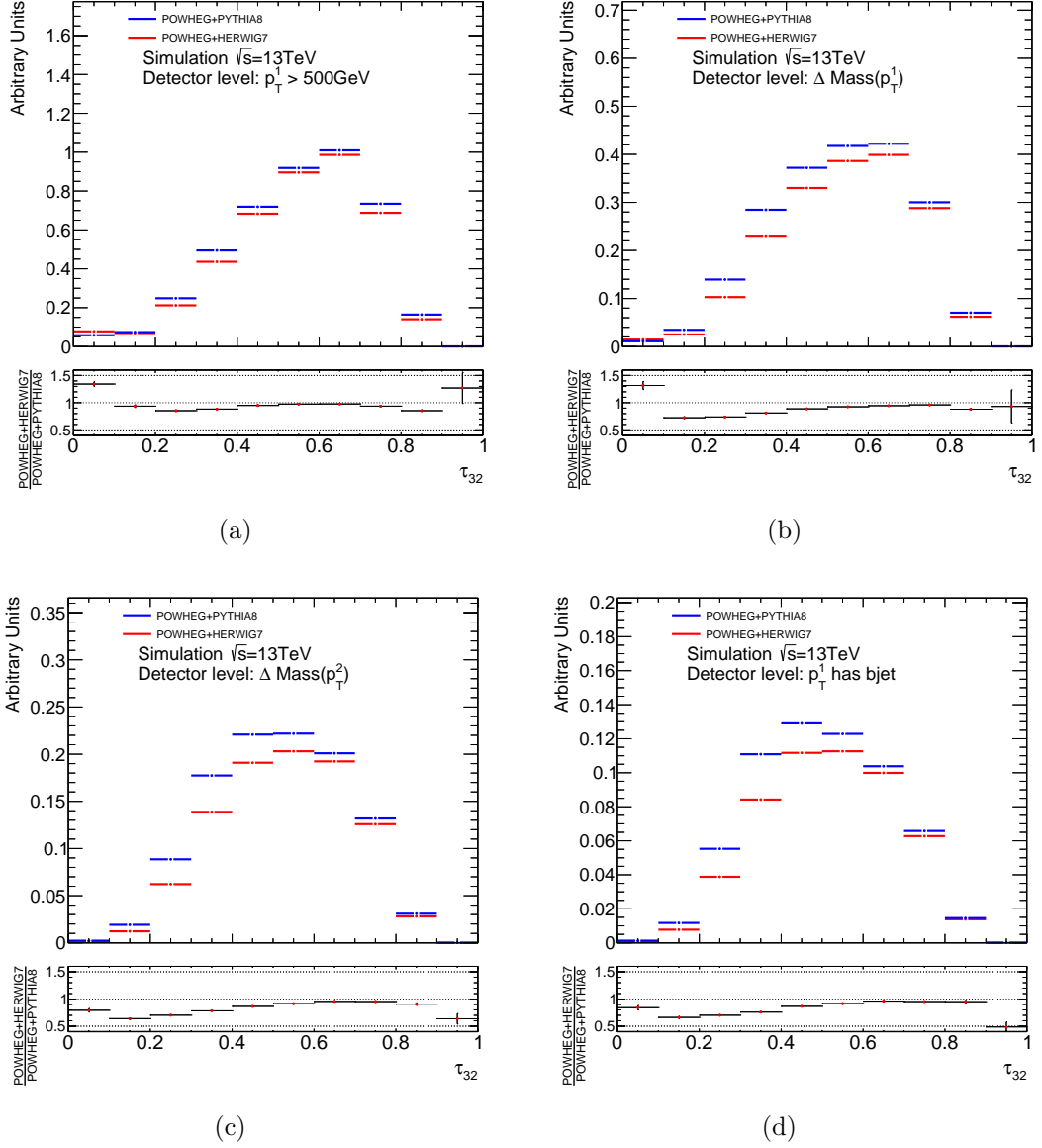
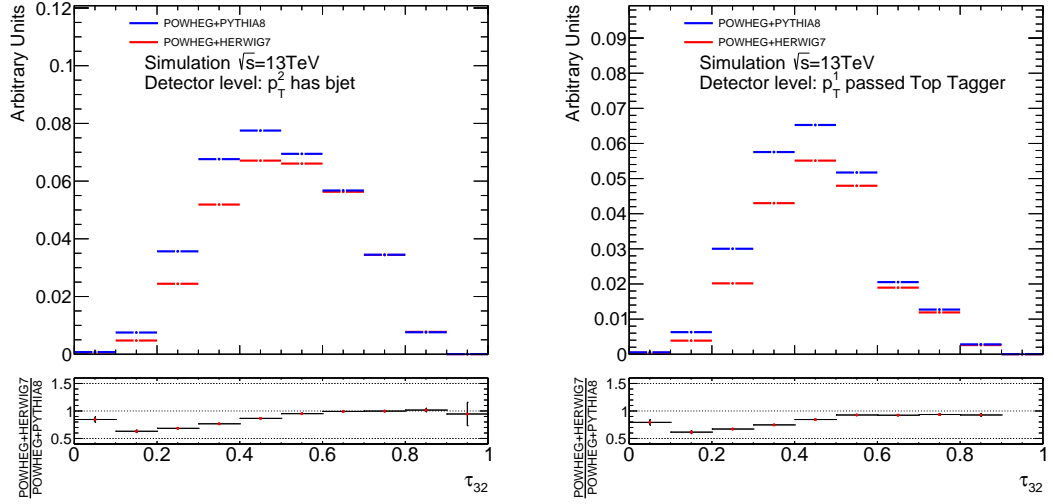
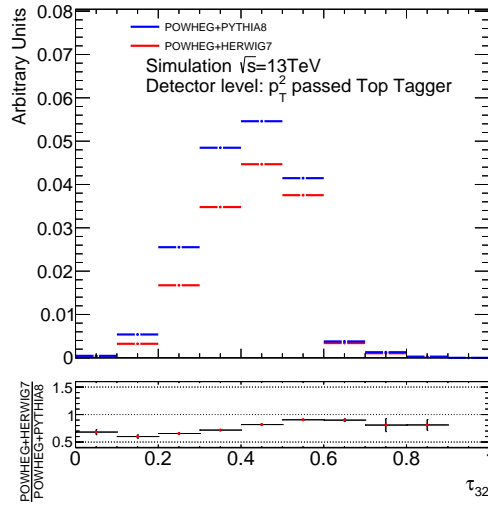


Figure 8.6:  $\tau_{32}$  for each step of event selection at the detector level. (a) after selecting Leading large jets  $p_T > 500\text{ GeV}$ . (b) after requiring the mass of the Leading large jets within  $50\text{ GeV}$  of the top quark mass. (c) after requiring the mass of the 2nd Leading large jets within  $50\text{ GeV}$  of the top quark mass. (d) after requiring  $b$ -tag in the Leading large jet. Cuts are applied sequentially.



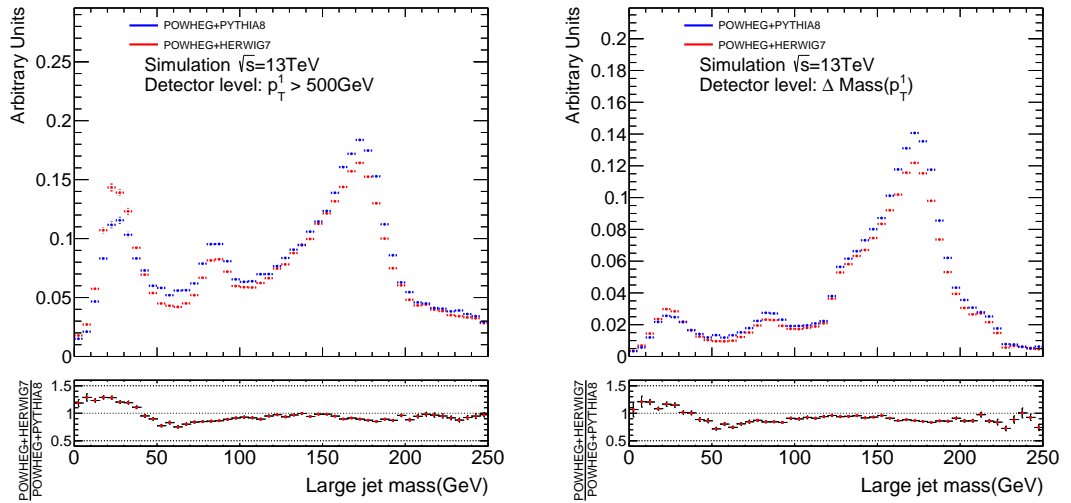
(a)

(b)



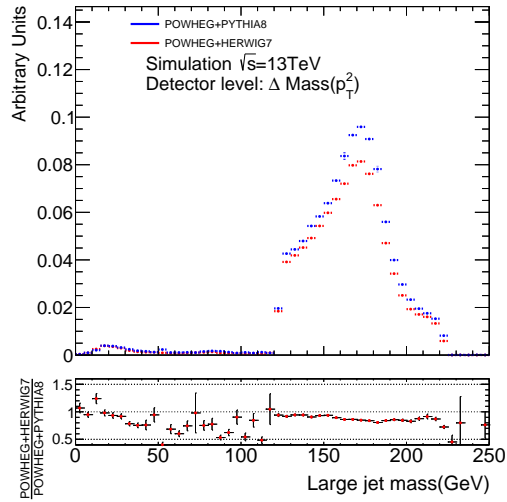
(c)

Figure 8.7:  $\tau_{32}$  for each step of event selection at the detector level (continued) (a) after requiring  $b$ -tag in the 2nd Leading large jet. (b) after requiring Leading large jet to be top-tagged. (c) after requiring 2nd Leading large jet to be top-tagged. Cuts are applied sequentially.



(a)

(b)



(c)

Figure 8.8: The mass distributions before and after mass cut at detector level. (a) after selecting Leading large jets  $p_T > 500$  GeV. (b) after requiring the mass of the Leading large jets within 50 GeV of the top quark mass. (c) after requiring the mass of the 2nd Leading large jets within 50 GeV of the top quark mass.

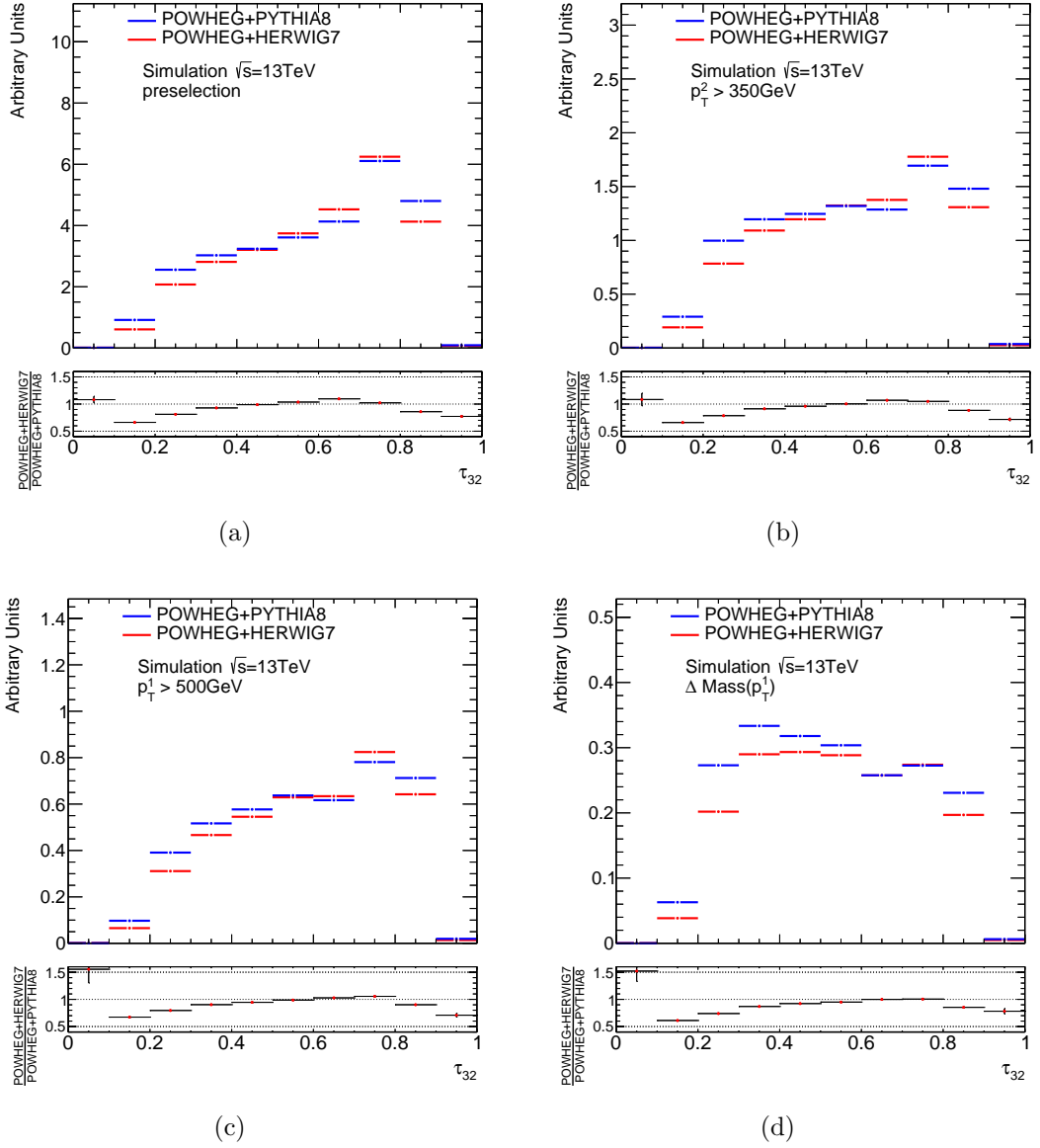
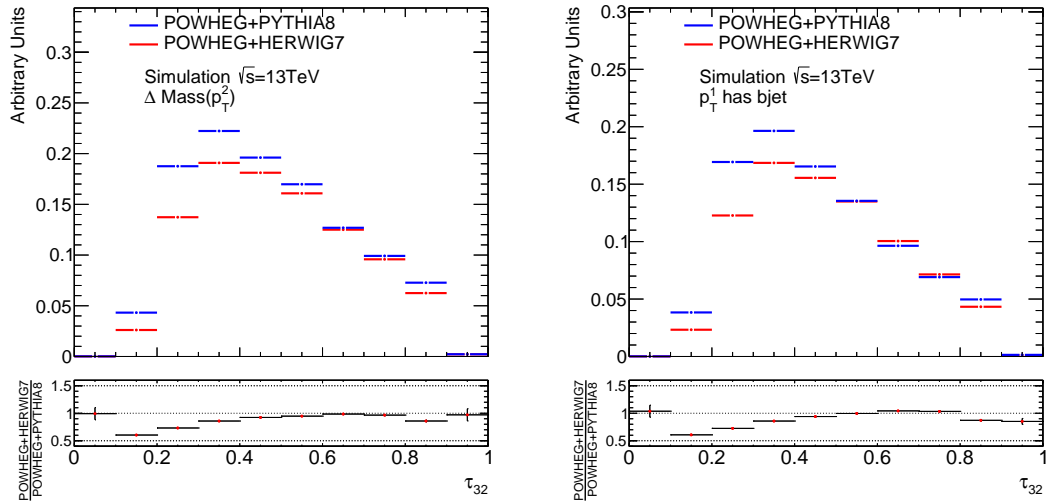
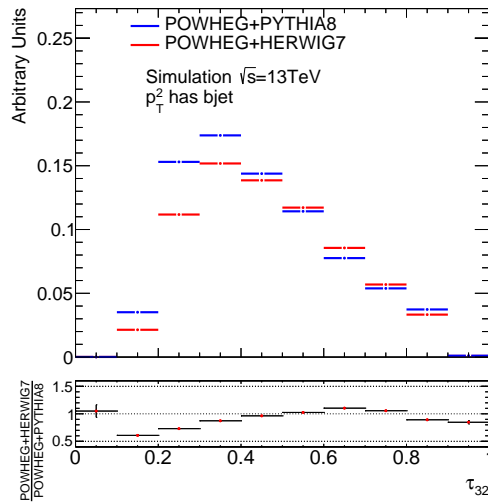


Figure 8.9:  $\tau_{32}$  distribution for each cut step at the particle level. (a) after preselection and trigger. (b) after selecting two large jets  $p_T > 350$  GeV. (c) after selecting Leading large jets  $p_T > 500$  GeV. (d) after requiring the mass of the Leading large jets within 50 GeV of the top quark mass. Cuts are applied sequentially.



(a)

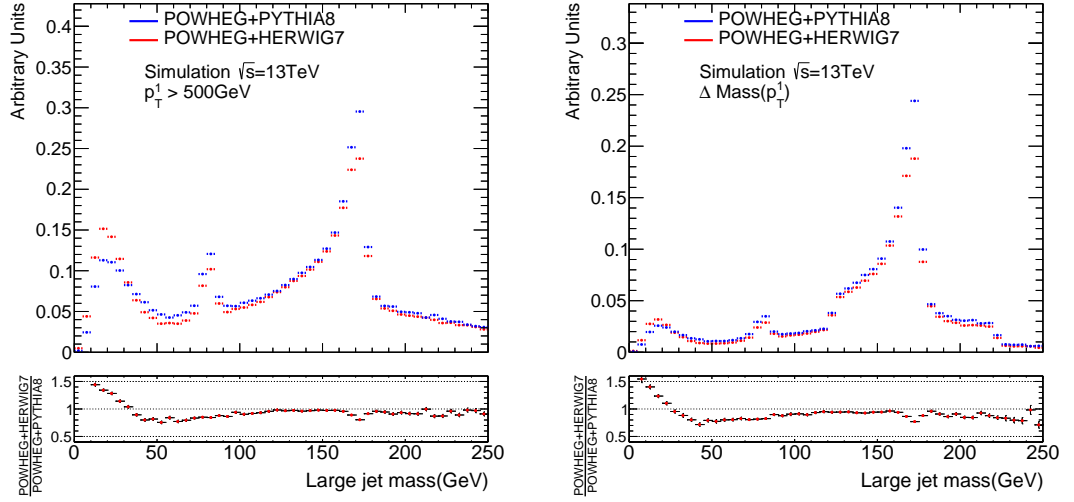
(b)



(c)

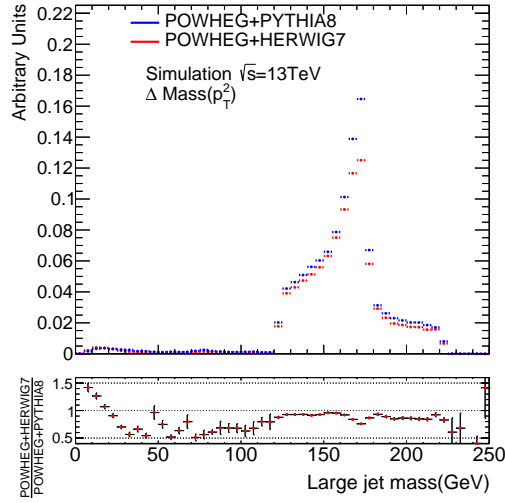
Figure 8.10:  $\tau_{32}$  distribution for each cut step at the particle level (continued). (a) after requiring the mass of the 2nd Leading large jets within 50 GeV of the top quark mass. (b) after requiring  $b$ -tag in the Leading large jet. (c) after requiring  $b$ -tag in the 2nd Leading large jet. Cuts are applied sequentially.

The behaviour of the  $\tau_{32}$  distribution was also investigated in the particle level. Fig. 8.9 and 8.10 shows the  $\tau_{32}$  distributions on the particle level. No significant difference between the two models was found before the mass cut. Similar behavior observed in the detector level that PWG+PY8 is more than PWG+H7 in the range of  $\tau_{32} < 0.6$ , was observed in the particle level in the  $\tau_{32}$  ratio after the mass cuts. The mass distributions at the particle level were also investigated and are shown in Fig. 8.11. After mass cut, the similar tendency that PWG+PY8 is more than PWG+H7 around mass distribution of 173 GeV, was observed in the particle level. These indicate that the observed difference between the two models in the detector



(a)

(b)



(c)

Figure 8.11: before and after mass cut at the particle level. (a) after selecting Leading large jets  $p_T > 500 \text{ GeV}$ . (b) after requiring the mass of the Leading large jets within 50 GeV of the top quark mass. (c) after requiring the mass of the 2nd Leading large jets within 50 GeV of the top quark mass.

level in fact comes from the different particle distributions, i.e. originated from the model difference.

For quantitative understanding, two kinds of values are estimated. One is integrating the cross sections in a mass range of 125 GeV and 220 GeV for detector and particle level after the mass cut. The values are listed in the Tab. 8.4. PWG+H7 showed 12.4% lower event yield than PWG+PY8 at detector level, while the corresponding number on the particle level is 9.1% lower. The other value is integrating the cross section in the  $\tau_{32}$  range of 0 and 0.6. The values are listed in the Tab. 8.5. PWG+H7 showed 19.2% lower than PWG+PY8 in detector level, while 12.9% lower in particle level.

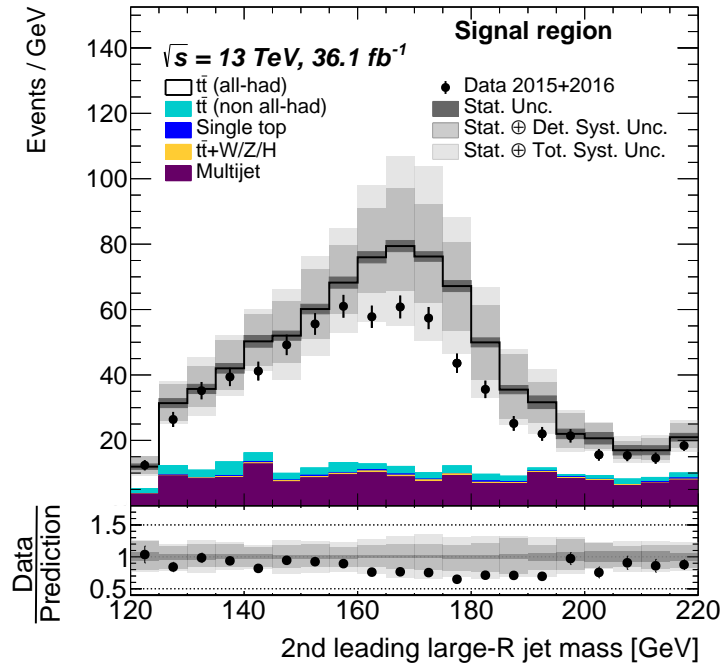
	PWG+H7	PWG+PY8	$1 - \frac{PWG+H7}{PWG+PY8}$
Detector level( $125 < m < 220$ GeV)	0.92 [pb]	1.05 [pb]	12.4%
Particle level( $125 < m < 220$ GeV)	0.70 [pb]	0.77 [pb]	9.1%

Table 8.4: Comparison of integrated mass distribution around the top mass with PWG+H7 and PWG+PY8 in the detector and particle levels

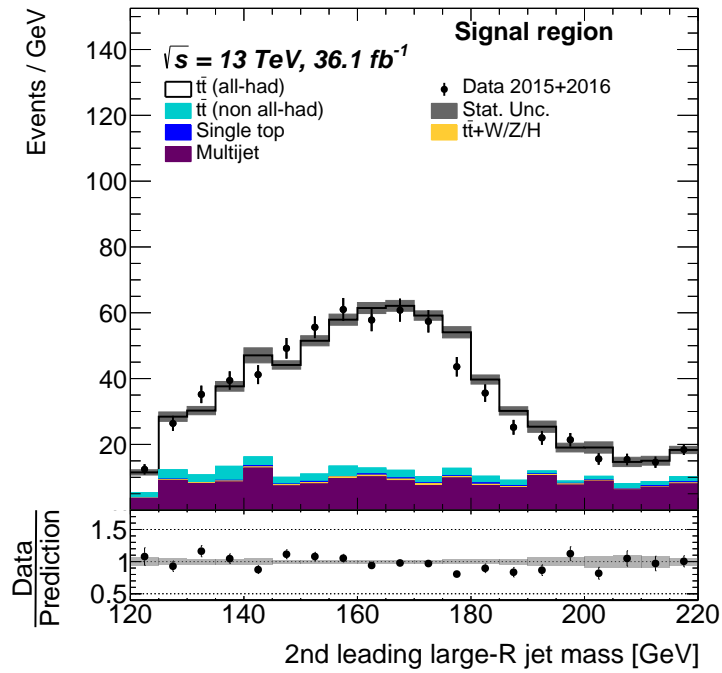
	PWG+H7	PWG+PY8	$1 - \frac{PWG+H7}{PWG+PY8}$
Detector level( $\tau_{32} < 0.6$ )	0.21[pb]	0.26[pb]	19.2%
Particle level( $\tau_{32} < 0.6$ )	0.54[pb]	0.62[pb]	12.9%

Table 8.5: Comparison of integrating  $\tau_{32}$  distributed from 0 to 0.6 with PWG+H7 and PWG+PY8 in the detector and particle levels

From the above values, similar behaviors appear in both detector and particle levels, although the difference is less pronounced in the particle level than the detector level. This means that the difference of detector with different MC signal samples is not completely from detector effect, but predominantly from particle level effect. Figure 8.12 show the 2nd Leading Large-R jet mass distributions at detector level, where PWG+PY8 and PWG+H7 as signal prediction is good agreement with data, but PWG+H7 tends to be closer to data.



(a)



(b)

Figure 8.12: 2nd Leading Large-R jet mass. (a): signal sample using PWG+PY8, (b): signal sample using PWG+H7.

# Chapter 9

## Result and discussion

This chapter presents the result of  $t\bar{t}$  after unfolding, and the qualitative and quantitative comparisons between data and several theoretical predictions.

### 9.1 Fiducial phase-space inclusive cross section

The inclusive cross section and its uncertainty integrated over the fiducial phase-space is calculated by using unfolding technique in the previous chapter and merging all events into a single bin. The measured cross section is:

$$\sigma_{\text{fid}} = 292 \pm 7 \text{ (stat.)} \pm 76 \text{ (syst.) fb.}$$

The systematic uncertainties in this measurement, which are dominated by tagging and modelling uncertainties, are summarized in Tab. 8.3. The result of fiducial inclusive cross-section measurement with several MC predictions is shown in Fig. 9.1. The measured value is below for all the predictions although they are within the uncertainty of the measurements and theoretical prediction. The PWG+H7 is the closest to the measured value and the farthest is aMC@NLO+PYTHIA8 (hereafter aMC@NLO+PY8). The PWG+PY8 as well as SHERPA2.2.1 (hereafter SHERPA) predicts in between the above two predictions.

The inclusive cross section with nominal prediction (PWG+PY8) is  $384 \pm 36$  fb, about 30% larger than the data. Similar result was observed in lepton+jets channel by two experiments, CMS [59] and ATLAS [59]. The results of the differential cross section as a function of  $p_T$  are presented in Fig. 9.2(a) and 9.2(b). For these two measurements, in the range of  $p_T > 400$  GeV region for PWG+PY8, the result of lepton+jets in the two experiments both show around 20% larger cross sections than the data. They indicate that this measurement is consistent with the above mentioned measurements in term of the PWG+PY8 prediction, i.e. beyond the data in high  $p_T$  region.

The fiducial inclusive cross-section reflects if a prediction is in agreement with the data on average. In order to find where the prediction is in agreement or disagreement with data in detail, the results of differential cross sections are shown in

next section.

## 9.2 Fiducial phase-space differential cross sections

The results of fiducial differential cross sections as a function of several variables are presented both as absolute and normalized differential cross sections.

**Absolute differential cross sections ( $d\sigma^{\text{fid}}/d\mathbf{X}^i$ )** The differential cross sections for observables related to Large-R jets, i.e. the top quark momentum, are shown in Fig. 9.3. The four MC predictions are in agreement with data for transverse momentum ( $p_T^{t,1}$  and  $p_T^{t,2}$ ) within the total uncertainty. For the variables related to the rapidity of the Large-R jets, the four MC predictions show good agreement with data in behaviour that the cross sections drop with the increase of rapidity ( $|y|$ ).

The predictions tend to overestimate the data. This indicates the consistency of the result between inclusive and differential cross section where the predictions tend to be beyond the data. Furthermore, from the differential cross section distributions, the predictions overestimating cross sections mainly come from in the range of  $y$  from 0 to 1, where all predictions tend to be beyond the data.

The results related to kinematics of the  $t\bar{t}$  system are presented in Fig. 9.4. The four MC predictions show good agreement with the data in the invariant mass of  $t\bar{t}$  reconstructed from two Leading Large-R jets. The mass extends up to around 2 TeV. For the  $t\bar{t}$  rapidity  $|y^{t\bar{t}}|$  as shown Fig 9.4(b), the  $t\bar{t}$  are produced mostly from the range of rapidity below 1.0. In this range, PWG+H7 tend to be closer to data than other three MC predictions. However, in the rapidity above 1.0, the four predictions are in agreement with data within uncertainties. The  $p_T^{t\bar{t}}$  describes the imbalance in the transverse momentum space between the two Leading Large-R jets used for the  $t\bar{t}$  reconstruction. As the transverse momentum of Leading Large-R jet approaches the 2nd Leading Large-R jet, events with two approximately transversely balanced Large-R jet mostly distribute with the transverse momentum of  $t\bar{t}$  close to zero as shown in the Fig. 9.4(c). A similar variable  $\Delta\phi_{t\bar{t}}$  is described in Fig. 7.1, which is sensitive to the emission of radiation associated with the production of  $t\bar{t}$ . The production of  $t\bar{t}$  is back-to-back, i.e. the distribution has a sharp peak at  $\Delta\phi_{t\bar{t}} = \pi$ , as seen in the Fig. 9.4(d). The aMC@NLO+PY8 shows poor agreement with data, where it tends to predict more radiation as manifested in  $p_T^{t\bar{t}}$  in above 300 GeV and  $\Delta\phi_{t\bar{t}}$  below 2.5.

**Normalized differential cross sections ( $1/\sigma^{\text{fid}} \cdot d\sigma^{\text{fid}}/d\mathbf{X}^i$ )** For better sensitivity in shape comparison, normalized cross sections are also presented. The unfolded normalized differential cross sections are obtained from absolute differential cross sections normalized to the total cross-section for the fiducial phase-space. The four MC predictions show good agreement with data with the transverse momentum of Leading and 2nd Large-R jet, and rapidity of the 2nd Leading Large-R jet as seen in Fig. 9.5(a), 9.5(b) and 9.5(d). However, for the rapidity of the Leading

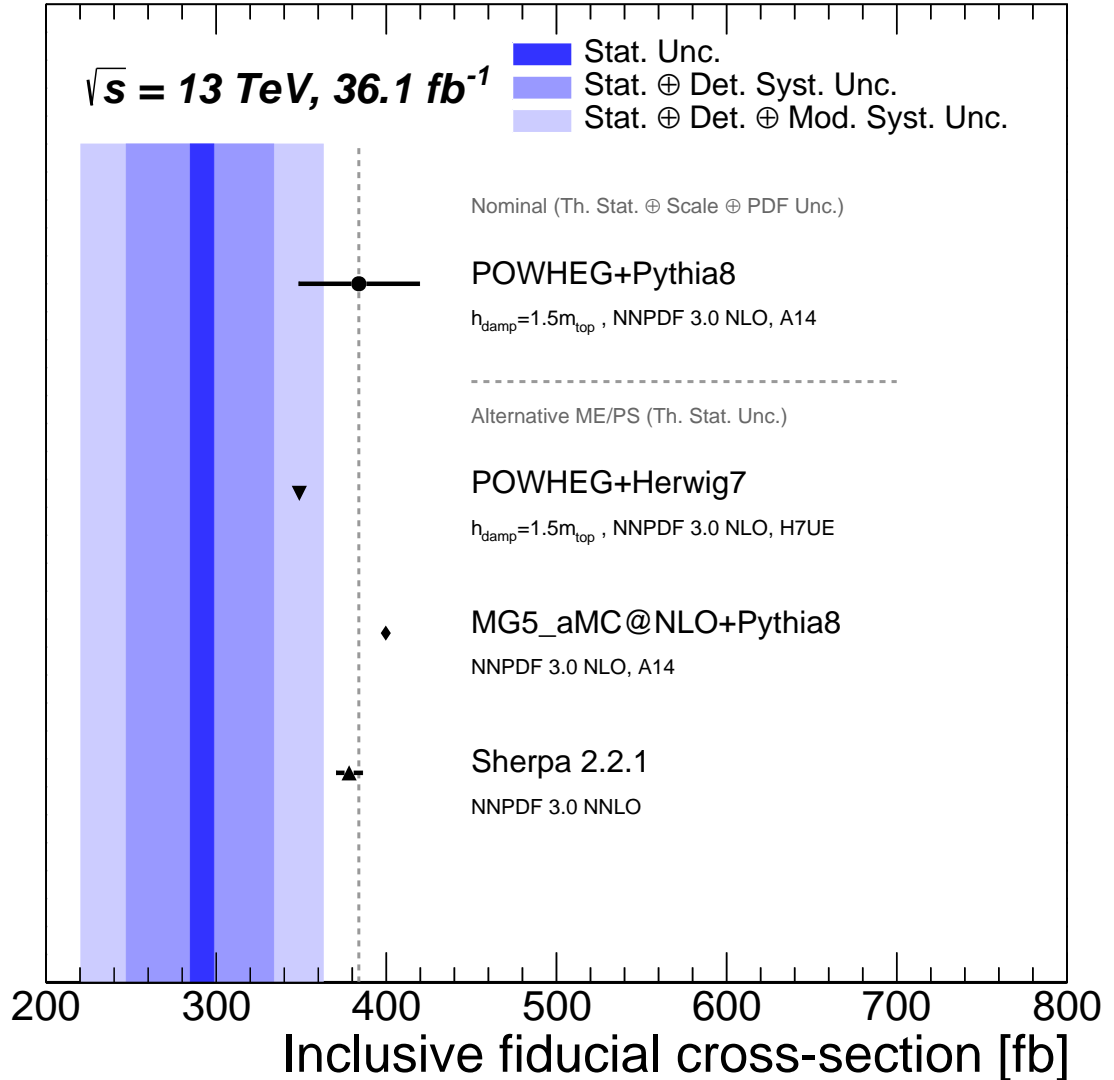
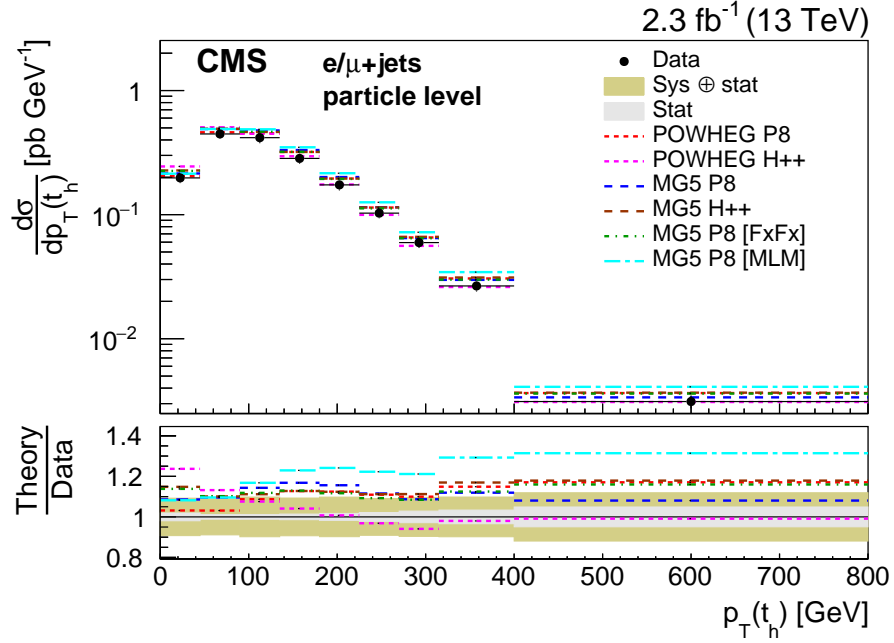
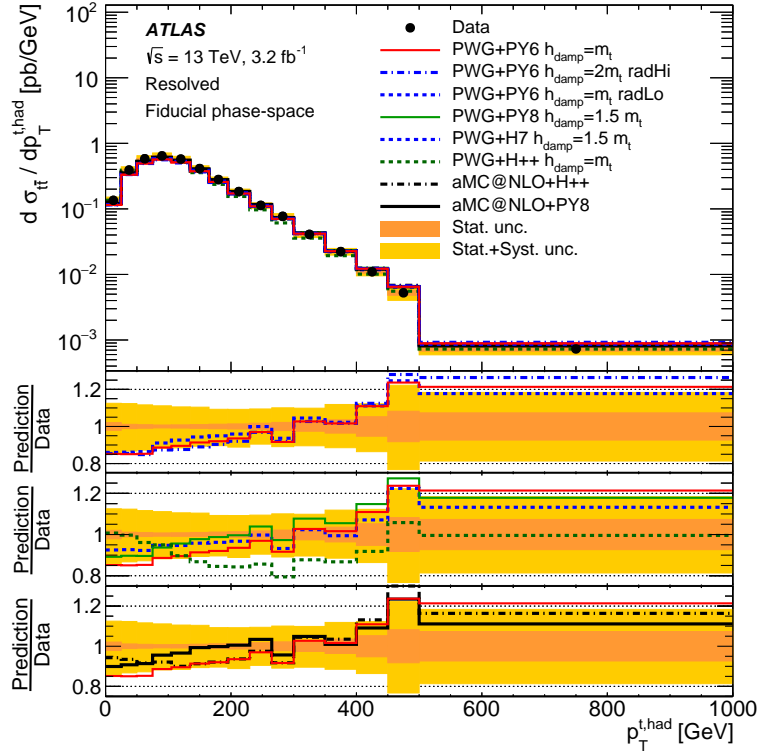


Figure 9.1: Fiducial inclusive phase-space cross-section. The deep blue bands indicate only the statistical uncertainty on the measurement, the medium blue bands show the statistical and detector uncertainties and the lightest blue bands indicate the statistical, detector and modelling uncertainties on the measurement. The POWHEG+PYTHIA8 event generator is used as the nominal prediction to correct for detector effects. The uncertainty associated with the POWHEG+PYTHIA8 signal model includes the statistical and theoretical uncertainties. Other predictions show only the statistical uncertainty of the MC sample.



(a)

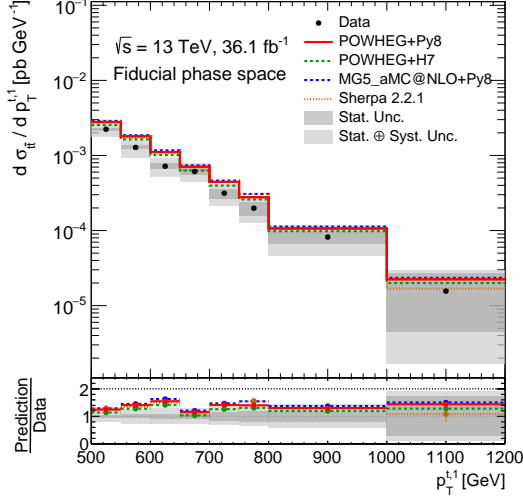


(b)

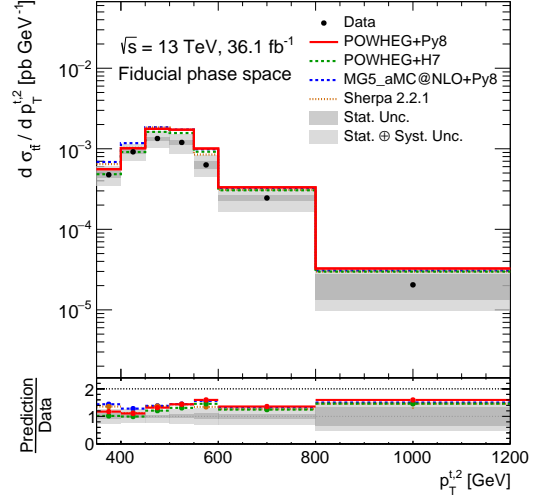
Figure 9.2: Absolute fiducial phase-space differential cross sections as a function of transverse momentum of top quark, (a) CMS lepton+jets channel@13TeV [59]; (b) ATLAS lepton+jets@13TeV [60].

Large-R jet, a similar behaviour, that the ratio between prediction and data drops in the range from 1.0 to 2.0, is observed in the four MC predictions.

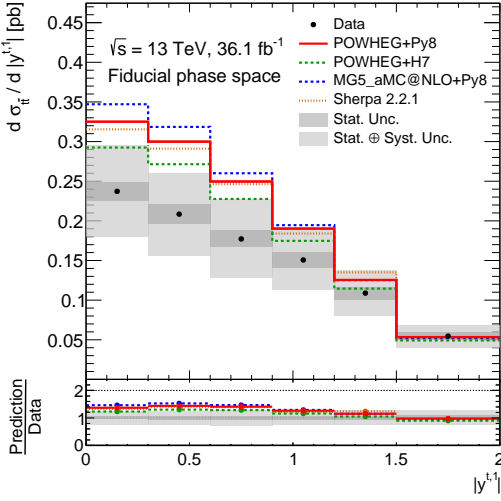
As for the  $t\bar{t}$  system, the  $t\bar{t}$  invariant mass (Fig. 9.6(a)) shows that the four predictions are in good agreement with the data. For the variables related to radiation associated with the production of  $t\bar{t}$ ,  $p_T^{t\bar{t}}$  and  $\Delta\phi_{t\bar{t}}$ , the aMC@NLO+PY8 prediction poorer agreement with data than other three MC predictions as seen in Fig. 9.6(b) and 9.6(d). For the rapidity of  $t\bar{t}$ , the four predictions show good agreement with data.



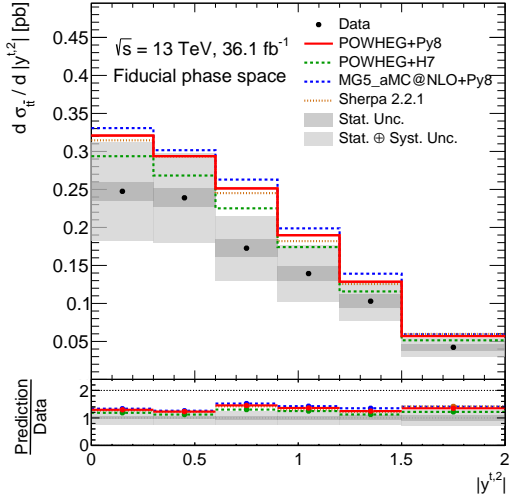
(a)



(b)



(c)



(d)

Figure 9.3: Absolute fiducial phase-space differential cross sections as a function of (a) transverse momentum of the Leading top-quark jet, (b) transverse momentum of the 2nd Leading top-quark jet, (c) absolute value of the rapidity of the Leading top-quark jet and (d) absolute value of the rapidity of the 2nd Leading top-quark jet. The gray bands indicate the total uncertainty in the data in each bin. The vertical bars in the ratio histograms indicate the statistical uncertainties on the theoretical models.

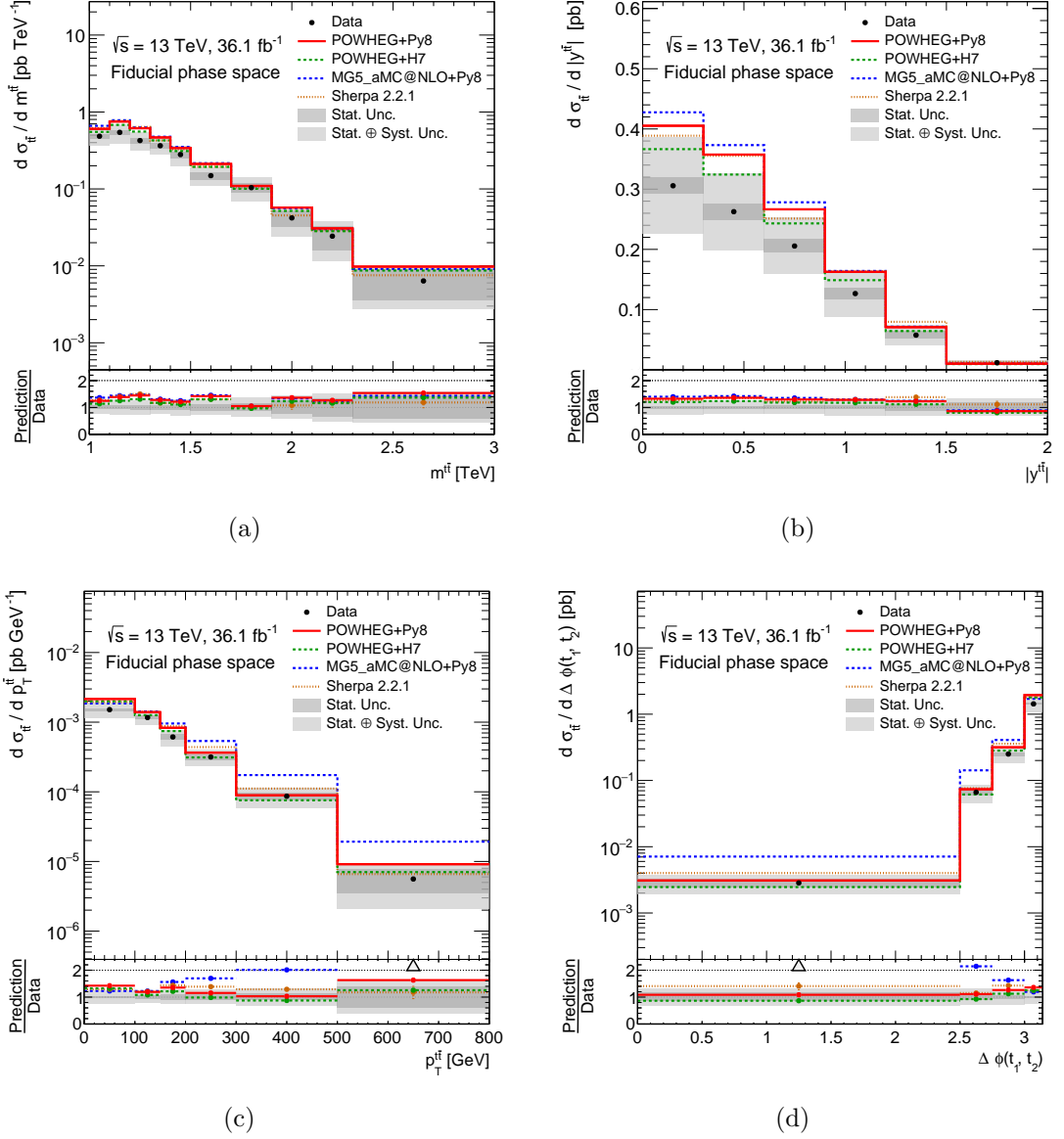


Figure 9.4: Absolute fiducial phase-space differential cross sections as a function of (a) invariant mass and (b) absolute value of the rapidity of the  $t\bar{t}$  system. (c) transverse momentum, (d) the azimuthal angle between the two top-quark jets  $\Delta\phi_{t\bar{t}}$ . The gray bands indicate the total uncertainty in the data in each bin. The vertical bars in the ratio histograms indicate the statistical uncertainties on the theoretical models.

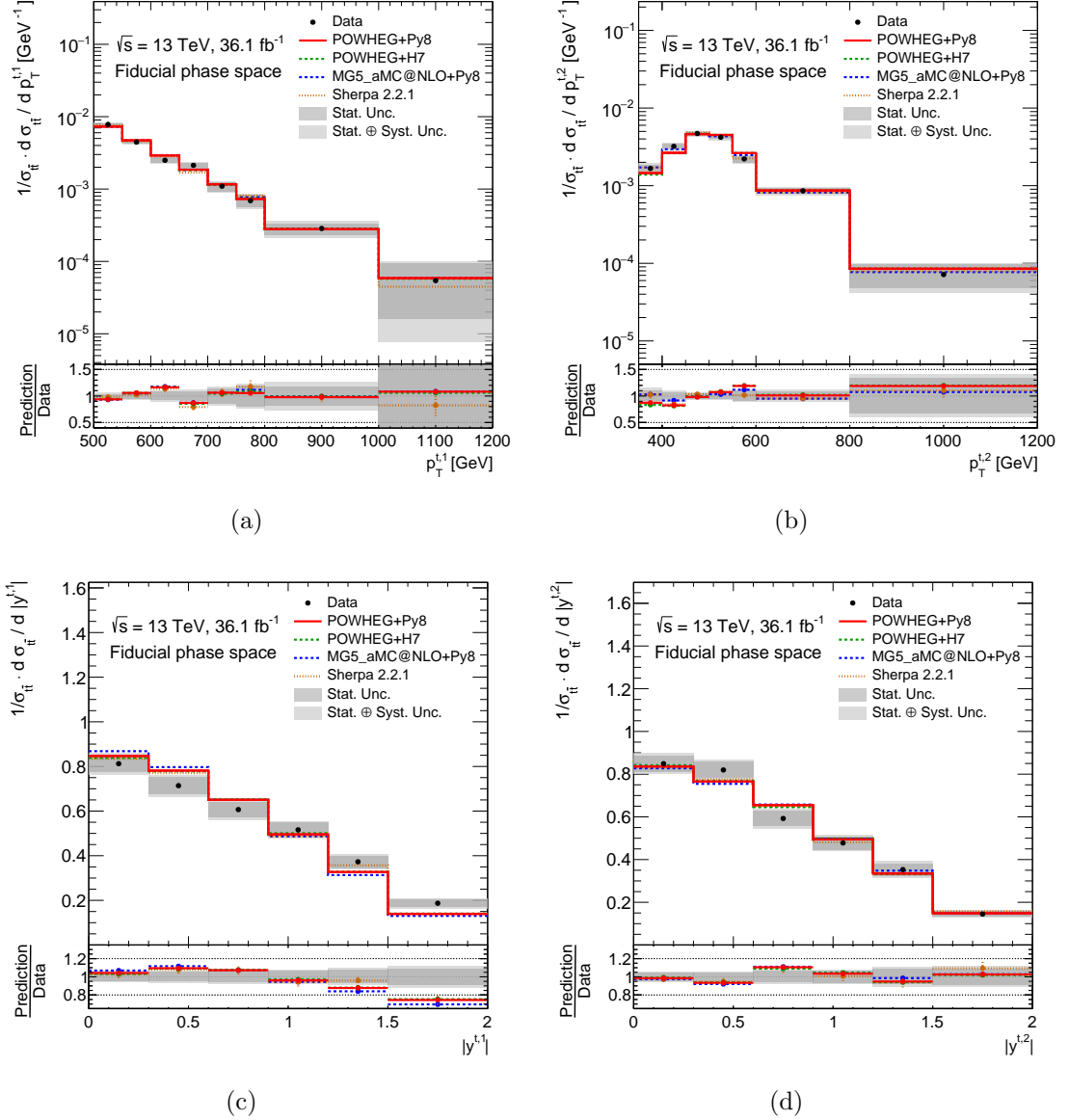


Figure 9.5: Normalized fiducial phase-space differential cross sections as a function of (a) transverse momentum of the Leading top-quark jet, (b) transverse momentum of the 2nd Leading top-quark jet, (c) absolute value of the rapidity of the Leading top-quark jet and (d) absolute value of the rapidity of the 2nd Leading top-quark jet. The gray bands indicate the total uncertainty in the data in each bin. The vertical bars in the ratio histograms indicate the statistical uncertainties on the theoretical models.

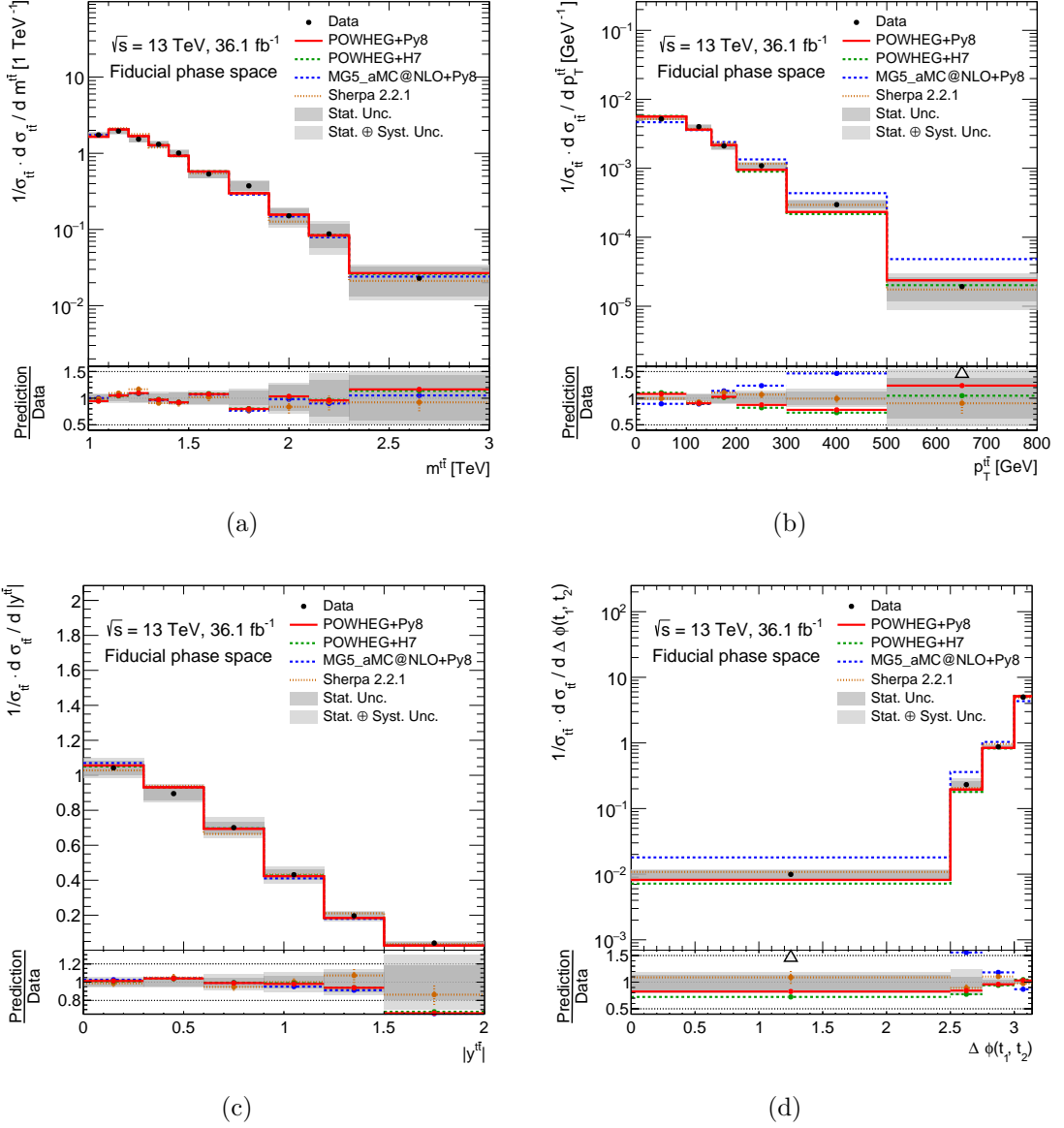


Figure 9.6: Normalized fiducial phase-space differential cross sections as a function of (a) invariant mass and (b) transverse momentum, (c) absolute value of the rapidity of the  $t\bar{t}$  system. (d) the azimuthal angle between the two top-quark jets  $\Delta\phi_{t\bar{t}}$ . The gray bands indicate the total uncertainty in the data in each bin. The vertical bars in the ratio histograms indicate the statistical uncertainties on the theoretical models.

### 9.3 Quantitative comparisons with SM predictions through $\chi^2$ estimator

Qualitative comparisons with SM predictions are presented in the previous section. In this section, quantitative comparison between the measured differential cross sections and four MC predictions is given by calculating  $\chi^2$  values and the corresponding  $p$ -values (probabilities that the  $\chi^2$  is less than or equal to the observed value) between data and models.

The formula to calculate the  $\chi^2$  is in Eq. 9.1 for differential cross sections.

$$\chi^2 = V_{N_b}^T \cdot \text{Cov}_{N_b}^{-1} \cdot V_{N_b}, \quad (9.1)$$

where  $V_{N_b}$  is a matrix containing  $N_b$  elements due to  $N_b$  bin in the distribution. Each element expresses the differences between measured differential cross section value and prediction for each bin.  $\text{Cov}_{N_b}^{-1}$  is the inverse of the covariance matrix. The covariance matrix is obtained from one calculated in Chapter 8.

For the case of normalized differential cross section, since the normalization constraint lowers the NDF (Number of Degrees of Freedom) to one less than the rank of the  $N_b \times N_b$  covariance matrix, the  $\chi^2$  for the normalized differential cross sections is expressed as below.

$$\chi^2 = V_{N_b-1}^T \cdot \text{Cov}_{N_b-1}^{-1} \cdot V_{N_b-1}, \quad (9.2)$$

The Tables 9.1 and 9.2 provide the  $\chi^2$  and  $p$ -values resulting from the comparisons of the absolute and normalized differential cross sections with predictions for the results in the fiducial phase-space.

**Discussion** Ideally, the prediction is in better agreement with the measurement as the  $\chi^2$  value gets closer to NDF. Correspondingly, the high  $p$ -value presents the prediction is closer to the measurement. Below the  $\chi^2$  value of differential cross sections in each variable is discussed.

- Leading Large-R jet  $p_T$  ( $p_T^{t1}$ ): the  $\chi^2$  is around 8.0 for four MC predictions. This indicates the four predictions are all in good agreement with the data. This result for both absolute and normalized differential cross sections are consistent with qualitative observation for Fig. 9.3(a) and 9.5(a).
- Leading Large-R jet rapidity ( $y^{t1}$ ): the  $\chi^2$  values show much larger than 6.0 (NDF value) as well as the  $p$ -values show lower than 0.1. This indicates the four MC predictions give only fair description on data for the absolute differential cross section. In particular, aMC@aNLO+PY8 gives the  $\chi^2$  value of 27.3 with the  $p$ -value which less than 0.01. For normalized differential cross sections, the  $\chi^2$  is around 6.0, close to the NDF value except aMC@NLO+PY8 which has 12.2. As Fig. 9.5(c) has shown, the higher  $\chi^2$  is due to the drop of rapidity from 1.0 to 2.0.

- 2nd Leading Large-R jet  $p_T$  ( $p_T^{t2}$ ) and rapidity ( $y^{t2}$ ): the four MC predictions have  $p$ -value at least above 0.15 for absolute and normalized differential cross sections. It is consistent with the qualitative conclusion based on the ratios in Fig. 9.5(b) and 9.5(d).
- $t\bar{t}$  invariant mass ( $m^{t\bar{t}}$ ): In previous section it is stated that the four MC predictions are in good agreement with data by Fig. 9.4(a) and 9.6(a). The  $p$ -values for four MC predictions are at least above 0.13, reflecting the qualitative conclusion as seen in with these figures.
- $t\bar{t}$  rapidity ( $y^{t\bar{t}}$ ): The four MC predictions have high  $p$ -values. Within the uncertainties, these predictions are in agreement with the data.
- $t\bar{t}$   $p_T$  ( $p_T^{t\bar{t}}$ ) and  $\Delta\phi_{t\bar{t}}$ : the aMC@NLO+PY8 shows higher  $\chi^2$  and very low  $p$ -value than other three MC predictions, which is consistent with the behaviour of the distribution as Fig. 9.4(c), 9.6(b), 9.4(d) and 9.6(d).

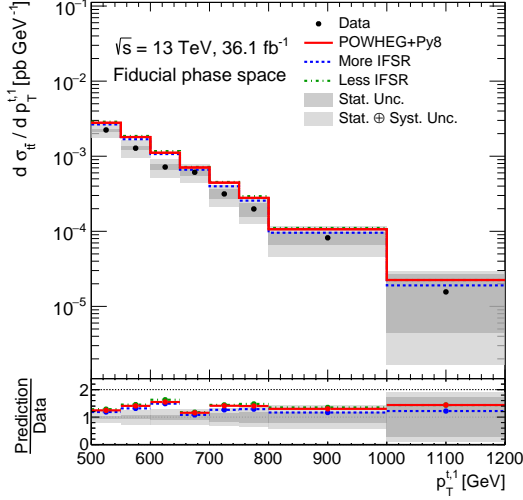
Observable	PWG+PY8		aMC@NLO+PY8		PWG+H7		SHERPA	
	$\chi^2/\text{NDF}$	$p$ -value						
$p_T^{t,1}$	7.6/8	0.48	8.9/8	0.35	6.1/8	0.63	9.8/8	0.28
$ y^{t,1} $	16.7/6	0.01	27.3/6	<0.01	12.6/6	0.05	12.1/6	0.06
$p_T^{t,2}$	10.7/7	0.15	6.6/7	0.47	10.4/7	0.17	8.5/7	0.29
$ y^{t,2} $	5.7/6	0.45	7.8/6	0.25	3.5/6	0.74	5.3/6	0.51
$m^{t\bar{t}}$	8.6/10	0.57	11.9/10	0.29	5.6/10	0.85	15.0/10	0.13
$p_T^{t\bar{t}}$	8.8/6	0.19	26.8/6	<0.01	10.2/6	0.12	3.4/6	0.76
$ y^{t\bar{t}} $	5.6/6	0.47	8.2/6	0.23	3.7/6	0.72	3.4/6	0.76
$\Delta\phi^{t\bar{t}}$	5.1/4	0.28	49.2/4	<0.01	6.2/4	0.19	3.6/4	0.47

Table 9.1: Comparison between the measured absolute differential cross sections and the predictions from several MC generators. For each variable and prediction, a  $\chi^2$  and a  $p$ -value are calculated using the covariance matrix in Chapter 8, which includes all sources of uncertainty. The number of degrees of freedom (NDF) is equal to  $N_b$ , where  $N_b$  is the number of bins in the distribution.

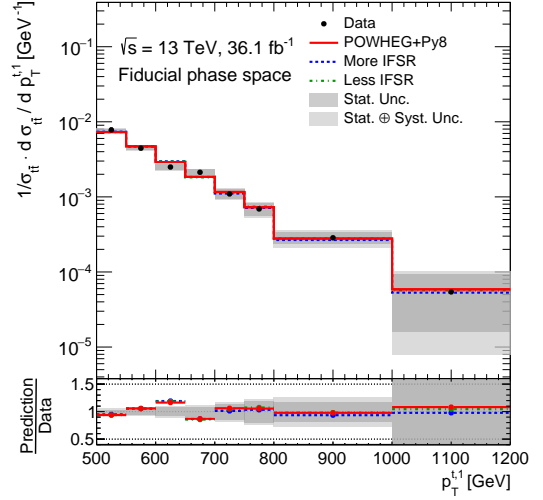
Observable	PWG+PY8		AMC@NLO+PY8		PWG+H7		SHERPA	
	$\chi^2/\text{NDF}$	$p$ -value						
$p_{\text{T}}^{t,1}$	7.7/7	0.36	8.2/7	0.32	8.0/7	0.33	9.3/7	0.23
$ y^{t,1} $	7.5/5	0.18	12.2/5	0.03	6.8/5	0.24	4.0/5	0.55
$p_{\text{T}}^{t,2}$	8.6/6	0.20	2.6/6	0.86	9.9/6	0.13	5.0/6	0.55
$ y^{t,2} $	3.7/5	0.59	4.6/5	0.46	3.1/5	0.68	2.9/5	0.72
$m^{t\bar{t}}$	4.5/9	0.88	4.7/9	0.86	4.0/9	0.91	10.0/9	0.35
$p_{\text{T}}^{t\bar{t}}$	7.8/5	0.17	20.9/5	<0.01	12.6/5	0.03	1.9/5	0.87
$ y^{t\bar{t}} $	1.1/5	0.95	2.2/5	0.83	0.9/5	0.97	1.7/5	0.89
$\Delta\phi^{t\bar{t}}$	0.9/3	0.84	16.3/3	<0.01	2.0/3	0.58	3.4/3	0.33

Table 9.2: Comparison between the measured normalized differential cross sections and the predictions from several SM generators. For each variable and prediction, a  $\chi^2$  and a  $p$ -value are calculated using the covariance matrix described in the Chapter 8, which includes all sources of uncertainty. The number of degrees of freedom (NDF) is equal to  $N_{\text{b}} - 1$ , where  $N_{\text{b}}$  is the number of bins in the distribution.

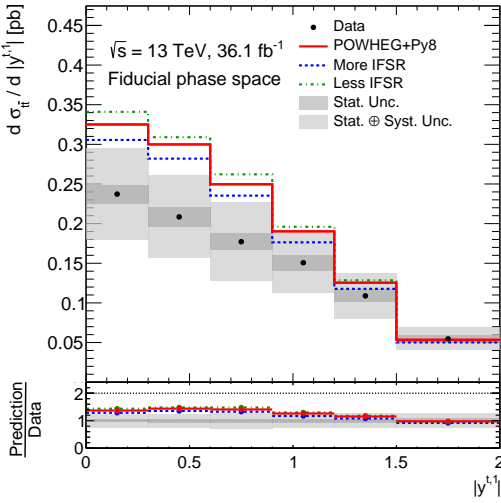
In the variables related to the QCD radiation associated with the production of  $t\bar{t}$ , the aMC@NLO+PY8 show poor agreement with data than other three MC predictions. The difference between aMC@NLO+PY8 and nominal sample (PWG+PY8) is from the ME calculations to determine more or less ISR and FSR. In order to see the effect of ISR and FSR, the measured cross sections are also compared to alternative samples, in which the parameters  $\mu_f$ ,  $\mu_R$  and `hdamp` are modified within allowed range of the ATLAS measurements of  $t\bar{t}$ +jets cross sections [61]. They are shown in Fig. 9.7 and 9.8. The “more ISR and FSR” sample is closer to data than “less ISR and FSR”. It indicates that more radiation of initial and final states give direction of the model predictions’ improvement.



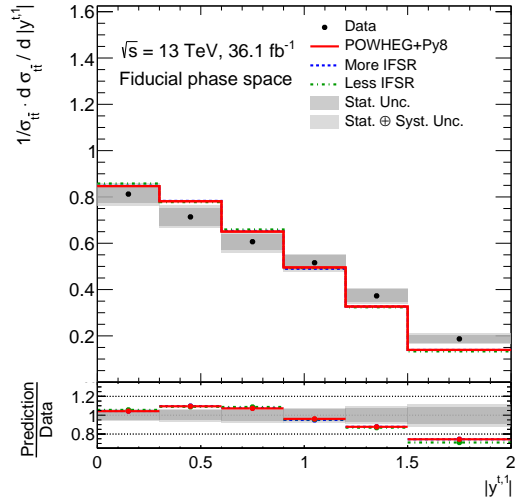
(a)



(b)



(c)



(d)

Figure 9.7: IFSR with fiducial phase-space differential cross sections as a function of (a) transverse momentum of Leading Large-R jet, absolute differential cross section, (b) transverse momentum of Leading Large-R jet, normalized differential cross section, (c) rapidity of Leading Large-R jet, absolute differential cross section, (d) rapidity of Leading Large-R jet, normalized differential cross section, The gray bands indicate the total uncertainty in the data in each bin. The vertical bars in the ratio histograms indicate the statistical uncertainties on the theoretical models.

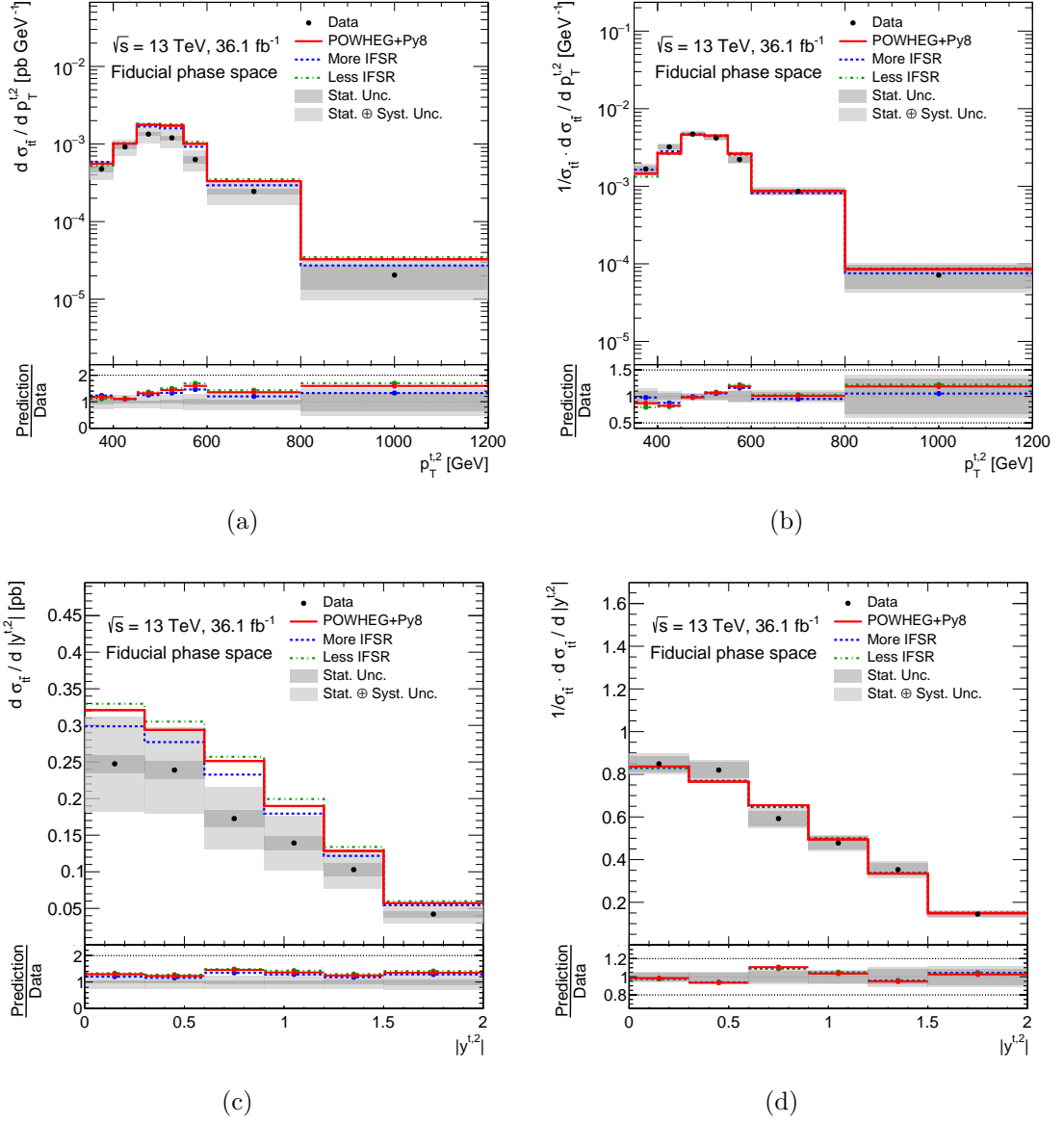
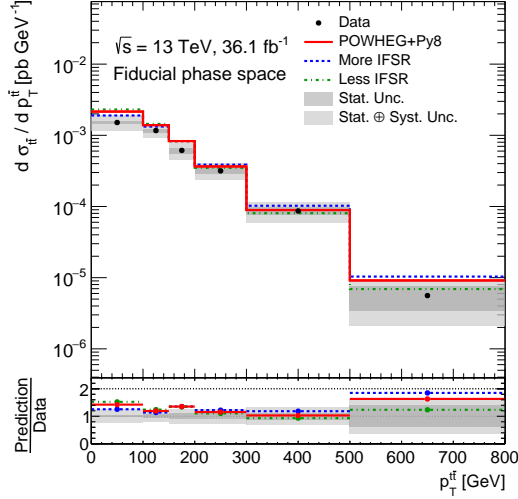
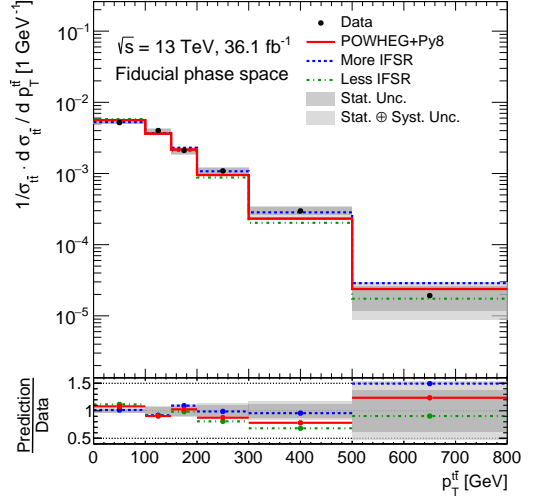


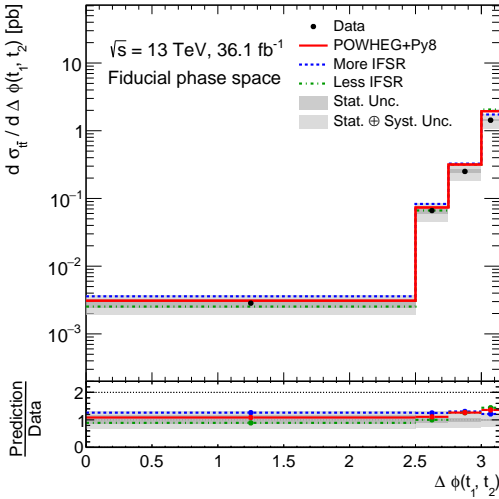
Figure 9.8: IFSR with fiducial phase-space differential cross sections as a function of (a) transverse momentum of 2nd Leading Large-R jet, absolute differential cross section, (b) transverse momentum of 2nd Leading Large-R jet, normalized differential cross section, (c) rapidity of 2nd Leading Large-R jet, absolute differential cross section, (d) rapidity of 2nd Leading Large-R jet, normalized differential cross section, The gray bands indicate the total uncertainty in the data in each bin. The vertical bars in the ratio histograms indicate the statistical uncertainties on the theoretical models.



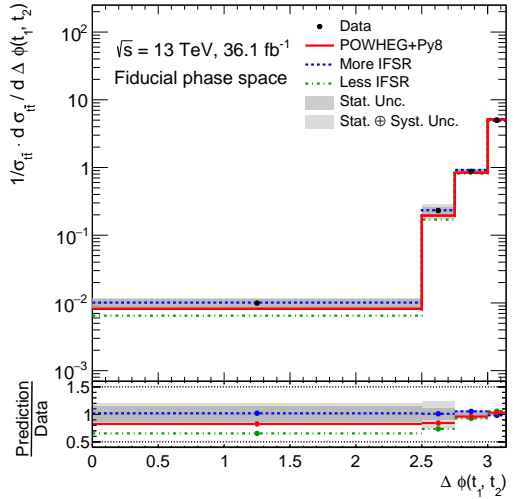
(a)



(b)



(c)



(d)

Figure 9.9: IFSR with fiducial phase-space differential cross sections as a function of (a) transverse momentum of  $t\bar{t}$  absolute differential cross section, (b) transverse momentum of  $t\bar{t}$  normalized differential cross section, (c) azimuthal angle of Leading Large-R jet and 2nd Leading Large-R jet, absolute differential cross section, (d) azimuthal angle of Leading Large-R jet and 2nd Leading Large-R jet, normalized differential cross section, The gray bands indicate the total uncertainty in the data in each bin. The vertical bars in the ratio histograms indicate the statistical uncertainties on the theoretical models.

# Chapter 10

## Conclusion

This dissertation presented measurement of the top pair production differential cross sections. The study has been carried out in the all-hadronic decay process, in which the both of top quarks decay into jets in the final states. The measurement is based on ATLAS experiment data from 13 TeV  $pp$  collisions at the LHC taken in 2015 and 2016. The data sample corresponds to  $36.1 \text{ fb}^{-1}$ . With the increase of collision energy and luminosity, more top quarks with high momentum are collected. The decay products from the top quark of high momentum are observed in single large radius (Large-R) jet due to boost. The kinematics of the top quark and the  $t\bar{t}$  system are reconstructed from the momentum of the Large-R jets.

The events were required with the momentum of Leading Large-R jet  $p_T > 500 \text{ GeV}$  and 2nd Leading Large-R jet  $p_T > 350 \text{ GeV}$ . The two Large-R jets were to pass the top tagging using the jet mass and the subjettiness ratio  $\tau_{32}$ . To reduce the background, at least a  $b$ -jets passing with an associated  $b$ -tagged hadron was required to be inside each Large-R jet. The multijet background as dominant background was estimated using data-driven method. After these selections, the ratio (S/N) of  $t\bar{t}$  signal to background is about 3 to 1.

In order to measure the  $t\bar{t}$  cross sections in particle level, The fiducial phase space is defined using the similar requirements to detector level selections to avoid large extrapolations relying on modelling in generators. The inclusive cross section for  $t\bar{t}$  production in the fiducial phase space is

$$\sigma_{\text{fid}} = 292 \pm 7 \text{ (stat.)} \pm 76 \text{ (syst.) fb.}$$

With respect to the nominal predicted inclusive cross-section of  $(384 \pm 36 \text{ fb})$ , the POWHEG+PYTHIA8 prediction is agreement with the data within the total uncertainties.

The fiducial differential cross sections are measured as a function of eight kinematic variables,  $p_T^{t,1}$  is transverse momentum of Leading Large-R jet,  $|y^{t,1}|$  is rapidity of the Leading Large-R jet,  $p_T^{t,2}$  is transverse momentum of Leading Large-R jet,  $|y^{t,2}|$  is rapidity of the Leading Large-R jet,  $p_T^{t\bar{t}}$  is transverse momentum of the  $t\bar{t}$  system,  $m^{t\bar{t}}$  is invariant mass of the  $t\bar{t}$  system,  $|y^{t\bar{t}}|$  is rapidity of the  $t\bar{t}$  system, and  $\Delta\phi(t_1, t_2)$  denotes azimuthal angle between the Leading and 2nd Leading

Large-jets. The measured differential cross sections including absolute and normalized cross sections are qualitatively and quantitatively compared to the four models, POWHEG+PYTHIA8, POWHEG+HERWIG7, aMC@NLO+PYTHIA8 and SHERPA. For the rapidities of the Leading top quark and of the  $t\bar{t}$  system, the data are overestimated by all predictions in the region  $|y| > 1.0$ . Among four predictions, the most significant discrepancy between prediction and data is the aMC@NLO+PYTHIA8 prediction for the kinematics of  $t\bar{t}$  system ( $\Delta\phi_{t\bar{t}}$ ) associated the emission of radiation along with the  $t\bar{t}$  pair.

This analysis shows that studies of boosted top quark jets can be performed with good signal to background ratios in the all-hadronic channel. This have created opportunities for more detailed studies of high  $p_T$  Standard Model processes. The measured differential cross sections provides measurements to test models of  $t\bar{t}$  production and give the feedback to these model theories that are sensitive to QCD radiation in high  $p_T$  region.

# Acknowledgement

I would like to thank all peoples who directly contributed to this thesis and indirectly helped me for the past several years at CERN and in Japan.

First, I would like to thank Prof. Hisaya Kurashige to bring me to the particle physics world. He also introduced me to the very warm study group, Kobe University Particle Physics Group. With his further introduction and recommendation, I started my study under the guidance of Prof. Yuji Yamazaki. I really thanks to the Prof. Yuji Yamazaki. Without his great help, this dissertation can be not completed. In the past five years from the master course until so far, he taught me not only the particle physics knowledge, but also helped me improve the Japanese level so that I lived well everyday in Japan. He always kindly and patiently encouraged me when I got lost and confused. I have caused him untold troubles so far. I very appreciates that he always accommodate my wayward. I also thanks to other staffs in the Kobe University Particle Physics Group, specially Prof. Yasuo Takeuchi, Prof. Kentaro Miuchi, Ochi Atsuhiko and Achimu Suzuki. They taught much knowledge about the particle physics.

In the subgroup of Kobe University Particle Physics Group, Kobe ATLAS group, I have the opportunity to travel to CERN to do the project of international collaboration, where I thanks to Yumi Yokoyama who helped me deal with the travel formalities. To be honest, I feel very lucky to study in this group. Every weekly meeting, I can receive many advices from these these members, Junpei Maeda, Kentaro Kawade and Shima Shimizu. Thanks to their help, my study can move on step by step.

I would like to extend my appreciations to my physics analysis group, "ttbar all-hadronic differential cross section" group. I appreciates that Shima Shimizu led me into this analysis group and help me accommodate my first physics analysis. I regret that she did not supervise this thesis until the end, I only express my sincere thank to her here. For analysis team members, Pekka Sinervo, Francesco Spano, Riccardo Di Sipio, Roman Lisak, Kyle James Read Cormier and Petr Jacka, thanks to them for greatly patience to help my study. Discussions with them have been extremely useful for my understanding and improvement of the analysis. Among others, Francesco gave me face-to-face conversation in his busy schedule.

I expresses my appreciation to the Japan HLT muon group. I am thankful to in particular, Prof. Kunihiro Nagano, Pro. Masaki Ishitsuka and Masato Aoki. They taught much knowledge to how to do the master study. I learned a lot of things in the group, analysis using the data and simulations. Due to these techniques, I can

continue to do my doctoral research.

For life at CERN, it is supported by a lot of colleagues, Dai Kobayashi, Masahiro Tanaka, Shota Suzuki, Takuya Honda and Shogo Kido. Qing Wang, Zijian Liu, Hongyi Qu, Qing Liang, Youmin Yu, Shuangling Yue and Fei Yang. I can stay at CERN and live happily for a long time thanks to companionships with them. These family dinners are unforgettable memories for me.

For life in Japan, I was worry about financial difficulties as an overseas students while studying in Japan due to much higher commodity prices, living costs, and tuition fees. I appreciates the financial support by Hirose International Scholarship Foundation, Kobayashi International Scholarship Foundation and Hyogo Scholarship for Privately Financed Students so that I can concentrate fully on my study in the past five years. In particular, I would like to thanks to Mitsuru Saeki. I also thanks to my Chinese friends, Dan Liang, Yu Qi, Shengqin Lin and Sheng Cao.

Finally, I would like to thank to my family in China from the bottom of my heart. Without your unconditional love and support, I can obviously not finish my research.

No matter what, to the people I have met and interacted with along the way, I would like to say,

Thank you very much.

本当にありがとうございました.

정말 감사합니다.

Merci.

谢谢大家

Ye Chen

January, 2018

# Bibliography

- [1] [https://en.wikipedia.org/wiki/Standard\\_Model](https://en.wikipedia.org/wiki/Standard_Model) .
- [2] ATLAS Collaboration, *Observation of a new particle in the search for the Standard Model Higgs boson with the ATLAS detector at the LHC*, Phys. Lett. B (2012) 716,1, arXiv:1207.7214.
- [3] CDF Collaboration, *Observation of top quark production in  $p\bar{p}$  collisions*, Phys. Rev. Lett (1995) 74,2626, arXiv:9503002.
- [4] DØ Collaboration, *Observation of the top quark*, Phys. Rev. Lett (1995) 74,2632, arXiv:9503003.
- [5] C. The ATLAS, CDF and D. Collaborations, *First combination of Tevatron and LHC measurements of the top-quark mass*, arXiv:1403.4427.
- [6] CMS Collaboration, *Measurement of the top quark mass using proton-proton data at  $\sqrt{s} = 7$  and  $8$  TeV*, Phys. Rev. D 93 (2016) 072004 , arXiv:1509.04044.
- [7] ATLAS Collaboration, *Measurement of the top quark mass in the  $t\bar{t} \rightarrow$  lepton+jets channel from  $\sqrt{s}= 8$ TeV ATLAS data*, ATLAS-CONF-2017-071 .
- [8] <https://nnpdf.hepforge.org> .
- [9] ATLAS Collaboration <https://atlas.web.cern.ch/Atlas/GROUPS/PHYSICS/CombinedSummaryPlots/TOP/> .
- [10] [https://www-d0.fnal.gov/Run2Physics/top/top\\_public\\_web\\_pages/top\\_feynman\\_diagrams.html](https://www-d0.fnal.gov/Run2Physics/top/top_public_web_pages/top_feynman_diagrams.html) .
- [11] <http://cms.web.cern.ch/news/jets-cms-and-determination-their-energy-scale> .
- [12] CERN OPEN-PHO-ACCEL-2014-001 .
- [13] Shank, James T., *The ATLAS Detector: Status and Results from Cosmic Rays*, arXiv:0910.3081.
- [14] C Kourkouvelis and S Vourakis, *HYPATIA—an online tool for ATLAS event visualization*, C Kourkouvelis and S Vourakis 2014 Phys. Educ. 49 21 .

- [15] ATLAS Collaboration  
<http://atlasexperiment.org/photos/inner-detector-combined.html> .
- [16] <https://twiki.cern.ch/twiki/bin/view/AtlasProtected/InDetTrackingDC14> .
- [17] ATLAS Collaboration, *Track Reconstruction Performance of the ATLAS Inner Detector at  $\sqrt{s}=13\text{TeV}$* , ATL-PHYS-PUB-2015-018 .
- [18] The ATLAS Collaboration, *The ATLAS experiment at the CERN Large Hadron Collider*, JINST **3** (2008) S08003.
- [19] ATLAS Collaboration, *Jet energy scale measurements and their systematic uncertainties in proton-proton collisions at  $\sqrt{s} = 13 \text{ TeV}$  with the ATLAS detector*, Phys. Rev. D 96 (2017) 072002 , [arXiv:1703.09665](https://arxiv.org/abs/1703.09665).
- [20] J.J. Goodson, *Search for Supersymmetry in States with Large Missing Transverse Momentum and Three Leptons including a Z-Boson*, Stony Brook University (2012) .
- [21] ATLAS Collaboration, *The ATLAS Muon Trigger: Experience and Performance in the first 3 years of LHC pp runs*, ATL-DAQ-PROC-2013-002 .
- [22] ATLAS Collaboration, *2015 start-up trigger menu and initial performance assessment of the ATLAS trigger using Run-2 data. Technical report*, CERN, ATL-DAQ-PUB-2016- 001, Geneva, March 2016 .
- [23] ATLAS Collaboration, *The ATLAS Data Acquisition System in LHC Run 2*, ATL-DAQ-PROC-2017-007 .
- [24] ATLAS Collaboration, *Luminosity determination in pp collisions at  $\sqrt{s} = 8 \text{ TeV}$  using the ATLAS detector at the LHC*, Eur. Phys. J. C 76 (2016) 653 , [arXiv:1608.03953](https://arxiv.org/abs/1608.03953).
- [25] S. M. White et al., *FIRST LUMINOSITY SCANS IN THE LHC*, MOPEC014 .
- [26] ATLAS Collaboration <https://twiki.cern.ch/twiki/bin/view/AtlasPublic/LuminosityPublicResultsRun2> .
- [27] [https://www.lhc-closer.es/taking\\_a\\_closer\\_look\\_at\\_lhc/0.lhc\\_p\\_collisions](https://www.lhc-closer.es/taking_a_closer_look_at_lhc/0.lhc_p_collisions) .
- [28] ATLAS Collaboration ATLAS-PHO-Event-2015-010 .
- [29] S. Agostinelli et al., *GEANT4: a simulation toolkit*, Nucl. Instrum. Methods Phys. A 506 (2003) 250 , CERN-IT-2002-003.
- [30] M.A. Dobbs, *Les Houches Guidebook to Monte Carlo Generators for Hadron Collider Physics*, [arXiv:0403045](https://arxiv.org/abs/0403045) .

- [31] S. Frixione, *A positive-weight next-to-leading-order Monte Carlo for heavy flavour hadroproduction*, JHEP 09 (2007) 126 , [arXiv:0707.3088](#).
- [32] S. Frixione, *Matching NLO QCD and parton showers in heavy flavor production*, JHEP 08 (2003) 007 , [arXiv:0305252](#).
- [33] T. Sjostrand, *A Brief Introduction to PYTHIA 8.1*, Comput. Phys. Commun. 178 (2008) 852 , [arXiv:0710.3820](#).
- [34] J. Bellm et al., *Herwig 7.0/Herwig++ 3.0 release note*, Eur. Phys. J. C76 (2016) 196 , [arXiv:1512.01178](#).
- [35] T. Gleisberg et al., *Event generation with SHERPA 1.1*, JHEP 0902 (2009) 007 , [arXiv:0811.4622](#).
- [36] A. Collaboration, *Jet energy measurement and its systematic uncertainty in proton-proton collisions at  $\sqrt{s} = 7\text{TeV}$  with the ATLAS detector*, J. High Energy Phys. 0804 (2008) 063 .
- [37] W. Lampl et al., *Calorimeter Clustering Algorithms: Description and Performance*, Tech. Rep. ATL-LARG-PUB-2008-002 .
- [38] ATLAS Collaboration, *Jet Calibration and Systematic Uncertainties for Jets Reconstructed in the ATLAS Detector at  $\sqrt{s} = 13\text{ TeV}$* , ATL-PHYS-PUB-2015-015 (2015), <https://cds.cern.ch/record/2037613> .
- [39] ATLAS Collaboration, *Optimization of the ATLAS b-tagging performance for the 2016 LHC run*, ATLAS-CONF-2016-012, <https://atlas.web.cern.ch/Atlas/GROUPS/PHYSICS/PUBNOTES/ATL-PHYS-PUB-2016-012/> .
- [40] A. Hocker et al., *TMVA: Toolkit for multivariate data analysis*, PoS ACAT (2007) , [arXiv:0703039](#).
- [41] A. Collaboration ATL-PHYS-PUB-2015-022 .
- [42] A. Collaboration <http://atlas.web.cern.ch/Atlas/GROUPS/PHYSICS/PLOTS/FTAG-2017-005/> .
- [43] A. Collaboration, *Performance of jet substructure techniques for large-R jets in proton-proton collisions at  $\sqrt{s}=7\text{ TeV}$  using the ATLAS detector*, JHEP09 (2013) 076 , [arXiv:1306.4945](#).
- [44] ATLAS Collaboration, *Boosted hadronic top identification at ATLAS for early 13 TeV data*, ATL-PHYS-PUB-2015-053 .
- [45] ATLAS Collaboration, *Electron efficiency measurements with the ATLAS detector using the 2015 LHC proton-proton collision data*, ATL-CONF-2016-024, <https://cds.cern.ch/record/2157687> .

- [46] ATLAS Collaboration, *Muon reconstruction performance of the ATLAS detector in proton–proton collision data at  $\sqrt{s} = 13$  TeV (2016)*, arXiv:1603.05598 .
- [47] ATLAS Collaboration, *Search for resonances decaying into top-quark pairs using fully hadronic decays in pp collisions with ATLAS at  $\sqrt{s} = 7$  TeV*, JHEP 01 (2013) 116 , arXiv:1211.2202.
- [48] G. D’Agostini, *A Multidimensional unfolding method based on Bayes’ theorem*, Nucl. Instrum. Meth. **A362** (1995) 487–498.
- [49] ATLAS Collaboration, *Measurement of the differential cross-section of highly boosted top quarks as a function of their transverse momentum in  $\sqrt{s} = 8$  TeV proton-proton collisions using the ATLAS detector*, Phys. Rev. D93 (2016) 032009 , arXiv:1510.03818.
- [50] ATLAS Collaboration, *Measurements of top-quark pair differential cross-sections in the lepton+jets channel in pp collisions at  $\sqrt{s}=13$  TeV using the ATLAS detector*, (2017) , arXiv:1708.00727.
- [51] ATLAS Collaboration, *Jet mass reconstruction with the ATLAS Detector in early Run 2 data*, ATLAS-CONF-2016-035 (2016), <http://cdsweb.cern.ch/record/2200211> .
- [52] ATLAS Collaboration, *Performance of jet substructure techniques for large- $R$  jets in proton-proton collisions at  $\sqrt{s} = 7$  TeV using the ATLAS detector*, JHEP 09 (2013) 076 , arXiv:1306.4945.
- [53] A. Collaboration, *Measurement of large radius jet mass reconstruction performance at  $\sqrt{s} = 8$  TeV using the ATLAS detector*, (2016), <http://cdsweb.cern.ch/record/2139642> .
- [54] A. Collaboration, *Jet energy measurement and its systematic uncertainty in proton-proton collisions at  $\sqrt{s} = 7$  TeV with the ATLAS detector*, Eur. Phys. J. C75 (2015) 17 , arXiv:1406.0076.
- [55] A. Collaboration, *Jet energy resolution in proton-proton collisions at  $\sqrt{s} = 7$  TeV recorded in 2010 with the ATLAS detector*, Eur. Phys. J. C 73 (2013) 2306 , arXiv:1210.6210.
- [56] A. Collaboration, *Electron performance measurements with the ATLAS detector using the 2010 LHC proton-proton collision data*, Eur. Phys. J. C 72 (2012) 1909 , arXiv:1110.3174.
- [57] A. Collaboration, *Measurement of the muon reconstruction performance of the ATLAS detector using 2011 and 2012 LHC proton–proton collision data*, Eur. Phys. J. C74 (2014) 3130 , arXiv:1407.3935.

- [58] J. Butterworth, *PDF4LHC recommendations for LHC Run II*, J. Phys.G43(2016) 023001 , [arXiv:1510.03865 \[hep-ph\]](#).
- [59] C. Collaboration, *Measurement of differential cross sections for top quark pair production using the lepton+jets final state in proton-proton collisions at 13 TeV*, Phys. Rev. D 95 (2017) 092001 , [arXiv:1610.04191](#).
- [60] ATLAS Collaboration, *Measurements of top-quark pair differential cross-sections in the lepton+jets channel in pppp collisions at  $\sqrt{s}=13$  TeV using the ATLAS detector*, JHEP 1711 (2017) 191 , [arXiv:1708.00727](#).
- [61] ATLAS Collaboration, *Measurement of jet activity produced in top-quark events with an electron, a muon and two bb-tagged jets in the final state in pp collisions at  $\sqrt{s}=13$  TeV with the ATLAS detector*, Eur. Phys. J. C77 (2017) 220 , [arXiv:1610.09978](#).

# Chapter 11

## Appendix

### 11.1 Tables of systematic uncertainties in detail for $t\bar{t}$ fiducial inclusive cross section

Total Uncertainty [%]	$\pm 24.4$
Statistics [%]	$\pm 2.3$
Systematics [%]	$\pm 24.3$
(JES) $b$ -Tagged jet energy scale [%]	-
(JES) Effective detector NP set 1 [%]	-
(JES) Effective detector NP set 2 [%]	-
(JES) Effective detector NP set 3 [%]	-
(JES) Effective detector NP set 4 [%]	-
(JES) Effective detector NP set 5 [%]	-
(JES) Effective detector NP set 6 [%]	-
(JES) Effective detector NP set 7 [%]	-
(JES) Effective detector NP set 8 restTerm [%]	-
(JES) $\eta$ intercalibration model [%]	-
(JES) $\eta$ intercalibration total stat [%]	-
(JES) Flavor composition [%]	+0.24 -0.16
(JES) Flavor response [%]	-
(JES) Pile-up offset $\mu$ [%]	-
(JES) Pile-up offset $N_{PV}$ [%]	-
(JES) Pile-up offset $p_T$ [%]	-
(JES) Pile-up offset $\rho$ topology [%]	+0.19 -0.10
(JES) Punch-through [%]	-
(JES) Single particle high- $p_T$ [%]	-
(LJES) Large- $R$ jet Baseline mass [%]	+0.30 -0.49
(LJES) Large- $R$ jet Baseline $p_T$ [%]	$\pm 2.27$
(LJES) Large- $R$ jet Baseline $\tau_{32}$ [%]	$\mp 7.76$
(LJES) Large- $R$ jet Modelling mass [%]	+0.36 -0.47
(LJES) Large- $R$ jet Modelling $p_T$ [%]	$\pm 2.25$

(LJES) Large- $R$ jet Modelling $\tau_{32}$ [%]	$\mp 9.84$
(LJES) Large- $R$ jet Tracking mass [%]	$\pm 0.13$
(LJES) Large- $R$ jet Tracking $p_T$ [%]	$\pm 4.96$
(LJES) Large- $R$ jet Tracking $\tau_{32}$ [%]	$\mp 0.39$
(LJES) Large- $R$ jet TotalStat mass [%]	-
(LJES) Large- $R$ jet TotalStat $p_T$ [%]	$\pm 0.28$
(LJES) Large- $R$ jet TotalStat $\tau_{32}$ [%]	$\mp 0.16$
(LJES) Large- $R$ jet top-quark mass resolution [%]	$\mp 1.30$
(FTAG) $b$ -Quark tagging efficiency (eigenvector 0) [%]	$\mp 5.29$
(FTAG) $b$ -Quark tagging efficiency (eigenvector 1) [%]	$\mp 4.90$
(FTAG) $b$ -Quark tagging efficiency (eigenvector 2) [%]	$\mp 0.75$
(FTAG) $b$ -Quark tagging efficiency (eigenvector 3) [%]	$\mp 0.51$
(FTAG) $b$ -Quark tagging efficiency (eigenvector 4) [%]	$\mp 0.24$
(FTAG) $c$ -Quark tagging efficiency (eigenvector 0) [%]	$\mp 2.06$
(FTAG) $c$ -Quark tagging efficiency (eigenvector 1) [%]	$\mp 1.29$
(FTAG) $c$ -Quark tagging efficiency (eigenvector 2) [%]	${}_{+0.13}^{-0.59}$
(FTAG) $c$ -Quark tagging efficiency (eigenvector 3) [%]	$\pm 0.44$
(FTAG) Light-jet tagging efficiency (eigenvector 0) [%]	$\mp 0.26$
(FTAG) Light-jet tagging efficiency (eigenvector 1) [%]	-
(FTAG) Light-jet tagging efficiency (eigenvector 2) [%]	$\pm 0.12$
(FTAG) Light-jet tagging efficiency (eigenvector 3) [%]	-
(FTAG) Light-jet tagging efficiency (eigenvector 4) [%]	-
(FTAG) Light-jet tagging efficiency (eigenvector 5) [%]	-
(FTAG) Light-jet tagging efficiency (eigenvector 6) [%]	-
(FTAG) Light-jet tagging efficiency (eigenvector 7) [%]	-
(FTAG) Light-jet tagging efficiency (eigenvector 8) [%]	${}_{-0.24}^-$
(FTAG) Light-jet tagging efficiency (eigenvector 9) [%]	${}_{-0.24}^-$
(FTAG) Light-jet tagging efficiency (eigenvector 10) [%]	-
(FTAG) Light-jet tagging efficiency (eigenvector 11) [%]	-
(FTAG) Light-jet tagging efficiency (eigenvector 12) [%]	-
(FTAG) Light-jet tagging efficiency (eigenvector 13) [%]	-
(FTAG) $b$ -Quark tagging extrapolation [%]	$\pm 3.02$
(FTAG) $b$ -Quark tagging extrapolation from $c$ -Quark [%]	-
(PDF) PDF4LHC15 eigenvector 01 [%]	-
(PDF) PDF4LHC15 eigenvector 02 [%]	$\mp 0.55$
(PDF) PDF4LHC15 eigenvector 03 [%]	-
(PDF) PDF4LHC15 eigenvector 04 [%]	$\mp 0.20$
(PDF) PDF4LHC15 eigenvector 05 [%]	$\mp 2.19$
(PDF) PDF4LHC15 eigenvector 06 [%]	$\mp 0.26$
(PDF) PDF4LHC15 eigenvector 07 [%]	-
(PDF) PDF4LHC15 eigenvector 08 [%]	$\mp 0.35$
(PDF) PDF4LHC15 eigenvector 09 [%]	$\mp 0.19$
(PDF) PDF4LHC15 eigenvector 10 [%]	-
(PDF) PDF4LHC15 eigenvector 11 [%]	$\mp 0.33$

(PDF) PDF4LHC15 eigenvector 12 [%]	$\mp 0.29$
(PDF) PDF4LHC15 eigenvector 13 [%]	-
(PDF) PDF4LHC15 eigenvector 14 [%]	-
(PDF) PDF4LHC15 eigenvector 15 [%]	$\mp 0.16$
(PDF) PDF4LHC15 eigenvector 16 [%]	-
(PDF) PDF4LHC15 eigenvector 17 [%]	$\pm 0.36$
(PDF) PDF4LHC15 eigenvector 18 [%]	-
(PDF) PDF4LHC15 eigenvector 19 [%]	$\mp 0.73$
(PDF) PDF4LHC15 eigenvector 20 [%]	$\pm 0.12$
(PDF) PDF4LHC15 eigenvector 21 [%]	-
(PDF) PDF4LHC15 eigenvector 22 [%]	$\pm 0.83$
(PDF) PDF4LHC15 eigenvector 23 [%]	-
(PDF) PDF4LHC15 eigenvector 24 [%]	-
(PDF) PDF4LHC15 eigenvector 25 [%]	-
(PDF) PDF4LHC15 eigenvector 26 [%]	-
(PDF) PDF4LHC15 eigenvector 27 [%]	$\mp 0.25$
(PDF) PDF4LHC15 eigenvector 28 [%]	$\mp 0.11$
(PDF) PDF4LHC15 eigenvector 29 [%]	-
(PDF) PDF4LHC15 eigenvector 30 [%]	-
(LEP) Electron energy resolution [%]	-
(LEP) Electron energy scale [%]	-
(LEP) Muon energy scale [%]	-
(LEP) Muon (MS) momentum resolution [%]	-
(LEP) Muon (ID) momentum resolution [%]	-
(LEP) Muon sagitta resolution bias [%]	-
(LEP) Muon sagitta $\rho$ [%]	-
(MET/PU) $E_T^{miss}$ Soft jet resolution para [%]	-
(MET/PU) $E_T^{miss}$ Soft jet resolution perp [%]	-
(MET/PU) $E_T^{miss}$ Soft jet scale [%]	-
(MET/PU) Jet vertex tagging [%]	-
Luminosity [%]	$\pm 2.01$
(BKG) Single top $Wt$ cross-section [%]	-
(BKG) Single top $t$ -channel treatment [%]	$\pm 0.21$
(BKG) $t\bar{t}+W$ cross-section [%]	-
(BKG) $t\bar{t}+Z$ cross-section [%]	-
(BKG) $t\bar{t}+H$ cross-section [%]	-
(BKG) Multijet background statistics [%]	$\pm 0.86$
(MOD) Monte Carlo sample statistics [%]	$\pm 0.90$
(MOD) ISR/FSR + scale [%]	$\pm 1.13$
(MOD) Alternative hard-scattering model [%]	$\mp 11.2$
(MOD) Alternative parton-shower model [%]	$\mp 13.7$

---

Table 11.1: The individual systematic uncertainties in the fiducial phase-space absolute inclusive cross-sections calculated as a percentage of the cross-section. Dashes are used when the estimated relative systematic uncertainty is below 0.01%.

## 11.2 Particle level covariances and correlations

### 11.2.1 Covariance and correlations for absolute differential cross section

bin [GeV]	350-400	400-450	450-500	500-550	550-600	600-800	800-1200
350-400	$1.75 \times 10^{-8}$	$2.32 \times 10^{-8}$	$3.44 \times 10^{-8}$	$3.56 \times 10^{-8}$	$2.04 \times 10^{-8}$	$8.86 \times 10^{-9}$	$9.38 \times 10^{-10}$
400-450	$2.32 \times 10^{-8}$	$5.20 \times 10^{-8}$	$6.65 \times 10^{-8}$	$6.56 \times 10^{-8}$	$3.89 \times 10^{-8}$	$1.68 \times 10^{-8}$	$1.77 \times 10^{-9}$
450-500	$3.44 \times 10^{-8}$	$6.65 \times 10^{-8}$	$1.08 \times 10^{-7}$	$1.02 \times 10^{-7}$	$5.75 \times 10^{-8}$	$2.52 \times 10^{-8}$	$2.56 \times 10^{-9}$
500-550	$3.56 \times 10^{-8}$	$6.56 \times 10^{-8}$	$1.02 \times 10^{-7}$	$1.11 \times 10^{-7}$	$5.97 \times 10^{-8}$	$2.53 \times 10^{-8}$	$2.47 \times 10^{-9}$
550-600	$2.04 \times 10^{-8}$	$3.89 \times 10^{-8}$	$5.75 \times 10^{-8}$	$5.97 \times 10^{-8}$	$3.96 \times 10^{-8}$	$1.45 \times 10^{-8}$	$1.48 \times 10^{-9}$
600-800	$8.86 \times 10^{-9}$	$1.68 \times 10^{-8}$	$2.52 \times 10^{-8}$	$2.53 \times 10^{-8}$	$1.45 \times 10^{-8}$	$7.01 \times 10^{-9}$	$6.50 \times 10^{-10}$
800-1200	$9.38 \times 10^{-10}$	$1.77 \times 10^{-9}$	$2.56 \times 10^{-9}$	$2.47 \times 10^{-9}$	$1.48 \times 10^{-9}$	$6.50 \times 10^{-10}$	$1.51 \times 10^{-10}$

Table 11.2: Covariance matrix for the absolute particle-level fiducial phase-space differential cross-section as a function of the transverse momentum of the second-leading top-quark jet , accounting for the statistical and systematic uncertainties.

bin [GeV]	350-400	400-450	450-500	500-550	550-600	600-800	800-1200
350-400	<b>1.00</b>	0.77	0.79	0.81	0.77	0.80	0.58
400-450	0.77	<b>1.00</b>	0.89	0.86	0.86	0.88	0.63
450-500	0.79	0.89	<b>1.00</b>	0.93	0.88	0.91	0.63
500-550	0.81	0.86	0.93	<b>1.00</b>	0.90	0.91	0.60
550-600	0.77	0.86	0.88	0.90	<b>1.00</b>	0.87	0.61
600-800	0.80	0.88	0.91	0.91	0.87	<b>1.00</b>	0.63
800-1200	0.58	0.63	0.63	0.60	0.61	0.63	<b>1.00</b>

Table 11.3: Correlation matrix for the absolute particle-level fiducial phase-space differential cross-section as a function of the transverse momentum of the second-leading top-quark jet , accounting for the statistical and systematic uncertainties.

bin [GeV]	0.00-0.30	0.30-0.60	0.60-0.90	0.90-1.20	1.20-1.50	1.50-2.00
0.00-0.30	$3.60 \times 10^{-3}$	$3.04 \times 10^{-3}$	$2.85 \times 10^{-3}$	$2.07 \times 10^{-3}$	$1.55 \times 10^{-3}$	$7.26 \times 10^{-4}$
0.30-0.60	$3.04 \times 10^{-3}$	$3.02 \times 10^{-3}$	$2.58 \times 10^{-3}$	$1.88 \times 10^{-3}$	$1.42 \times 10^{-3}$	$6.61 \times 10^{-4}$
0.60-0.90	$2.85 \times 10^{-3}$	$2.58 \times 10^{-3}$	$2.64 \times 10^{-3}$	$1.77 \times 10^{-3}$	$1.35 \times 10^{-3}$	$6.17 \times 10^{-4}$
0.90-1.20	$2.07 \times 10^{-3}$	$1.88 \times 10^{-3}$	$1.77 \times 10^{-3}$	$1.44 \times 10^{-3}$	$9.67 \times 10^{-4}$	$4.49 \times 10^{-4}$
1.20-1.50	$1.55 \times 10^{-3}$	$1.42 \times 10^{-3}$	$1.35 \times 10^{-3}$	$9.67 \times 10^{-4}$	$8.43 \times 10^{-4}$	$3.34 \times 10^{-4}$
1.50-2.00	$7.26 \times 10^{-4}$	$6.61 \times 10^{-4}$	$6.17 \times 10^{-4}$	$4.49 \times 10^{-4}$	$3.34 \times 10^{-4}$	$1.97 \times 10^{-4}$

Table 11.4: Covariance matrix for the absolute particle-level fiducial phase-space differential cross-section as a function of absolute value of the rapidity of the leading top-quark jet , accounting for the statistical and systematic uncertainties.

bin [GeV]	0.00-0.30	0.30-0.60	0.60-0.90	0.90-1.20	1.20-1.50	1.50-2.00
0.00-0.30	<b>1.00</b>	0.92	0.92	0.91	0.89	0.86
0.30-0.60	0.92	<b>1.00</b>	0.91	0.90	0.89	0.86
0.60-0.90	0.92	0.91	<b>1.00</b>	0.91	0.90	0.86
0.90-1.20	0.91	0.90	0.91	<b>1.00</b>	0.88	0.84
1.20-1.50	0.89	0.89	0.90	0.88	<b>1.00</b>	0.82
1.50-2.00	0.86	0.86	0.86	0.84	0.82	<b>1.00</b>

Table 11.5: Correlation matrix for the absolute particle-level fiducial phase-space differential cross-section as a function of absolute value of the rapidity of the leading top-quark jet , accounting for the statistical and systematic uncertainties.

bin [GeV]	0.00-0.30	0.30-0.60	0.60-0.90	0.90-1.20	1.20-1.50	1.50-2.00
0.00-0.30	$4.43 \times 10^{-3}$	$3.76 \times 10^{-3}$	$2.77 \times 10^{-3}$	$2.36 \times 10^{-3}$	$1.58 \times 10^{-3}$	$7.37 \times 10^{-4}$
0.30-0.60	$3.76 \times 10^{-3}$	$3.65 \times 10^{-3}$	$2.46 \times 10^{-3}$	$2.13 \times 10^{-3}$	$1.44 \times 10^{-3}$	$6.65 \times 10^{-4}$
0.60-0.90	$2.77 \times 10^{-3}$	$2.46 \times 10^{-3}$	$2.07 \times 10^{-3}$	$1.55 \times 10^{-3}$	$1.04 \times 10^{-3}$	$4.86 \times 10^{-4}$
0.90-1.20	$2.36 \times 10^{-3}$	$2.13 \times 10^{-3}$	$1.55 \times 10^{-3}$	$1.49 \times 10^{-3}$	$8.81 \times 10^{-4}$	$4.18 \times 10^{-4}$
1.20-1.50	$1.58 \times 10^{-3}$	$1.44 \times 10^{-3}$	$1.04 \times 10^{-3}$	$8.81 \times 10^{-4}$	$7.44 \times 10^{-4}$	$2.75 \times 10^{-4}$
1.50-2.00	$7.37 \times 10^{-4}$	$6.65 \times 10^{-4}$	$4.86 \times 10^{-4}$	$4.18 \times 10^{-4}$	$2.75 \times 10^{-4}$	$1.55 \times 10^{-4}$

Table 11.6: Covariance matrix for the absolute particle-level fiducial phase-space differential cross-section as a function of absolute value of the rapidity of the second-leading top-quark jet , accounting for the statistical and systematic uncertainties.

bin [GeV]	0.00-0.30	0.30-0.60	0.60-0.90	0.90-1.20	1.20-1.50	1.50-2.00
0.00-0.30	<b>1.00</b>	0.94	0.92	0.92	0.87	0.89
0.30-0.60	0.94	<b>1.00</b>	0.90	0.91	0.87	0.88
0.60-0.90	0.92	0.90	<b>1.00</b>	0.88	0.84	0.86
0.90-1.20	0.92	0.91	0.88	<b>1.00</b>	0.84	0.87
1.20-1.50	0.87	0.87	0.84	0.84	<b>1.00</b>	0.81
1.50-2.00	0.89	0.88	0.86	0.87	0.81	<b>1.00</b>

Table 11.7: Correlation matrix for the absolute particle-level fiducial phase-space differential cross-section as a function of absolute value of the rapidity of the second-leading top-quark jet , accounting for the statistical and systematic uncertainties.

bin [GeV]	0-100	100-150	150-200	200-300	300-500	500-800
0-100	$1.54 \times 10^{-7}$	$9.41 \times 10^{-8}$	$6.04 \times 10^{-8}$	$2.94 \times 10^{-8}$	$9.69 \times 10^{-9}$	$9.85 \times 10^{-10}$
100-150	$9.41 \times 10^{-8}$	$7.30 \times 10^{-8}$	$4.11 \times 10^{-8}$	$1.86 \times 10^{-8}$	$6.59 \times 10^{-9}$	$5.79 \times 10^{-10}$
150-200	$6.04 \times 10^{-8}$	$4.11 \times 10^{-8}$	$3.21 \times 10^{-8}$	$1.28 \times 10^{-8}$	$4.14 \times 10^{-9}$	$4.07 \times 10^{-10}$
200-300	$2.94 \times 10^{-8}$	$1.86 \times 10^{-8}$	$1.28 \times 10^{-8}$	$8.22 \times 10^{-9}$	$1.97 \times 10^{-9}$	$2.08 \times 10^{-10}$
300-500	$9.69 \times 10^{-9}$	$6.59 \times 10^{-9}$	$4.14 \times 10^{-9}$	$1.97 \times 10^{-9}$	$1.02 \times 10^{-9}$	$6.04 \times 10^{-11}$
500-800	$9.85 \times 10^{-10}$	$5.79 \times 10^{-10}$	$4.07 \times 10^{-10}$	$2.08 \times 10^{-10}$	$6.04 \times 10^{-11}$	$2.40 \times 10^{-11}$

Table 11.8: Covariance matrix for the absolute particle-level fiducial phase-space differential cross-section as a function of transverse momentum of the  $t\bar{t}$  system , accounting for the statistical and systematic uncertainties.

bin [GeV]	0-100	100-150	150-200	200-300	300-500	500-800
0-100	<b>1.00</b>	0.89	0.86	0.83	0.77	0.51
100-150	0.89	<b>1.00</b>	0.85	0.76	0.76	0.44
150-200	0.86	0.85	<b>1.00</b>	0.79	0.72	0.46
200-300	0.83	0.76	0.79	<b>1.00</b>	0.68	0.47
300-500	0.77	0.76	0.72	0.68	<b>1.00</b>	0.39
500-800	0.51	0.44	0.46	0.47	0.39	<b>1.00</b>

Table 11.9: Correlation matrix for the absolute particle-level fiducial phase-space differential cross-section as a function of transverse momentum of the  $t\bar{t}$  system , accounting for the statistical and systematic uncertainties.

bin [GeV]	1.00-1.10	1.10-1.20	1.20-1.30	1.30-1.40	1.40-1.50	1.50-1.70	1.70-1.90	1.90-2.10	2.10-2.30	2.30-3.00
1.00-1.10	$1.41 \times 10^{-2}$	$1.65 \times 10^{-2}$	$1.24 \times 10^{-2}$	$9.05 \times 10^{-3}$	$8.81 \times 10^{-3}$	$4.19 \times 10^{-3}$	$3.70 \times 10^{-3}$	$1.59 \times 10^{-3}$	$9.58 \times 10^{-4}$	$2.34 \times 10^{-4}$
1.10-1.20	$1.65 \times 10^{-2}$	$2.54 \times 10^{-2}$	$1.69 \times 10^{-2}$	$1.19 \times 10^{-2}$	$1.20 \times 10^{-2}$	$5.64 \times 10^{-3}$	$5.00 \times 10^{-3}$	$2.21 \times 10^{-3}$	$1.26 \times 10^{-3}$	$2.96 \times 10^{-4}$
1.20-1.30	$1.24 \times 10^{-2}$	$1.69 \times 10^{-2}$	$1.44 \times 10^{-2}$	$9.20 \times 10^{-3}$	$8.66 \times 10^{-3}$	$4.26 \times 10^{-3}$	$3.73 \times 10^{-3}$	$1.61 \times 10^{-3}$	$9.66 \times 10^{-4}$	$2.37 \times 10^{-4}$
1.30-1.40	$9.05 \times 10^{-3}$	$1.19 \times 10^{-2}$	$9.20 \times 10^{-3}$	$8.12 \times 10^{-3}$	$6.36 \times 10^{-3}$	$2.98 \times 10^{-3}$	$2.69 \times 10^{-3}$	$1.15 \times 10^{-3}$	$7.45 \times 10^{-4}$	$1.83 \times 10^{-4}$
1.40-1.50	$8.81 \times 10^{-3}$	$1.20 \times 10^{-2}$	$8.66 \times 10^{-3}$	$6.36 \times 10^{-3}$	$7.41 \times 10^{-3}$	$2.85 \times 10^{-3}$	$2.60 \times 10^{-3}$	$1.12 \times 10^{-3}$	$6.60 \times 10^{-4}$	$1.67 \times 10^{-4}$
1.50-1.70	$4.19 \times 10^{-3}$	$5.64 \times 10^{-3}$	$4.26 \times 10^{-3}$	$2.98 \times 10^{-3}$	$2.85 \times 10^{-3}$	$1.91 \times 10^{-3}$	$1.18 \times 10^{-3}$	$5.31 \times 10^{-4}$	$3.21 \times 10^{-4}$	$8.05 \times 10^{-5}$
1.70-1.90	$3.70 \times 10^{-3}$	$5.00 \times 10^{-3}$	$3.73 \times 10^{-3}$	$2.69 \times 10^{-3}$	$2.60 \times 10^{-3}$	$1.18 \times 10^{-3}$	$1.42 \times 10^{-3}$	$4.54 \times 10^{-4}$	$2.66 \times 10^{-4}$	$7.19 \times 10^{-5}$
1.90-2.10	$1.59 \times 10^{-3}$	$2.21 \times 10^{-3}$	$1.61 \times 10^{-3}$	$1.15 \times 10^{-3}$	$1.12 \times 10^{-3}$	$5.31 \times 10^{-4}$	$4.54 \times 10^{-4}$	$3.73 \times 10^{-4}$	$1.09 \times 10^{-4}$	$2.80 \times 10^{-5}$
2.10-2.30	$9.58 \times 10^{-4}$	$1.26 \times 10^{-3}$	$9.66 \times 10^{-4}$	$7.45 \times 10^{-4}$	$6.60 \times 10^{-4}$	$3.21 \times 10^{-4}$	$2.66 \times 10^{-4}$	$1.09 \times 10^{-4}$	$2.09 \times 10^{-4}$	$1.70 \times 10^{-5}$
2.30-3.00	$2.34 \times 10^{-4}$	$2.96 \times 10^{-4}$	$2.37 \times 10^{-4}$	$1.83 \times 10^{-4}$	$1.67 \times 10^{-4}$	$8.05 \times 10^{-5}$	$7.19 \times 10^{-5}$	$2.80 \times 10^{-5}$	$1.70 \times 10^{-5}$	$1.52 \times 10^{-5}$

Table 11.10: Covariance matrix for the absolute particle-level fiducial phase-space differential cross-section as a function of invariant mass of the  $t\bar{t}$  system , accounting for the statistical and systematic uncertainties.

bin [GeV]	1.00-1.10	1.10-1.20	1.20-1.30	1.30-1.40	1.40-1.50	1.50-1.70	1.70-1.90	1.90-2.10	2.10-2.30	2.30-3.00
1.00-1.10	<b>1.00</b>	0.87	0.87	0.85	0.86	0.81	0.83	0.69	0.56	0.51
1.10-1.20	0.87	<b>1.00</b>	0.89	0.83	0.87	0.81	0.83	0.72	0.55	0.48
1.20-1.30	0.87	0.89	<b>1.00</b>	0.85	0.84	0.81	0.83	0.70	0.56	0.51
1.30-1.40	0.85	0.83	0.85	<b>1.00</b>	0.82	0.76	0.79	0.66	0.57	0.52
1.40-1.50	0.86	0.87	0.84	0.82	<b>1.00</b>	0.76	0.80	0.67	0.53	0.50
1.50-1.70	0.81	0.81	0.81	0.76	0.76	<b>1.00</b>	0.72	0.63	0.51	0.47
1.70-1.90	0.83	0.83	0.83	0.79	0.80	0.72	<b>1.00</b>	0.62	0.49	0.49
1.90-2.10	0.69	0.72	0.70	0.66	0.67	0.63	0.62	<b>1.00</b>	0.39	0.37
2.10-2.30	0.56	0.55	0.56	0.57	0.53	0.51	0.49	0.39	<b>1.00</b>	0.30
2.30-3.00	0.51	0.48	0.51	0.52	0.50	0.47	0.49	0.37	0.30	<b>1.00</b>

Table 11.11: Correlation matrix for the absolute particle-level fiducial phase-space differential cross-section as a function of invariant mass of the  $t\bar{t}$  system , accounting for the statistical and systematic uncertainties.

bin [GeV]	0.00-0.30	0.30-0.60	0.60-0.90	0.90-1.20	1.20-1.50	1.50-2.00
0.00-0.30	$6.83 \times 10^{-3}$	$5.20 \times 10^{-3}$	$3.67 \times 10^{-3}$	$3.00 \times 10^{-3}$	$1.22 \times 10^{-3}$	$1.56 \times 10^{-4}$
0.30-0.60	$5.20 \times 10^{-3}$	$4.51 \times 10^{-3}$	$2.98 \times 10^{-3}$	$2.38 \times 10^{-3}$	$9.84 \times 10^{-4}$	$1.27 \times 10^{-4}$
0.60-0.90	$3.67 \times 10^{-3}$	$2.98 \times 10^{-3}$	$2.40 \times 10^{-3}$	$1.66 \times 10^{-3}$	$7.00 \times 10^{-4}$	$9.88 \times 10^{-5}$
0.90-1.20	$3.00 \times 10^{-3}$	$2.38 \times 10^{-3}$	$1.66 \times 10^{-3}$	$1.53 \times 10^{-3}$	$5.59 \times 10^{-4}$	$7.15 \times 10^{-5}$
1.20-1.50	$1.22 \times 10^{-3}$	$9.84 \times 10^{-4}$	$7.00 \times 10^{-4}$	$5.59 \times 10^{-4}$	$2.90 \times 10^{-4}$	$2.96 \times 10^{-5}$
1.50-2.00	$1.56 \times 10^{-4}$	$1.27 \times 10^{-4}$	$9.88 \times 10^{-5}$	$7.15 \times 10^{-5}$	$2.96 \times 10^{-5}$	$1.16 \times 10^{-5}$

Table 11.12: Covariance matrix for the absolute particle-level fiducial phase-space differential cross-section as a function of absolute value of the rapidity of the  $t\bar{t}$  system , accounting for the statistical and systematic uncertainties.

bin [GeV]	0.00-0.30	0.30-0.60	0.60-0.90	0.90-1.20	1.20-1.50	1.50-2.00
0.00-0.30	<b>1.00</b>	0.94	0.91	0.93	0.87	0.55
0.30-0.60	0.94	<b>1.00</b>	0.90	0.91	0.86	0.55
0.60-0.90	0.91	0.90	<b>1.00</b>	0.87	0.84	0.59
0.90-1.20	0.93	0.91	0.87	<b>1.00</b>	0.84	0.54
1.20-1.50	0.87	0.86	0.84	0.84	<b>1.00</b>	0.51
1.50-2.00	0.55	0.55	0.59	0.54	0.51	<b>1.00</b>

Table 11.13: Correlation matrix for the absolute particle-level fiducial phase-space differential cross-section as a function of absolute value of the rapidity of the  $t\bar{t}$  system , accounting for the statistical and systematic uncertainties.

bin [GeV]	0.00-2.50	2.50-2.75	2.75-3.00	3.00-3.14
0.00-2.50	$1.23 \times 10^{-6}$	$1.33 \times 10^{-5}$	$5.54 \times 10^{-5}$	$2.80 \times 10^{-4}$
2.50-2.75	$1.33 \times 10^{-5}$	$4.80 \times 10^{-4}$	$9.68 \times 10^{-4}$	$5.28 \times 10^{-3}$
2.75-3.00	$5.54 \times 10^{-5}$	$9.68 \times 10^{-4}$	$5.21 \times 10^{-3}$	$2.45 \times 10^{-2}$
3.00-3.14	$2.80 \times 10^{-4}$	$5.28 \times 10^{-3}$	$2.45 \times 10^{-2}$	$1.30 \times 10^{-1}$

Table 11.14: Covariance matrix for the absolute particle-level fiducial phase-space differential cross-section as a function of azimuthal angle between the two top-quark jets  $\Delta\phi_{t\bar{t}}$ , accounting for the statistical and systematic uncertainties.

bin [GeV]	0.00-2.50	2.50-2.75	2.75-3.00	3.00-3.14
0.00-2.50	<b>1.00</b>	0.55	0.69	0.70
2.50-2.75	0.55	<b>1.00</b>	0.61	0.67
2.75-3.00	0.69	0.61	<b>1.00</b>	0.94
3.00-3.14	0.70	0.67	0.94	<b>1.00</b>

Table 11.15: Correlation matrix for the absolute particle-level fiducial phase-space differential cross-section as a function of azimuthal angle between the two top-quark jets  $\Delta\phi_{t\bar{t}}$ , accounting for the statistical and systematic uncertainties.

## 11.2.2 Covariance and correlations for normalized differential cross section

bin [GeV]	500-550	550-600	600-650	650-700	700-750	750-800	800-1000	1000-1200
500-550	$1.87 \times 10^{-7}$	$1.74 \times 10^{-8}$	$-1.40 \times 10^{-8}$	$5.80 \times 10^{-9}$	$-1.05 \times 10^{-8}$	$-1.09 \times 10^{-8}$	$-6.48 \times 10^{-9}$	$-2.68 \times 10^{-9}$
550-600	$1.74 \times 10^{-8}$	$9.89 \times 10^{-8}$	$1.45 \times 10^{-8}$	$-6.03 \times 10^{-9}$	$-3.83 \times 10^{-9}$	$-3.14 \times 10^{-9}$	$-3.40 \times 10^{-9}$	$-9.95 \times 10^{-10}$
600-650	$-1.40 \times 10^{-8}$	$1.45 \times 10^{-8}$	$5.70 \times 10^{-8}$	$1.67 \times 10^{-8}$	$-6.14 \times 10^{-9}$	$1.08 \times 10^{-9}$	$1.98 \times 10^{-9}$	$6.48 \times 10^{-10}$
650-700	$5.80 \times 10^{-9}$	$-6.03 \times 10^{-9}$	$1.67 \times 10^{-8}$	$5.55 \times 10^{-8}$	$8.35 \times 10^{-9}$	$-6.67 \times 10^{-9}$	$3.20 \times 10^{-9}$	$1.15 \times 10^{-9}$
700-750	$-1.05 \times 10^{-8}$	$-3.83 \times 10^{-9}$	$-6.14 \times 10^{-9}$	$8.35 \times 10^{-9}$	$4.08 \times 10^{-8}$	$5.92 \times 10^{-9}$	$-3.65 \times 10^{-10}$	$1.04 \times 10^{-9}$
750-800	$-1.09 \times 10^{-8}$	$-3.14 \times 10^{-9}$	$1.08 \times 10^{-9}$	$-6.67 \times 10^{-9}$	$5.92 \times 10^{-9}$	$2.22 \times 10^{-8}$	$6.60 \times 10^{-10}$	$-5.72 \times 10^{-10}$
800-1000	$-6.48 \times 10^{-9}$	$-3.40 \times 10^{-9}$	$1.98 \times 10^{-9}$	$3.20 \times 10^{-9}$	$-3.65 \times 10^{-10}$	$6.60 \times 10^{-10}$	$5.20 \times 10^{-9}$	$-1.42 \times 10^{-11}$
1000-1200	$-2.68 \times 10^{-9}$	$-9.95 \times 10^{-10}$	$6.48 \times 10^{-10}$	$1.15 \times 10^{-9}$	$1.04 \times 10^{-9}$	$-5.72 \times 10^{-10}$	$-1.42 \times 10^{-11}$	$2.77 \times 10^{-9}$

Table 11.16: Covariance matrix for the normalized particle-level fiducial phase-space differential cross-section as a function of the transverse momentum of the leading top-quark jet , accounting for the statistical and systematic uncertainties.

bin [GeV]	500-550	550-600	600-650	650-700	700-750	750-800	800-1000	1000-1200
500-550	<b>1.00</b>	0.13	-0.14	0.06	-0.12	-0.17	-0.21	-0.12
550-600	0.13	<b>1.00</b>	0.19	-0.08	-0.06	-0.07	-0.15	-0.06
600-650	-0.14	0.19	<b>1.00</b>	0.30	-0.13	0.03	0.12	0.05
650-700	0.06	-0.08	0.30	<b>1.00</b>	0.18	-0.19	0.19	0.09
700-750	-0.12	-0.06	-0.13	0.18	<b>1.00</b>	0.20	-0.03	0.10
750-800	-0.17	-0.07	0.03	-0.19	0.20	<b>1.00</b>	0.06	-0.07
800-1000	-0.21	-0.15	0.12	0.19	-0.03	0.06	<b>1.00</b>	-0.00
1000-1200	-0.12	-0.06	0.05	0.09	0.10	-0.07	-0.00	<b>1.00</b>

Table 11.17: Correlation matrix for the normalized particle-level fiducial phase-space differential cross-section as a function of the transverse momentum of the leading top-quark jet , accounting for the statistical and systematic uncertainties.

bin [GeV]	350-400	400-450	450-500	500-550	550-600	600-800	800-1200
350-400	$5.11 \times 10^{-8}$	$7.28 \times 10^{-9}$	$-7.19 \times 10^{-10}$	$6.14 \times 10^{-9}$	$7.52 \times 10^{-10}$	$-1.50 \times 10^{-10}$	$-4.91 \times 10^{-10}$
400-450	$7.28 \times 10^{-9}$	$9.31 \times 10^{-8}$	$1.95 \times 10^{-8}$	$-3.95 \times 10^{-9}$	$-1.09 \times 10^{-9}$	$7.94 \times 10^{-10}$	$-1.21 \times 10^{-9}$
450-500	$-7.19 \times 10^{-10}$	$1.95 \times 10^{-8}$	$9.68 \times 10^{-8}$	$1.21 \times 10^{-8}$	$-1.34 \times 10^{-8}$	$3.53 \times 10^{-9}$	$-1.01 \times 10^{-9}$
500-550	$6.14 \times 10^{-9}$	$-3.95 \times 10^{-9}$	$1.21 \times 10^{-8}$	$7.12 \times 10^{-8}$	$2.79 \times 10^{-9}$	$-2.66 \times 10^{-9}$	$-1.50 \times 10^{-9}$
550-600	$7.52 \times 10^{-10}$	$-1.09 \times 10^{-9}$	$-1.34 \times 10^{-8}$	$2.79 \times 10^{-9}$	$5.06 \times 10^{-8}$	$1.17 \times 10^{-10}$	$1.87 \times 10^{-10}$
600-800	$-1.50 \times 10^{-10}$	$7.94 \times 10^{-10}$	$3.53 \times 10^{-9}$	$-2.66 \times 10^{-9}$	$1.17 \times 10^{-10}$	$7.33 \times 10^{-9}$	$2.97 \times 10^{-10}$
800-1200	$-4.91 \times 10^{-10}$	$-1.21 \times 10^{-9}$	$-1.01 \times 10^{-9}$	$-1.50 \times 10^{-9}$	$1.87 \times 10^{-10}$	$2.97 \times 10^{-10}$	$7.95 \times 10^{-10}$

Table 11.18: Covariance matrix for the normalized particle-level fiducial phase-space differential cross-section as a function of the transverse momentum of the second-leading top-quark jet , accounting for the statistical and systematic uncertainties.

bin [GeV]	350-400	400-450	450-500	500-550	550-600	600-800	800-1200
350-400	<b>1.00</b>	0.11	-0.01	0.10	0.01	-0.01	-0.08
400-450	0.11	<b>1.00</b>	0.20	-0.05	-0.02	0.03	-0.14
450-500	-0.01	0.20	<b>1.00</b>	0.15	-0.19	0.13	-0.12
500-550	0.10	-0.05	0.15	<b>1.00</b>	0.05	-0.12	-0.20
550-600	0.01	-0.02	-0.19	0.05	<b>1.00</b>	0.01	0.03
600-800	-0.01	0.03	0.13	-0.12	0.01	<b>1.00</b>	0.12
800-1200	-0.08	-0.14	-0.12	-0.20	0.03	0.12	<b>1.00</b>

Table 11.19: Correlation matrix for the normalized particle-level fiducial phase-space differential cross-section as a function of the transverse momentum of the second-leading top-quark jet , accounting for the statistical and systematic uncertainties.

bin [GeV]	0.00-0.30	0.30-0.60	0.60-0.90	0.90-1.20	1.20-1.50	1.50-2.00
0.00-0.30	$1.84 \times 10^{-3}$	$-2.98 \times 10^{-4}$	$1.41 \times 10^{-4}$	$-1.87 \times 10^{-4}$	$-9.07 \times 10^{-6}$	$-4.15 \times 10^{-5}$
0.30-0.60	$-2.98 \times 10^{-4}$	$2.03 \times 10^{-3}$	$9.54 \times 10^{-5}$	$-2.42 \times 10^{-5}$	$9.62 \times 10^{-5}$	$-6.32 \times 10^{-5}$
0.60-0.90	$1.41 \times 10^{-4}$	$9.54 \times 10^{-5}$	$2.04 \times 10^{-3}$	$-1.01 \times 10^{-6}$	$2.51 \times 10^{-4}$	$7.47 \times 10^{-5}$
0.90-1.20	$-1.87 \times 10^{-4}$	$-2.42 \times 10^{-5}$	$-1.01 \times 10^{-6}$	$1.24 \times 10^{-3}$	$-4.09 \times 10^{-5}$	$-3.69 \times 10^{-5}$
1.20-1.50	$-9.07 \times 10^{-6}$	$9.62 \times 10^{-5}$	$2.51 \times 10^{-4}$	$-4.09 \times 10^{-5}$	$9.21 \times 10^{-4}$	$-6.96 \times 10^{-6}$
1.50-2.00	$-4.15 \times 10^{-5}$	$-6.32 \times 10^{-5}$	$7.47 \times 10^{-5}$	$-3.69 \times 10^{-5}$	$-6.96 \times 10^{-6}$	$3.30 \times 10^{-4}$

Table 11.20: Covariance matrix for the normalized particle-level fiducial phase-space differential cross-section as a function of absolute value of the rapidity of the leading top-quark jet , accounting for the statistical and systematic uncertainties.

bin [GeV]	0.00-0.30	0.30-0.60	0.60-0.90	0.90-1.20	1.20-1.50	1.50-2.00
0.00-0.30	<b>1.00</b>	-0.15	0.07	-0.12	-0.01	-0.05
0.30-0.60	-0.15	<b>1.00</b>	0.05	-0.02	0.07	-0.08
0.60-0.90	0.07	0.05	<b>1.00</b>	-0.00	0.18	0.09
0.90-1.20	-0.12	-0.02	-0.00	<b>1.00</b>	-0.04	-0.06
1.20-1.50	-0.01	0.07	0.18	-0.04	<b>1.00</b>	-0.01
1.50-2.00	-0.05	-0.08	0.09	-0.06	-0.01	<b>1.00</b>

Table 11.21: Correlation matrix for the normalized particle-level fiducial phase-space differential cross-section as a function of absolute value of the rapidity of the leading top-quark jet , accounting for the statistical and systematic uncertainties.

bin [GeV]	0.00-0.30	0.30-0.60	0.60-0.90	0.90-1.20	1.20-1.50	1.50-2.00
0.00-0.30	$1.71 \times 10^{-3}$	$-2.95 \times 10^{-4}$	$-9.71 \times 10^{-5}$	$-1.69 \times 10^{-4}$	$1.27 \times 10^{-4}$	$-2.11 \times 10^{-5}$
0.30-0.60	$-2.95 \times 10^{-4}$	$1.74 \times 10^{-3}$	$-2.33 \times 10^{-4}$	$-1.19 \times 10^{-4}$	$9.33 \times 10^{-6}$	$-2.33 \times 10^{-5}$
0.60-0.90	$-9.71 \times 10^{-5}$	$-2.33 \times 10^{-4}$	$2.12 \times 10^{-3}$	$-5.78 \times 10^{-5}$	$3.54 \times 10^{-5}$	$5.44 \times 10^{-5}$
0.90-1.20	$-1.69 \times 10^{-4}$	$-1.19 \times 10^{-4}$	$-5.78 \times 10^{-5}$	$1.31 \times 10^{-3}$	$-1.12 \times 10^{-4}$	$3.80 \times 10^{-6}$
1.20-1.50	$1.27 \times 10^{-4}$	$9.33 \times 10^{-6}$	$3.54 \times 10^{-5}$	$-1.12 \times 10^{-4}$	$1.30 \times 10^{-3}$	$-1.38 \times 10^{-5}$
1.50-2.00	$-2.11 \times 10^{-5}$	$-2.33 \times 10^{-5}$	$5.44 \times 10^{-5}$	$3.80 \times 10^{-6}$	$-1.38 \times 10^{-5}$	$2.13 \times 10^{-4}$

Table 11.22: Covariance matrix for the normalized particle-level fiducial phase-space differential cross-section as a function of absolute value of the rapidity of the second-leading top-quark jet , accounting for the statistical and systematic uncertainties.

bin [GeV]	0.00-0.30	0.30-0.60	0.60-0.90	0.90-1.20	1.20-1.50	1.50-2.00
0.00-0.30	<b>1.00</b>	-0.17	-0.05	-0.11	0.09	-0.03
0.30-0.60	-0.17	<b>1.00</b>	-0.12	-0.08	0.01	-0.04
0.60-0.90	-0.05	-0.12	<b>1.00</b>	-0.03	0.02	0.08
0.90-1.20	-0.11	-0.08	-0.03	<b>1.00</b>	-0.09	0.01
1.20-1.50	0.09	0.01	0.02	-0.09	<b>1.00</b>	-0.03
1.50-2.00	-0.03	-0.04	0.08	0.01	-0.03	<b>1.00</b>

Table 11.23: Correlation matrix for the normalized particle-level fiducial phase-space differential cross-section as a function of absolute value of the rapidity of the second-leading top-quark jet , accounting for the statistical and systematic uncertainties.

bin [GeV]	0-100	100-150	150-200	200-300	300-500	500-800
0-100	$4.23 \times 10^{-8}$	$-1.22 \times 10^{-8}$	$-8.36 \times 10^{-9}$	$6.38 \times 10^{-9}$	$-2.67 \times 10^{-9}$	$1.20 \times 10^{-10}$
100-150	$-1.22 \times 10^{-8}$	$1.16 \times 10^{-7}$	$3.29 \times 10^{-9}$	$-1.53 \times 10^{-10}$	$1.13 \times 10^{-9}$	$1.64 \times 10^{-9}$
150-200	$-8.36 \times 10^{-9}$	$3.29 \times 10^{-9}$	$5.46 \times 10^{-8}$	$4.71 \times 10^{-9}$	$-9.24 \times 10^{-10}$	$1.37 \times 10^{-10}$
200-300	$6.38 \times 10^{-9}$	$-1.53 \times 10^{-10}$	$4.71 \times 10^{-9}$	$2.13 \times 10^{-8}$	$-6.65 \times 10^{-10}$	$2.80 \times 10^{-10}$
300-500	$-2.67 \times 10^{-9}$	$1.13 \times 10^{-9}$	$-9.24 \times 10^{-10}$	$-6.65 \times 10^{-10}$	$2.96 \times 10^{-9}$	$2.89 \times 10^{-11}$
500-800	$1.20 \times 10^{-10}$	$1.64 \times 10^{-9}$	$1.37 \times 10^{-10}$	$2.80 \times 10^{-10}$	$2.89 \times 10^{-11}$	$1.78 \times 10^{-10}$

Table 11.24: Covariance matrix for the normalized particle-level fiducial phase-space differential cross-section as a function of transverse momentum of the  $t\bar{t}$  system , accounting for the statistical and systematic uncertainties.

bin [GeV]	0-100	100-150	150-200	200-300	300-500	500-800
0-100	<b>1.00</b>	-0.17	-0.17	0.21	-0.24	0.04
100-150	-0.17	<b>1.00</b>	0.04	-0.00	0.06	0.36
150-200	-0.17	0.04	<b>1.00</b>	0.14	-0.07	0.04
200-300	0.21	-0.00	0.14	<b>1.00</b>	-0.08	0.14
300-500	-0.24	0.06	-0.07	-0.08	<b>1.00</b>	0.04
500-800	0.04	0.36	0.04	0.14	0.04	<b>1.00</b>

Table 11.25: Correlation matrix for the normalized particle-level fiducial phase-space differential cross-section as a function of transverse momentum of the  $t\bar{t}$  system , accounting for the statistical and systematic uncertainties.

bin [GeV]	1.00-1.10	1.10-1.20	1.20-1.30	1.30-1.40	1.40-1.50	1.50-1.70	1.70-1.90	1.90-2.10	2.10-2.30	2.30-3.00
1.00-1.10	<b>1.00</b>	$1.91 \times 10^{-2}$	$1.09 \times 10^{-3}$	$-2.83 \times 10^{-3}$	$1.50 \times 10^{-3}$	$5.59 \times 10^{-4}$	$9.08 \times 10^{-4}$	$-7.00 \times 10^{-5}$	$-1.55 \times 10^{-5}$	$4.52 \times 10^{-4}$
1.10-1.20	$1.09 \times 10^{-3}$	<b>1.00</b>	$2.72 \times 10^{-2}$	$-1.33 \times 10^{-3}$	$5.46 \times 10^{-3}$	$2.55 \times 10^{-3}$	$2.06 \times 10^{-3}$	$1.09 \times 10^{-3}$	$1.18 \times 10^{-3}$	$1.95 \times 10^{-3}$
1.20-1.30	$-2.83 \times 10^{-3}$	$-1.33 \times 10^{-3}$	<b>1.00</b>	$1.42 \times 10^{-2}$	$-3.34 \times 10^{-4}$	$-2.35 \times 10^{-3}$	$-2.30 \times 10^{-4}$	$-2.74 \times 10^{-4}$	$-1.57 \times 10^{-4}$	$-9.35 \times 10^{-5}$
1.30-1.40	$1.50 \times 10^{-3}$	$5.46 \times 10^{-3}$	$-3.34 \times 10^{-4}$	<b>1.00</b>	$1.83 \times 10^{-2}$	$2.02 \times 10^{-3}$	$-1.74 \times 10^{-4}$	$1.85 \times 10^{-3}$	$1.04 \times 10^{-3}$	$1.91 \times 10^{-3}$
1.40-1.50	$5.59 \times 10^{-4}$	$2.55 \times 10^{-3}$	$-2.35 \times 10^{-3}$	$2.02 \times 10^{-3}$	<b>1.00</b>	$1.13 \times 10^{-2}$	$-4.52 \times 10^{-4}$	$4.55 \times 10^{-4}$	$3.33 \times 10^{-4}$	$6.49 \times 10^{-4}$
1.50-1.70	$9.08 \times 10^{-4}$	$2.06 \times 10^{-3}$	$-2.30 \times 10^{-4}$	$-1.74 \times 10^{-4}$	$-4.52 \times 10^{-4}$	<b>1.00</b>	$5.03 \times 10^{-3}$	$-4.94 \times 10^{-4}$	$1.18 \times 10^{-4}$	$4.37 \times 10^{-4}$
1.70-1.90	$-7.00 \times 10^{-5}$	$1.09 \times 10^{-3}$	$-2.74 \times 10^{-4}$	$1.85 \times 10^{-3}$	$4.55 \times 10^{-4}$	$-4.94 \times 10^{-4}$	<b>1.00</b>	$3.36 \times 10^{-3}$	$8.60 \times 10^{-5}$	$4.29 \times 10^{-4}$
1.90-2.10	$-1.55 \times 10^{-5}$	$1.18 \times 10^{-3}$	$-1.57 \times 10^{-4}$	$1.04 \times 10^{-3}$	$3.33 \times 10^{-4}$	$1.18 \times 10^{-4}$	$8.60 \times 10^{-5}$	<b>1.00</b>	$2.11 \times 10^{-4}$	$2.74 \times 10^{-5}$
2.10-2.30	$4.52 \times 10^{-4}$	$1.95 \times 10^{-3}$	$-9.35 \times 10^{-5}$	$1.91 \times 10^{-3}$	$6.49 \times 10^{-4}$	$4.37 \times 10^{-4}$	$4.29 \times 10^{-4}$	$2.11 \times 10^{-4}$	<b>1.00</b>	$3.66 \times 10^{-5}$
2.30-3.00	$-1.40 \times 10^{-4}$	$3.76 \times 10^{-5}$	$-6.73 \times 10^{-5}$	$2.00 \times 10^{-4}$	$8.44 \times 10^{-5}$	$1.04 \times 10^{-5}$	$1.01 \times 10^{-4}$	$2.74 \times 10^{-5}$	$3.66 \times 10^{-5}$	<b>1.00</b>

Table 11.26: Covariance matrix for the normalized particle-level fiducial phase-space differential cross-section as a function of invariant mass of the  $t\bar{t}$  system , accounting for the statistical and systematic uncertainties.

bin [GeV]	1.00-1.10	1.10-1.20	1.20-1.30	1.30-1.40	1.40-1.50	1.50-1.70	1.70-1.90	1.90-2.10	2.10-2.30	2.30-3.00
1.00-1.10	<b>1.00</b>	0.05	-0.17	0.08	0.04	0.09	-0.01	-0.00	0.08	-0.10
1.10-1.20	0.05	<b>1.00</b>	-0.07	0.24	0.15	0.18	0.11	0.17	0.29	0.02
1.20-1.30	-0.17	-0.07	<b>1.00</b>	-0.02	-0.19	-0.03	-0.04	-0.03	-0.02	-0.06
1.30-1.40	0.08	0.24	-0.02	<b>1.00</b>	0.14	-0.02	0.24	0.19	0.35	0.15
1.40-1.50	0.04	0.15	-0.19	0.14	<b>1.00</b>	-0.06	0.07	0.08	0.15	0.08
1.50-1.70	0.09	0.18	-0.03	-0.02	-0.06	<b>1.00</b>	-0.12	0.04	0.15	0.01
1.70-1.90	-0.01	0.11	-0.04	0.24	0.07	-0.12	<b>1.00</b>	0.04	0.18	0.17
1.90-2.10	-0.00	0.17	-0.03	0.19	0.08	0.04	0.04	<b>1.00</b>	0.13	0.07
2.10-2.30	0.08	0.29	-0.02	0.35	0.15	0.15	0.18	0.13	<b>1.00</b>	0.09
2.30-3.00	-0.10	0.02	-0.06	0.15	0.08	0.01	0.17	0.07	0.09	<b>1.00</b>

Table 11.27: Correlation matrix for the normalized particle-level fiducial phase-space differential cross-section as a function of invariant mass of the  $t\bar{t}$  system , accounting for the statistical and systematic uncertainties.

bin [GeV]	0.00-0.30	0.30-0.60	0.60-0.90	0.90-1.20	1.20-1.50	1.50-2.00
0.00-0.30	<b>1.00</b>	$2.45 \times 10^{-3}$	$-6.06 \times 10^{-4}$	$5.68 \times 10^{-4}$	$3.11 \times 10^{-4}$	$-1.12 \times 10^{-4}$
0.30-0.60	$2.45 \times 10^{-3}$	<b>1.00</b>	$2.48 \times 10^{-3}$	$-1.73 \times 10^{-4}$	$3.07 \times 10^{-4}$	$-2.94 \times 10^{-5}$
0.60-0.90	$-6.06 \times 10^{-4}$	$2.48 \times 10^{-3}$	<b>1.00</b>	$3.07 \times 10^{-3}$	$7.29 \times 10^{-4}$	$4.71 \times 10^{-5}$
0.90-1.20	$5.68 \times 10^{-4}$	$-1.73 \times 10^{-4}$	$3.07 \times 10^{-3}$	<b>1.00</b>	$1.96 \times 10^{-3}$	$9.34 \times 10^{-6}$
1.20-1.50	$3.11 \times 10^{-4}$	$3.07 \times 10^{-4}$	$7.29 \times 10^{-4}$	$1.96 \times 10^{-3}$	<b>1.00</b>	$4.97 \times 10^{-4}$
1.50-2.00	$-1.12 \times 10^{-4}$	$-2.94 \times 10^{-5}$	$4.71 \times 10^{-5}$	$9.34 \times 10^{-6}$	$4.97 \times 10^{-4}$	<b>1.00</b>

Table 11.28: Covariance matrix for the normalized particle-level fiducial phase-space differential cross-section as a function of absolute value of the rapidity of the  $t\bar{t}$  system , accounting for the statistical and systematic uncertainties.

bin [GeV]	0.00-0.30	0.30-0.60	0.60-0.90	0.90-1.20	1.20-1.50	1.50-2.00
0.00-0.30	<b>1.00</b>	-0.25	0.21	0.14	-0.10	0.23
0.30-0.60	-0.25	<b>1.00</b>	-0.06	0.14	-0.03	0.09
0.60-0.90	0.21	-0.06	<b>1.00</b>	0.30	0.04	0.37
0.90-1.20	0.14	0.14	0.30	<b>1.00</b>	0.01	0.31
1.20-1.50	-0.10	-0.03	0.04	0.01	<b>1.00</b>	0.01
1.50-2.00	0.23	0.09	0.37	0.31	0.01	<b>1.00</b>

Table 11.29: Correlation matrix for the normalized particle-level fiducial phase-space differential cross-section as a function of absolute value of the rapidity of the  $t\bar{t}$  system , accounting for the statistical and systematic uncertainties.

bin [GeV]	0.00-2.50	2.50-2.75	2.75-3.00	3.00-3.14
0.00-2.50	$6.21 \times 10^{-6}$	$2.85 \times 10^{-5}$	$1.28 \times 10^{-5}$	$-6.83 \times 10^{-5}$
2.50-2.75	$2.85 \times 10^{-5}$	$3.22 \times 10^{-3}$	$1.40 \times 10^{-3}$	$-1.76 \times 10^{-4}$
2.75-3.00	$1.28 \times 10^{-5}$	$1.40 \times 10^{-3}$	$4.12 \times 10^{-3}$	$-3.77 \times 10^{-3}$
3.00-3.14	$-6.83 \times 10^{-5}$	$-1.76 \times 10^{-4}$	$-3.77 \times 10^{-3}$	$1.61 \times 10^{-2}$

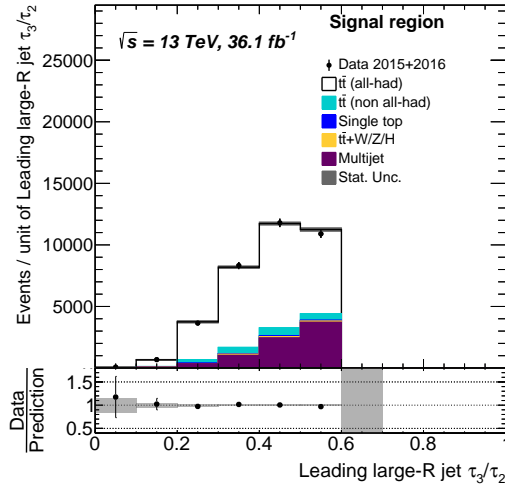
Table 11.30: Covariance matrix for the normalized particle-level fiducial phase-space differential cross-section as a function of azimuthal angle between the two top-quark jets  $\Delta\phi_{t\bar{t}}$  , accounting for the statistical and systematic uncertainties.

bin [GeV]	0.00-2.50	2.50-2.75	2.75-3.00	3.00-3.14
0.00-2.50	<b>1.00</b>	0.20	0.08	-0.22
2.50-2.75	0.20	<b>1.00</b>	0.38	-0.02
2.75-3.00	0.08	0.38	<b>1.00</b>	-0.46
3.00-3.14	-0.22	-0.02	-0.46	<b>1.00</b>

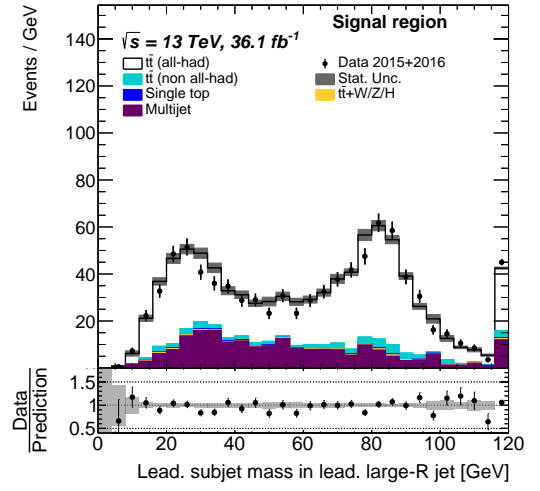
Table 11.31: Correlation matrix for the normalized particle-level fiducial phase-space differential cross-section as a function of azimuthal angle between the two top-quark jets  $\Delta\phi_{t\bar{t}}$  , accounting for the statistical and systematic uncertainties.

## **11.3 POWHEG+HERWIG7 vs POWHEG+PYTHIA8 @ detector level distribution**

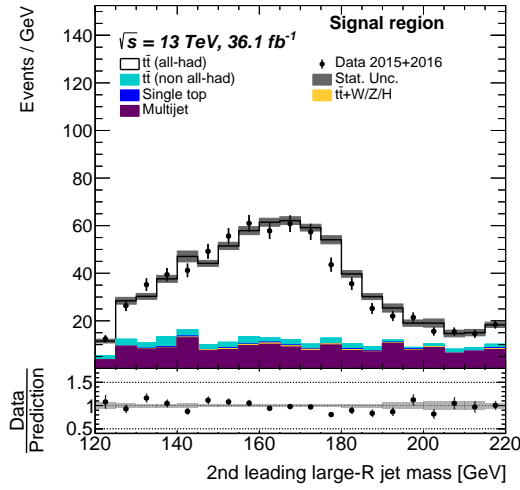
### **11.3.1 POWHEG+HERWIG7 distribution**



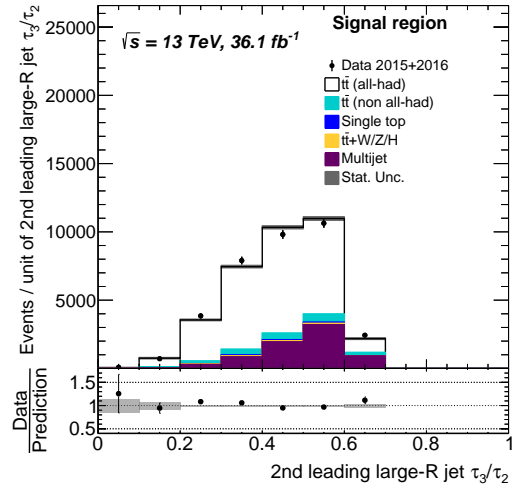
(a)



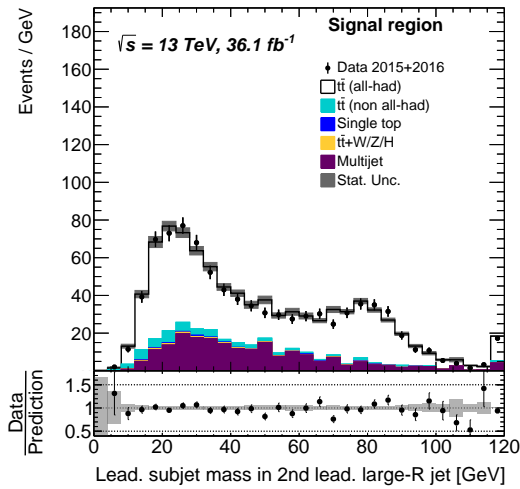
(b)



(c)

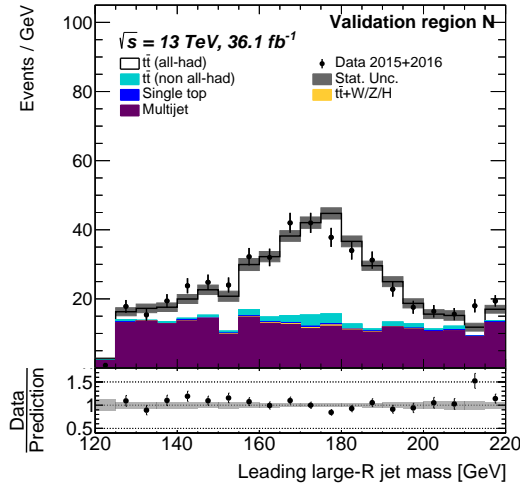


(d)

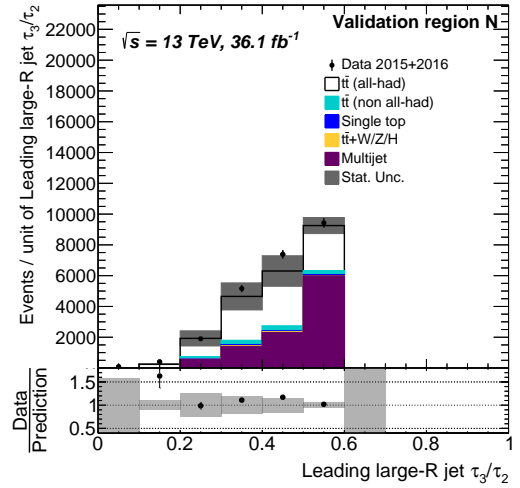


(e)

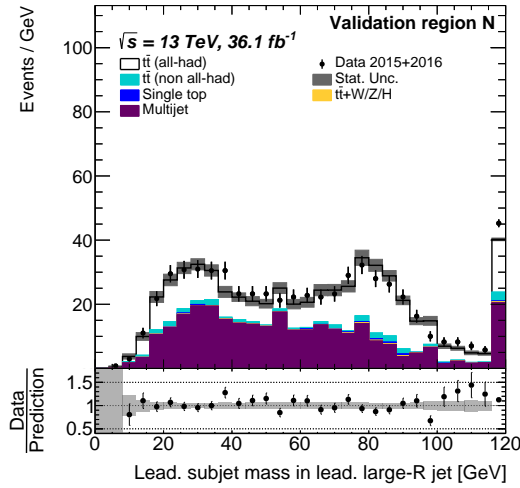
Figure 11.1: Kinematic distributions of large- $R$  jets in the signal: mass, 3/2-subjettiness ratio and leading subjet mass of the Leading and 2nd Leading Large- $R$  jet.



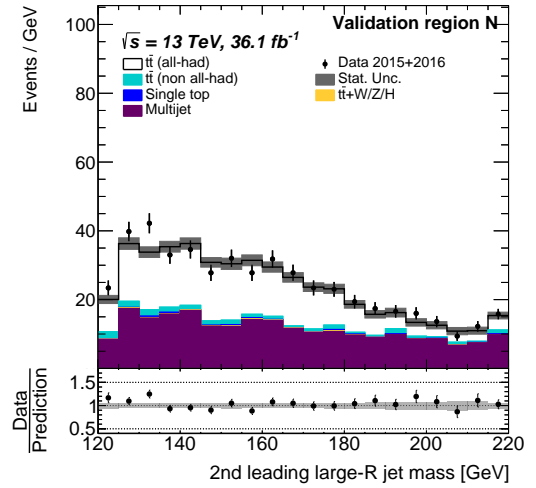
(a)



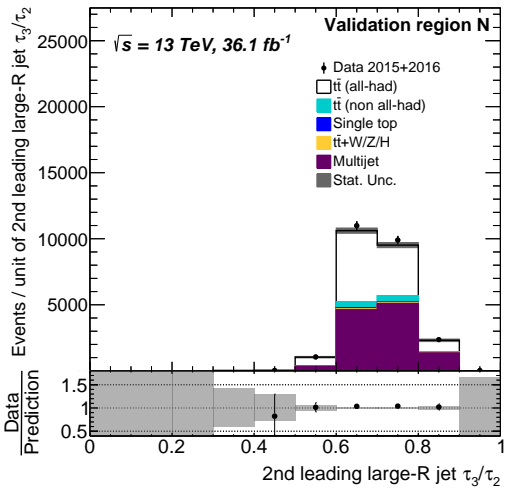
(b)



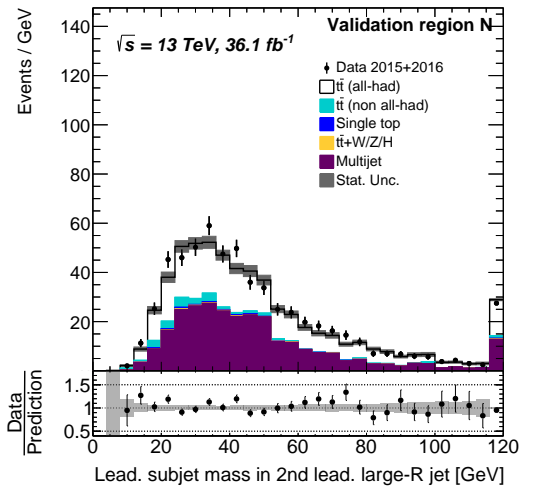
(c)



(d)

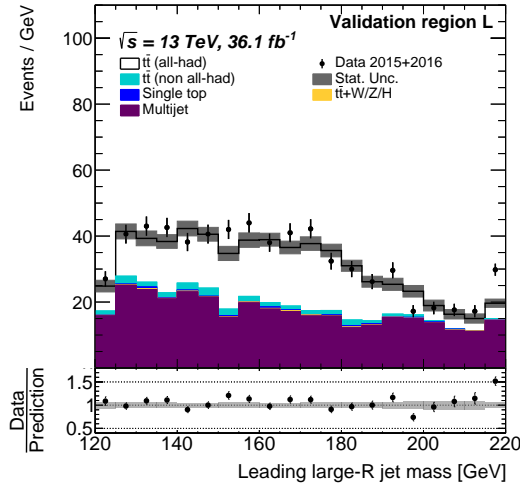


(e)

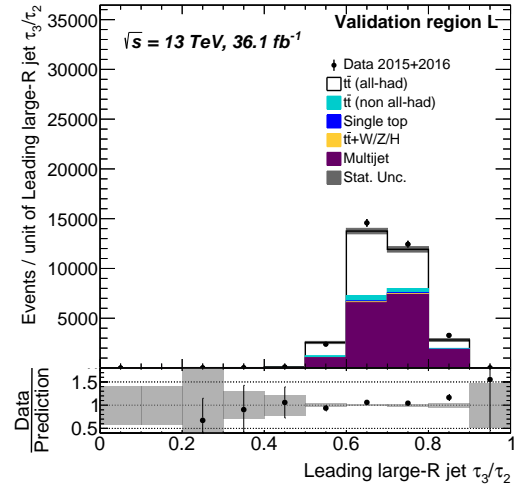


(f)

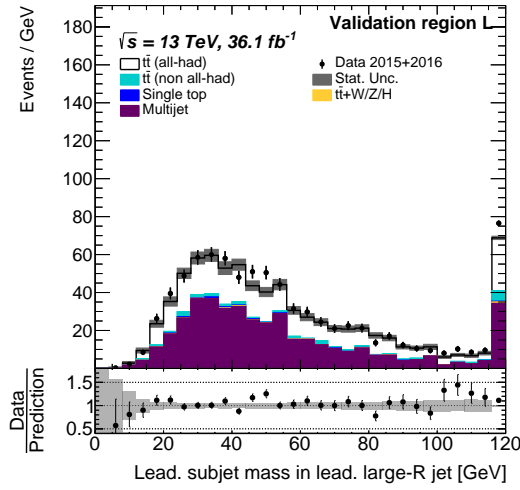
Figure 11.2: Kinematic distributions of large- $R$  jets in the control regions N: mass, 3/2-subjettiness ratio and leading subjet mass of the Leading and 2nd Leading Large- $R$  jet.



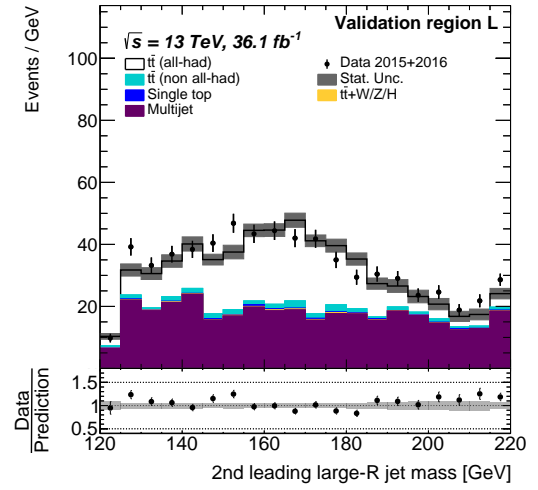
(a)



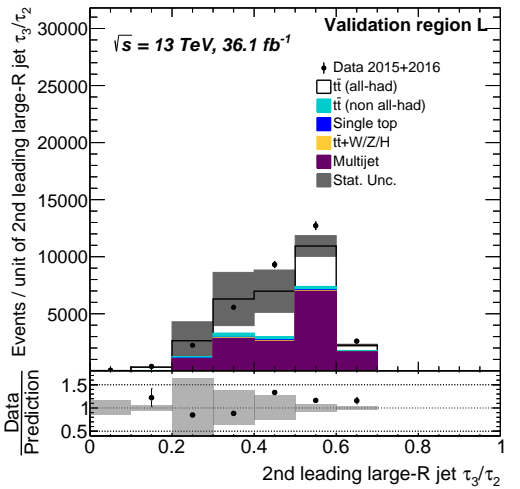
(b)



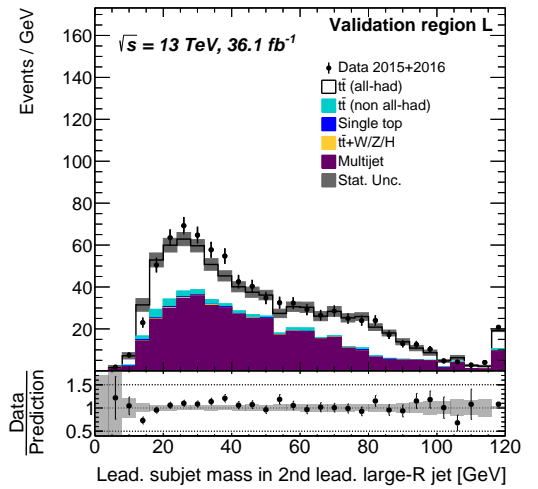
(c)



(d)



(e)



(f)

Figure 11.3: Kinematic distributions of large- $R$  jets in the control regions L: mass,  $N$ -subjettiness ratio and leading subjet mass of the Leading and 2nd Leading Large- $R$  jet.

### 11.3.2 POWHEG+PYTHIA8 distribution

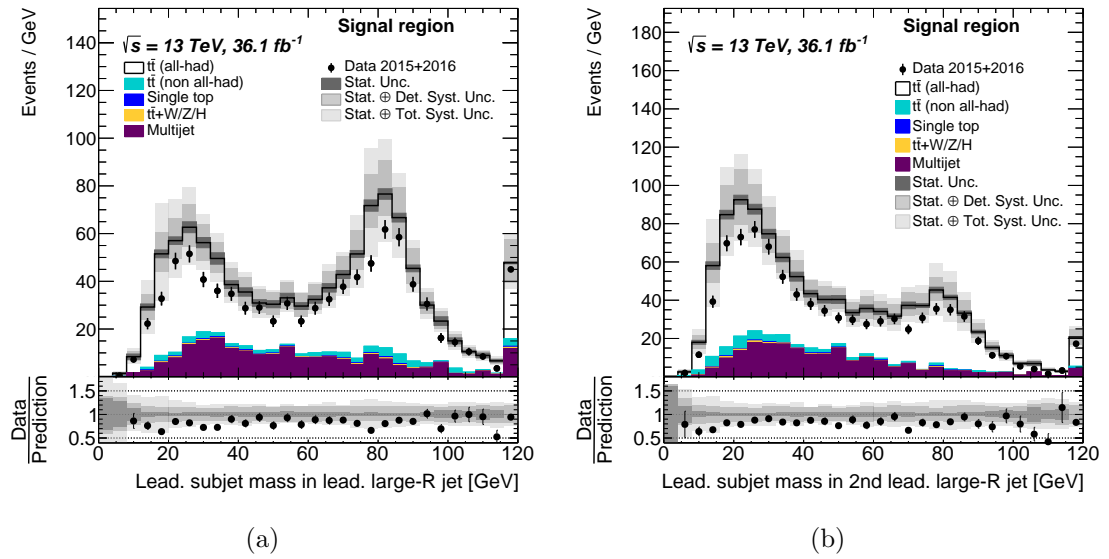
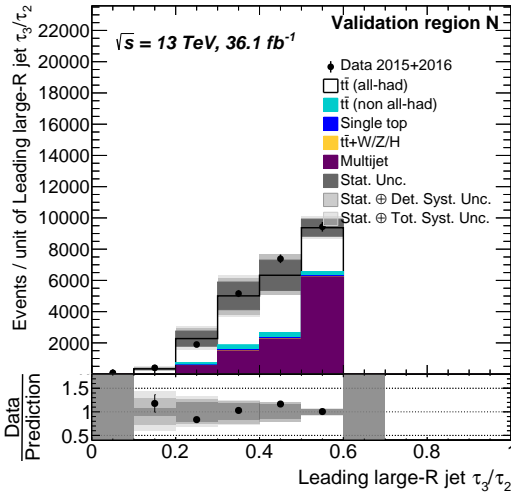
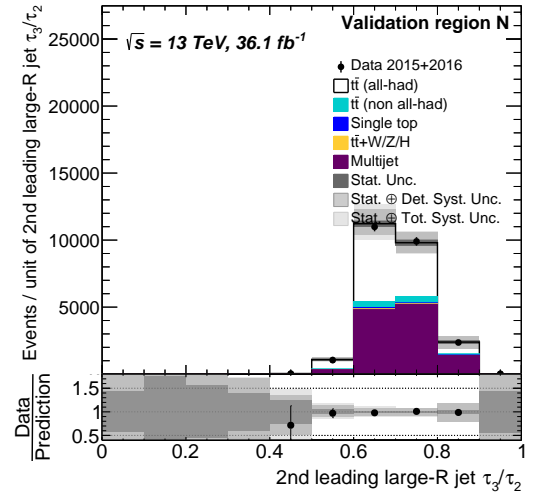


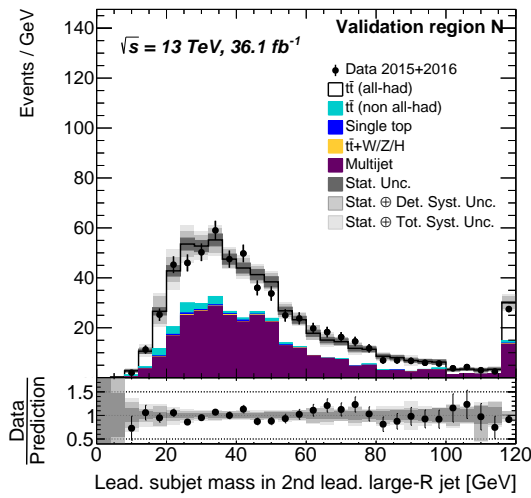
Figure 11.4: Kinematic distributions of large- $R$  jets in the signal: leading subject mass of the Leading and 2nd Leading Large- $R$  jet.



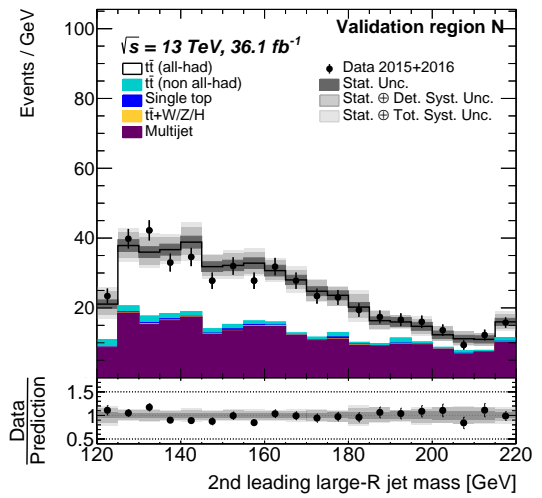
(a)



(b)

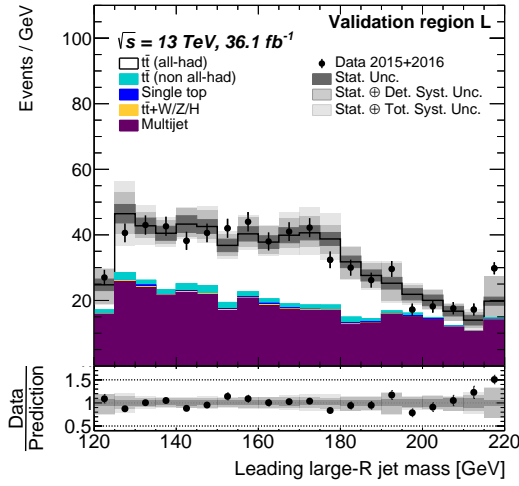


(c)

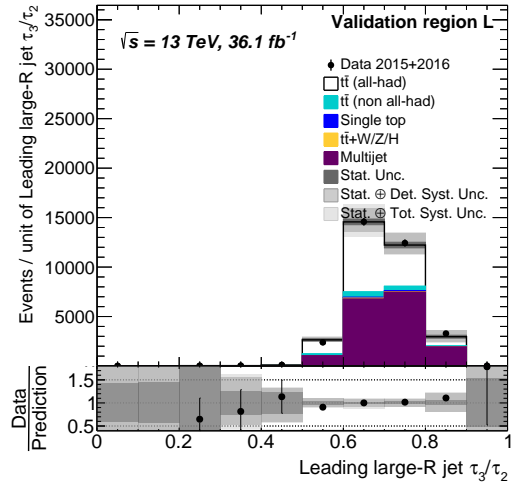


(d)

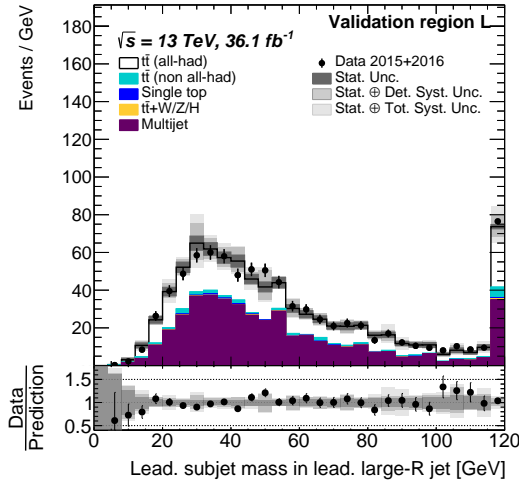
Figure 11.5: Kinematic distributions of large- $R$  jets in the control regions N : 3/2-subjettiness ratio and leading subject mass of the Leading and 2nd Leading Large- $R$  jet.



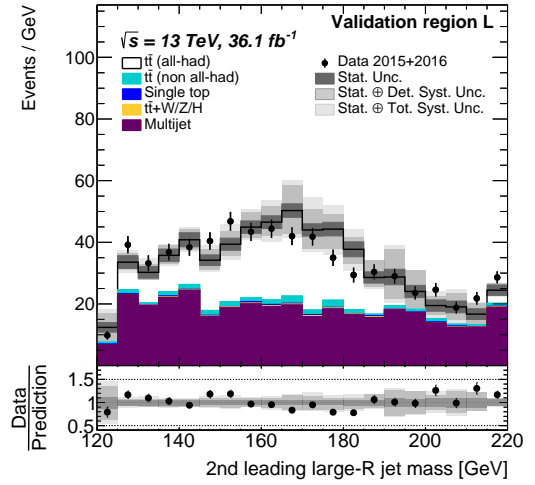
(a)



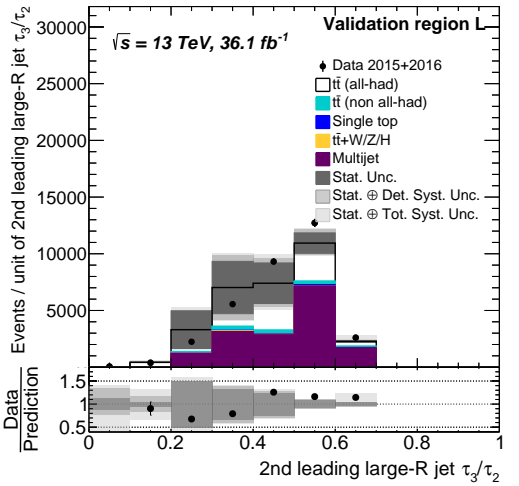
(b)



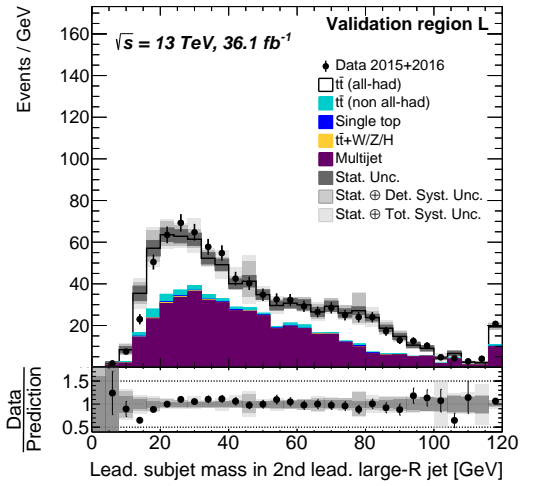
(c)



(d)



(e)



(f)

Figure 11.6: Kinematic distributions of large- $R$  jets in the control regions L: mass, 3/2-subjettiness ratio and leading subject mass of the Leading and 2nd Leading Large- $R$  jet.